Université d'Ottawa · University of Ottawa

Performance Analysis and Robustness of the ATM Adaptation Layer 2 over Wireless ATM Networks

By

Luis Armando Villaseñor González

A thesis submitted to the
Faculty of Graduate and Postdoctoral Studies
in partial fulfillment of the requirements
for the degree of

Doctor of Philosophy

University of Ottawa

Ottawa-Carleton Institute for Electrical and Computer Engineering
School of Information Technology and Engineering

August 12, 2002

0-612-76469-9

Table of Contents

List of Figures

List of Tables

List of Abbreviations

AAL	ATM Adaptation Layer
ADPCM	Adaptive Differential Pulse Code Modulation
ATM	Asynchronous Transfer Mode
AWGN	Additive White Gaussian Noise
BCH	Bose-Chaudhuri-Hocquenghem
BER	Bit Error Rate
BFSK	Binary Frequency Shift Keying
BPSK	Binary Phase Shift Keying
BSC	Binary Symmetric Channel
CI	Confidence Interval
CID	Channel Identifier
CPS	Common Part Sublayer
CPS-PH	Common Part Sublayer Packet Header
CPS-PP	Common Part Sublayer Packet Payload
CS-ACELP	Conjugate-Structure Algebraic Code Excited Linear Prediction
DF	Delineation Field
DMC	Discrete Memoryless Channel
DS	Delineation Sequence
DSLI	Delineation Sequence Length Indicator
EDU	Encoding Data Unit
EGC	Equal Gain Combining
FEC	Forward Error Correction
FSMC	Finite State Markov Chain
HEC	Header Error Control
HMM	Hidden Markov Model
IMT-2000	International Mobile Telecommunications for the year 2000
ITU	International Telecommunications Union
LAS	Local Area Subsystem
LI	Length Indicator
LOS	Line-of-Sight

mCLR	mini-Cell Loss Rate
mPBER	mini-cell Payload Bit Error Rate
mPER	mini-cell Payload Error Rate
MRC	Maximal Ratio Combining
MS	Mobile Subsystem
OSF	Offset Field
PCM	Pulse Code Modulation
PDU	Protocol Data Unit
QoS	Quality of Service
QPSK	Quadrature Phase Shift Keying
RS	Reed-Solomon
SD	Selection Diversity
SDU	Service Data Unit
SID	Silence Insertion Descriptor
SMCS	System Management and Control Subsystem
SN	Sequence Number
SNR	Signal-to-Noise Ratio
STF	Start Field
SSCS	Service Specific Convergence Sublayer
UMTS	Universal Mobile Telecommunication Systems
UUI	User-to-User Indication
WAS	Wide Area Subsystem
WATM	Wireless ATM

Glossary

$\oplus$ – Modulo-2 addition

α – Amplitude of the fading signal

β_m – A random variable. Denotes the successful or unsuccessful delivery of the m-th AAL2 packet to the higher layers

ε – Channel bit error rate

$\phi_{ij}(k, n)$ – The probability that exactly k bits are in error in $0, 1, \ldots, n-1$ time-units and the channel state at time instant n is j given that the channel state at time instant 0 was i

γ – The received Signal-to-Noise ratio

$\mathbf{\Phi}(k,n)$ – The matrix with elements $\phi_{ij}(k, n)$

$\Gamma(\cdot)$ – Gamma function

$\Gamma(\cdot,\cdot,\cdot)$ – Generalized incomplete gamma function

Ω – Mean-square value of the fading amplitude

$\boldsymbol{\pi}$ – Stationary state vector of a Markov chain

ρ – Correlation coefficient

τ – The mean burst length

τ_b – The channel symbol duration

$\mathbf{A}$ – A general matrix

$\mathbf{A}^T$ – Transpose of matrix $\mathbf{A}$

C_n – Random variable associated to the state of a Markov chain at time-instant n

$\mathbf{D_e}$ – A diagonal matrix with the state error probabilities of a FSMC model

d_{min} – Minimum distance of a block code

$d(\mathbf{v},\mathbf{w})$ – Hamming distance of two codewords $\mathbf{v}$ and $\mathbf{w}$

$e(\gamma)$ – The probability of bit error, as a function of the Signal-to-Noise ratio, in an Additive White Gaussian Noise (AWGN) channel

$erfc(.)$ – The complementary error function

$\mathbf{e}$ – The unit column vector

$\mathrm{E}[\cdot]$ – Expected value of a Random Variable

E_n – Random variable associated to the bit error process of the error-prone link

f_c – The carrier frequency

f_d – Doppler frequency

$f_X(x)$ – Probability density function of a random variable X

$f_{X,Y}(x,y)$ – Joint probability density function of two random variables X, Y

H_A – The header of an ATM cell

H_m – The header of the m-th AAL2 packet

H_S – The STF field

$\mathbf{I}$ – Identity matrix

$I_0(\cdot)$ – Zero-order modified Bessel Function of the first kind

$I_m(\cdot)$ – m-order modified Bessel Function of the first kind

k_m – A random variable. Denotes the number of bit errors in the m-th AAL2 packet payload

$J_0(\cdot)$ – Zero-order Bessel function of the first kind

L_m – The length (in bits) of the m-th AAL2 packet payload

M' – The number of bits from a CPS packet that has exceeded the boundaries of the previous CPS-PDU.

N – Number of states of a finite state Markov chain

N_A – The length (in bits) of the ATM cell header

N_S – The length (in bits) of the Start Field

N_m – the length (in bits) of the m-th AAL2 packet header

$\mathbf{P}$ – Transition probability matrix

$\mathbf{P}^M$ – M-step transition probability matrix

$\mathbf{P_e}$ – State error probability vector

p_{ij} – Probability of a transition from state i into state j

$P_e(k)$ – Probability of bit errors in state k

P_m – The payload of the m-th AAL2 packet

$Pr[A]$ – Probability of event A

$Pr[A\,|\,B]$ – Probability of event A given event B

$Q(x)$ – The Q-function

R_c – The code rate of a block code

s_k – State k of a Markov chain

s^2 – The average scattered wave power normalized by the direct-wave power

S – The set of states of a Markov chain

U_n – The number of errors in a sequence of n bits

Abstract

The wireless and personal communication systems are experiencing an enormous growth due to recent advancements in wireless networking technologies. At the same time the cellular network infrastructure around the world is being upgraded to support the 3rd generation wireless communication networks, as defined by the International Mobile Telecommunications for the year 2000 (IMT-2000) and the Universal Mobile Telecommunication Systems (UMTS) standards. As a result there is great interest in evaluating diverse technologies that can be used to handle the heterogeneous traffic types and at the same time be able to provide quality of service guarantees and ATM has been identified as an ideal transport technology for this type of networks.

The research presented in this thesis details the use of the ATM Adaptation Layer 2 (AAL2) standard, which is used to adapt low data rate and delay sensitive traffic in ATM networks. In this work we are interested in evaluating the performance of the AAL2 standard over error-prone wireless links. Therefore we are interested in proposing a mechanism to improve the performance that is observed at the AAL2 layer.

The study begins by evaluating diverse analytical models to characterize the bit error process at the physical layer over error-prone links. This study has identified that the Finite State Markov Chain (FSMC) models provide a suitable analytical work frame to evaluate the impact of bit errors at the higher protocol layers, such as the AAL2. Based on the FSMC models we derive analytical expressions to evaluate the impact of bit errors at the AAL2 layer and numerical results are obtained to evaluate the performance of the AAL2 standard over the error-prone links. Later the analytical expressions are used to evaluate the performance improvements at the AAL2 layer when implementing diverse techniques that are commonly used to improve system performance. Such techniques include the use of Forward Error Correction codes and diversity techniques. Finally, a robust frame format is proposed for the AAL2 standard. The proposed frame format improves the performance of the AAL2 standard by introducing a robust mechanism for the delineation of AAL2 packets. In addition, the proposed mechanism can reduce the overhead introduce by the header fields that are required to achieve the delineation of the AAL2 packets inside the payload of the ATM cells.

Acknowledgments

Throughout my doctoral studies there have been several people and even organizations that have contributed and assisted me in achieving this important milestone of my professional career. I want to start by acknowledging the people that were academically involved in diverse aspects of my studies and research. I want to thank my thesis supervisor, Dr. Luis Orozco-Barbosa, for assisting me throughout my doctoral studies. His dedication and support have been of great help in the successful accomplishment of my research. I also want to thank Louise Lamont for giving me the opportunity to complete my research at the Communications Research Centre Canada (CRC). In addition, I want to acknowledge the support from Dr. Sophia Tsakiridou. Both Mrs. Lamont and Dr. Tsakiridou provided me with useful comments and suggestions during my research at CRC.

Next I want to acknowledge the support I have received from multiple organizations. Many thanks to the people at the Communications Research Centre Canada (CRC) for the support I received during my doctoral studies; in particular many thanks to Dr. John Robinson, Research Manager of the Network Systems group. In addition, I want to acknowledge the support from the Defence Research and Development Canada agency. I also want to acknowledge the support I received from the Centro de Investigación Científica y Educación Superior de Ensenada (CICESE); in particular many thanks to M.C. Jorge Preciado. As well, I want to acknowledge the support I received from the Consejo Nacional de Ciencia y Tecnología (CONACYT).

And finally I want to thank my family and friends. Many thanks to my wife Edith and my wonderful three children Topacio, Huong and Luis Alberto for the support they provided me, as well as, for all the sacrifices they endured during my studies. I also want to express my immense gratitude to my parents Amado and Maricela; this achievement is greatly possible because of the support I have received from them. Also, I want to thank my brother Carlos Alberto for his love and support. From the University of Ottawa, I want to thank my fellow Ph.D. student Miguel López Guerrero for his unconditional friendship, both to me and my family.

Chapter 1 Introduction

The Asynchronous Transfer Mode (ATM) technology was initially introduced during the early 1990s and today it is widely used over public and private telecommunication systems all over the world. One of the main reasons for the great success of ATM is because of its ability to support a whole range of applications with Quality of Service (QoS) guarantees. Figure 1.1 illustrates the protocol stack of the ATM standard as defined by the International Telecommunications Union (ITU).

Throughout these years there has been a great deal of investment in terms of research, equipment development and deployment based on the ATM standard, and in more recent years there has been great interest in the use of the ATM technology for the 3rd generation wireless communication networks [1], [2], as defined in the International Mobile Telecommunications for the year 2000 (IMT-2000) and the Universal Mobile Telecommunication Systems (UMTS) standards. Currently the cellular network infrastructure around the world is being upgraded to support the emerging 3rd generation wireless communication networks and the ATM technology is being integrated into this type of networks to manage the heterogeneous traffic types and at the same time to support the diverse quality of service requirements in the network.

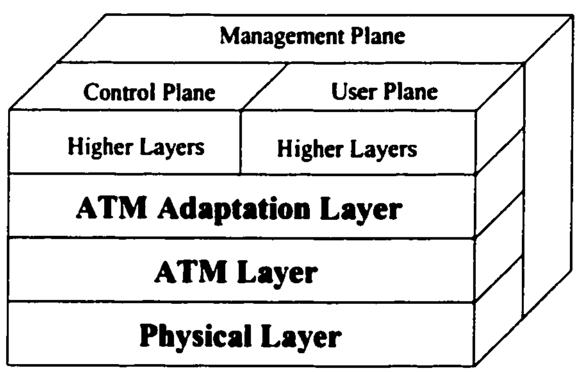

Figure 1.1: The ATM protocol stack.

Similarly there is great interest in the use of commercial technologies, such as the ATM standard, which can be integrated as part of the military tactical telecommunication networks [3]-[11]. Several authors have proposed the use of ATM over strategic and tactical military networks arguing that implementing a well-known and tested technology would greatly reduce costs. Additionally the use of ATM can increase the interoperability between strategic and tactical nodes, as well as, the interconnectivity with civilian telecommunication networks. One implementation example of the use of ATM over military tactical networks is the POST-2000 Tactical Communications Systems for NATO [10].

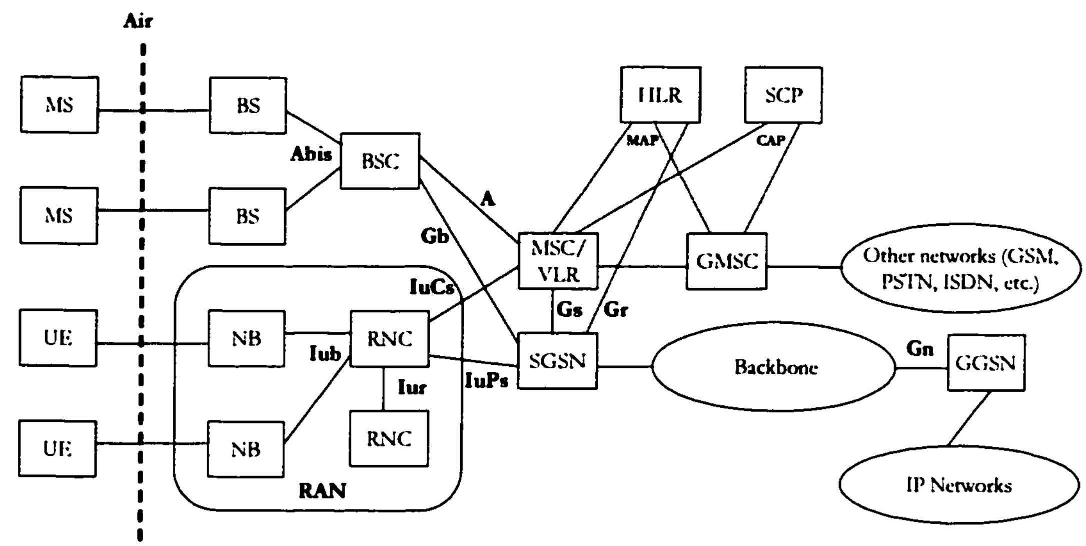

MS/UE = 2G/3G Mobile Station
BS/NB = 2G/3G Base Station
BSC = Base Station Controller
RNC = Radio Network Controller
RAN = Radio Access Network

MSC = Mobile Switching Centre
VLR = Visitor Location Register
SGSN = Serving GPRS Support Node
GMSC = Gateway MSC
GGSN = Gateway GPRS Support Node

SCP = Service Control Point
HLR = Home Location Register
CAP = CAMEL Application Part
MAP = Mobile Application Protocol

Figure 1.2: UMTS/GSM network architecture.

The research presented in this thesis details the use of the ATM Adaptation Layer 2 (AAL2) standard [12], which is used to adapt low data rate and delay sensitive traffic in ATM networks. One of the main characteristics of the AAL2 standard is that it can multiplex the information from multiple sources and therefore be able to make an efficient use of the bandwidth utilization. Because of the particular characteristics of the ATM Adaptation Layer 2, the AAL2 standard has been proposed to be used in the 3rd generation wireless communication networks [13]-[17]. Figure 1.2 illustrates an example of the UMTS/GSM network architecture, as depicted in reference [2]. It has been proposed that ATM and in particular AAL2, be used in the Radio Access Network (RAN) [2].

Similarly tactical military networks can benefit of the bandwidth improvements provided by the AAL2 standard, especially when dealing with bandwidth limited wireless links. Later in Chapter 2 we present a detailed description of the AAL2 standard, as well as, an example of a network architecture that has been proposed for tactical military networks.

In this work we are interested in evaluating the performance of the AAL2 standard over error-prone wireless links. Therefore we are interested in proposing a mechanism to improve the performance that is observed at the AAL2 layer in ATM wireless networks.

1.1 Research Motivation

This research study is motivated by the interest of the Defence Research and Development Canada agency in the performance evaluation of the ATM and the AAL2 standards over error-prone links. The nature of military strategic and tactical networks will require the support for telecommunication between mobile nodes. Usually, these mobile nodes require the use of wireless telecommunications links, which are limited in bandwidth and present a much higher bit error rate (BER) than that of wired links. On the other hand, the ATM standard was conceived to be used over highly reliable links, such as fiber-optic links, with BER in the order of 10^{-10} or less. If the ATM standard is to be used over error-prone links, such as wireless links, then several technical issues must first be resolved for the successful deployment of the ATM technology over strategic and tactical networks.

Of special interest, in this work, is the support of low data rate and delay sensitive applications over wireless links. Identifying the need for a new ATM Adaptation Layer (AAL), which could efficiently support this type of applications, the ITU-T has standardized the AAL Type 2 (AAL2) under specification I.363.2 [12]. Nevertheless, as currently specified, the AAL2 standard does not provide an efficient protection mechanism to allow for its efficient deployment over wireless ATM networks. It is the purpose of this work to evaluate the performance of the AAL2 standard over error-prone links and propose diverse mechanisms to improve the system performance that is observed at the AAL2 layer.

1.2 Research Objectives and Methodology

The purpose of this work is to present a performance analysis of the ATM adaptation Layer 2 over wireless ATM links, and evaluate the resiliency of the AAL2 standard in error-prone networks. In addition we want to propose a robust system design to improve transmission performance, over such wireless channels, by reducing the probability of bit errors at the ATM Adaptation layer 2. The main objectives of this work include the:

- Performance evaluation of the AAL2 standard over error-prone links.
- Proposal and evaluation of mechanisms to improve system performance over wireless links.
- Proposal of a robust system design for the transmission of low data rate and delay sensitive services over wireless ATM links.

To achieve these objectives the following research methodology was implemented:

– *Wireless Channel Characterization*: The analytical characterization of a wireless link is required to evaluate the impact of wireless channel impairments, such as, interference, fading and noise over wireless data transmission. The presence of these channel impairments in the wireless link has a direct impact on the bit error process experienced by the receiver. Then the wireless channel model is useful in the analysis of performance metrics of interest, which can be used to evaluate the impact of the channel impairments at the higher protocol layers.

– *Performance Analysis of ATM/AAL2 over Wireless Links*: The standard ATM/AAL2 frame format is affected by the channel impairments over the Wireless link. Thus, the importance to understand how these channel impairments will affect the transport of the ATM/AAL2 frames over wireless links. The performance analysis of the ATM/AAL2 includes the derivation of performance metrics of interest, which are used to evaluate the impact of the bit error process at the ATM adaptation layer.

– *Proposal and Evaluation of Mechanisms to Improve System Performance*: One of the main characteristics of wireless channels is the presence of a higher bit error rate, as compared to that of wired links. Then, it is important to evaluate and propose diverse mechanisms to improve the transmission performance over error-prone links. Some of these mechanisms include the use of well known techniques, such as, forward error correction (FEC) codes and the possibility of implementing diversity techniques. Other mechanisms may include protocol enhancements to reduce the impact of wireless channel impairments at the higher protocol layers.

– *System Design and Performance Evaluation*: The end goal of this research is the proposal of a robust system design for the transmission of low data rate and delay sensitive services, such as voice, over wireless ATM links. The derivation of a robust system design is based on the analysis of performance results obtained from diverse mechanisms, which are used to improve system performance. In addition, a performance analysis is presented to validate the robustness of the proposed system for the transmission of low data rate and delay sensitive applications over wireless ATM networks.

1.3 Contributions and List of Publications

The research presented in this dissertation is related to the support of the ATM Adaptation Layer 2 over error-prone channels, such as wireless links. The main contributions of this work can be summarized as follows:

– The derivation of analytical expressions to evaluate performance metrics of interest at the AAL2 layer. These analytical expressions account for the impact of the bit error process at the physical layer, as well as, for the frame structure at the ATM an ATM Adaptation layers.

- The performance analysis of the AAL2 standard over an error-prone link.
- The derivation of performance results at the AAL2 layer by introducing diverse techniques to improve the system performance.
- The proposal of an improved mechanism to reduce the probability of losses at the AAL2 layer.

As part of the contributions from the research presented in this Thesis, several articles have been published in multiple journals, conferences and symposiums. In addition, there is a technical report submitted at the Communications Research Centre Canada. Following is a list of publications:

Journals

1 L. Villasenor-Gonzalez, S. Tsakiridou, L. Orozco-Barbosa, L. Lamont, "Performance Analysis of Wireless ATM/AAL2 over a Burst Error Channel", Computer Communications, Vol. 25, No. 1, Jan. 2002, pp. 1-8.

2 L. Villasenor-Gonzalez, L. Orozco-Barbosa, L. Lamont, "A Novel Delineation Mechanism for the ATM Adaptation Layer 2 over Wireless ATM Networks", International Journal of Communication Systems, (To appear)

Conference and Symposium Papers

1 L. Villasenor-Gonzalez, L. Orozco-Barbosa, L. Lamont, S. Tsakiridou, "Improved Delineation Mechanism for ATM Adaptation Layer 2 over Wireless ATM Networks", IEEE Military Communications Conference, McLean, USA, October 2001.

2 L. Villasenor-Gonzalez, L. Lamont, L. Orozco-Barbosa, "Resilient Mechanism for Low Data Rate and Delay Sensitive Traffic over Wireless ATM Networks", Information Systems Technology Panel Symposium on Military Communications", Warsaw, Poland, October 2001.

3 L. Villasenor-Gonzalez, L. Orozco-Barbosa, L. Lamont, "Performance Analysis of Wireless ATM/AAL2 over Correlated Fading Channels using Diversity", Proc. IASTED International Conference on Advances in Communications, Rhodes, Greece, July 2001, pp. 129-134

4 L. Villasenor-Gonzalez, S. Tsakiridou, L. Orozco-Barbosa, L. Lamont, "Performance Analysis of Wireless ATM/AAL2 over a Burst Error Channel", Proc. IEEE Canadian Conference on Electrical and Computer Engineering, Toronto, Canada, May 2001.

5 L. Villasenor-Gonzalez, S. Tsakiridou, L. Orozco-Barbosa, L. Lamont, "Performance Measures for Wireless ATM/AAL2 over a Gilbert-Elliott Channel", Proc. 20th Biennial Symposium on Communications, Kingston, Canada, May 2000, pp. 231-235.

Technical Reports

1 L. Villasenor-Gonzalez, L. Lamont, "Military Voice Services over Wireless ATM Networks: ATM Adaptation Layer Study", CRC Technical Report (CRC-RP-2001-02), March 2001.

1.4 Thesis Organization

The thesis is divided into 7 chapters. Chapter 1 presents the introduction and the motivation of this work, as well as, an overview of the methodology used to accomplish the proposed objectives of this research. Chapter 2 presents a description of the ATM Adaptation Layer 2 standard, which is used for the encapsulation of low data rate and delay sensitive traffic in ATM networks. In Chapter 3 we present the derivation of the Finite State Markov Channel models which are used in the characterization of the wireless channel. Chapter 4 presents the derivation of analytical expressions for performance metrics of interest at the AAL2 layer. In addition numerical results are presented to evaluate the performance of the AAL2 standard in the presence of bit errors. Then Chapter 5 shows the performance improvements achieved at the AAL2 layer when introducing diverse mechanisms to improve system performance. These mechanisms include the use of well known techniques, such as, the use of Forward Error Correction codes and the use of diversity techniques. In Chapter 6 a robust frame format is proposed for the AAL2 standard to improve system performance in the presence of error-prone links. Finally the conclusions of this work are presented in Chapter 7.

Chapter 2 Low Data Rate and Delay Sensitive Services in WATM Networks

2.1 Introduction

The Asynchronous Transfer Mode (ATM) technology is widely used over public and private telecommunication networks all over the world. One of the main reasons for the great success of ATM is due to its ability to support a whole range of applications, such as data, voice and video, with Quality of Service (QoS) guarantees. In addition, there has been a great deal of research around the ATM technology and many companies currently provide ATM solutions, thus allowing for an easy deployment of an ATM network.

In recent years, there has been great interest in the use of ATM technology for the 3rd generation wireless networks, as well as, over military telecommunication networks. Several authors have proposed the use of ATM over strategic and tactical military networks arguing that costs would be greatly reduced by implementing a well known technology [3]-[11]. Furthermore, the use of ATM will increase the interoperability and interconnectivity with civilian telecommunication networks, which is seen as an added benefit for implementing ATM over military networks. On the other hand, the nature of tactical networks requires the support for telecommunications between mobile nodes. Usually, these mobile nodes require the use of wireless communication links, which are limited in bandwidth and usually present higher bit error rates than that of wired links. Wireless link errors can affect significantly the performance at the ATM and the ATM Adaptation Layer, which inherently have very limited protection against errors. Consequently, it is important to evaluate the performance of ATM over the wireless medium, as the ATM technology was conceived to be used over highly reliable links with a BER in the order of 10^{-10}.

This work is concerned with the support of low data rate and delay sensitive traffic over point-to-point wireless ATM links. In this chapter we present a description of the ATM

Adaptation Layer 2, which was standardized by the ITU-T for the support of low data rate and delay sensitive traffic in ATM networks..

2.2 The ATM Adaptation Layer 2 (AAL2)

The use of the ATM Adaptation Layers AAL1, the AAL3/4 and the AAL5 for the transport of low data rate and delay sensitive services can result in partially filled ATM cells (i.e., they make an inefficient use of the bandwidth utilization). Identifying the need for a new ATM Adaptation Layer (AAL), the ITU-T has standardized the AAL type 2 (AAL2) under specification I.363.2 [12].

The ATM Adaptation Layer 2 (AAL2) was standardized in 1997 by the ITU-T for the support of low bit rate and delay sensitive traffic over ATM networks. The AAL2 standard can provide significant improvement in bandwidth utilization that is not attainable by using other previously defined ATM Adaptation Layers such as AAL1, AAL3/4 or AAL5. The structure of AAL2 layer, as defined by the ITU-T, is shown in Figure 2.1.

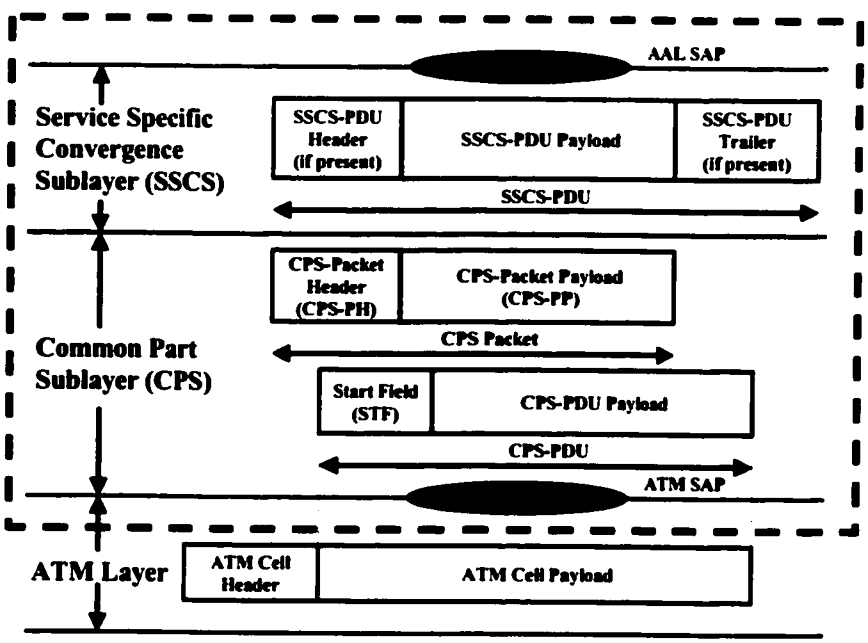

Figure 2.1: The AAL2 structure.

The AAL2 layer, as illustrated in Figure 2.1, is divided in two sublayers: the Common Part Sublayer (CPS) and the Service Specific Convergence Sublayer (SSCS). The AAL2 standard was designed to achieve efficient bandwidth utilization by multiplexing data from different sources within the payload of the AAL2 Common Part Sublayer Protocol Data Unit (CPS-PDU). The structure of the AAL2 CPS-PDU is depicted in Figure 2.2.

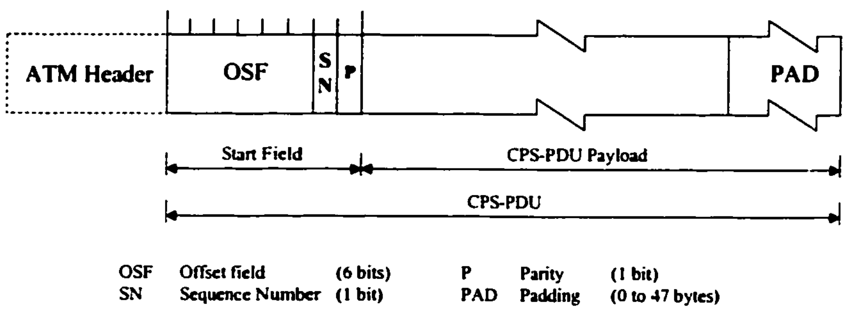

Figure 2.2: The structure of the AAL2 CPS-PDU.

The CPS-PDU consists of the Start Field (STF) of size one (1) byte and the CPS-PDU payload of size forty-seven (47) bytes. The CPS-PDU payload is formed from a sequence of CPS packets (AAL2 packets or mini-cells[1]) originating from different sources. The Start Field STF includes a six-bit Offset Field (OSF) used to identify the position of the first CPS packet within the CPS-PDU payload. It should be noted that a CPS packet could be mapped across CPS-PDU payload boundaries. The structure of the CPS packet, which consists of the CPS packet header (CPS-PH) and the CPS packet payload (CPS-PP), is shown in Figure 2.3.

The AAL2 CPS packet header is composed of four fields: the Channel Identifier (CID), the Length Indicator (LI), the User-to-User Indication (UUI) and the Header Error Control (HEC). The CID is an eight-bit field required for the identification of the user of the AAL2. The CID, as defined by the ITU-T, allows for up to 248 individual users to be multiplexed in a single AAL2 connection.

[1] The terms CPS packet, AAL2 packet and mini-cell are used interchangeably throughout this document.

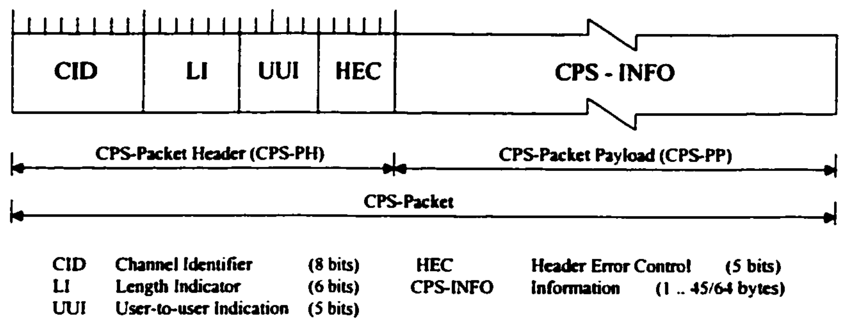

Figure 2.3: Structure of the AAL2 CPS packet.

Table 1 shows the description and the values (codes) for the CID field:

Table 1: The CID field codes.

Value	Use
0	Not Used
1	Reserved for Layer Management Peer-to-Peer Procedures
2-7	Reserved
8-255	AAL2 User (248 channels)

The LI is a six-bit field used to define the length of the CPS packet payload and to provide for the delineation of CPS packets in the CPS-PDU. The LI takes a value that is one less than the size of the CPS packet payload in bytes; the maximum CPS packet payload size is set to sixty-four (64) bytes.

The UUI is a five-bit field that serves two purposes:

- to convey specific information transparently between the CPS users, and,
- to distinguish between the SSCS entities and Layer Management users of the CPS.

The HEC is a five-bit field that provides for error detection in the CPS packet header. This field does not provide for any correction capability.

Some applications of the AAL2 standard include the encapsulation of voice-encoded information over ATM Networks. For example, the ITU-T recommendation I.366.2 specifies the packet formats, as well as, the procedures for the encapsulation of voice-encoded information at the Service Specific Convergence Sublayer (SSCS) of the AAL2 [18]. Recommendation I.366.2 introduces the concept of Encoding Data Unit (EDU), which is an octet-aligned concatenation of one or more frames of an audio algorithm. A group of N_1 EDUs is concatenated to form a Service Data Unit and M SDUs are concatenated to fill the payload of a CPS packet (CPS-PP), as shown in Figure 2.4. The selection of values for N_1 and M are specified as part of a predefined profile. Under recommendation I.366.2 a profile is defined as a set of entries, where each entry specifies an encoding format with a UUI range and length. In other words, a profile can specify different audio encoding formats, which are uniquely identified by the selection of values for the UUI and LI fields within each CPS packet.

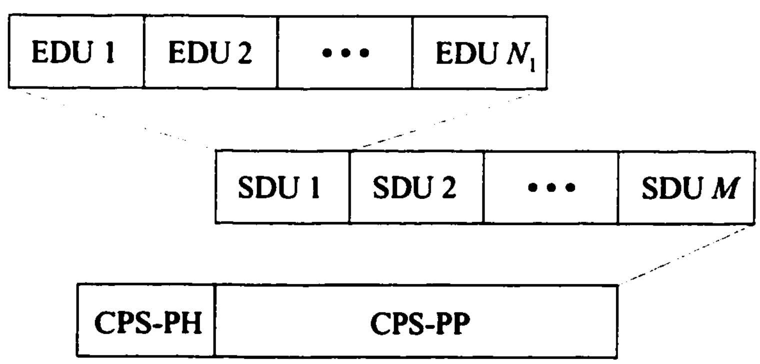

Figure 2.4: Encapsulation of voice-encoded data.

The ITU-T recommendation I.366.2 defines several profiles to be used with audio algorithms G.711 (PCM) [19], G.726 (ADPCM) [20] and G.729 (CS-ACELP) [21,22,23]. The audio algorithm G.729 is of particular interest, as it has been adopted as the default compressed algorithm for use with non-secure military voice [6, 7]. The Encoding Data Units, as well as, predefined profiles settings for these algorithms are presented in Appendix A.

In this section we have presented a description of the AAL2 standard as defined in the ITU-T recommendation I.363.2. In the next section we describe the network topology proposed in the POST-2000 Tactical Communication Systems for NATO. The NATO Post-2000 communications architecture illustrates a network topology in which ATM links are established over point-to-point wireless links. Usually these point-to-point wireless links are limited in bandwidth and the AAL2 standard can be used to improve the bandwidth utilization.

2.3 Tactical Network Topology

One implementation example of the use of ATM over military tactical networks is the POST-2000 Tactical Communications Systems for NATO [10]. The NATO Post-2000 communications architecture, as described in [10], is composed of four subsystems: the Local Area Subsystem (LAS), the Wide Area Subsystem (WAS), the Mobile Subsystem (MS) and the System Management and Control Subsystem (SMCS), shown in Figure 2.5.

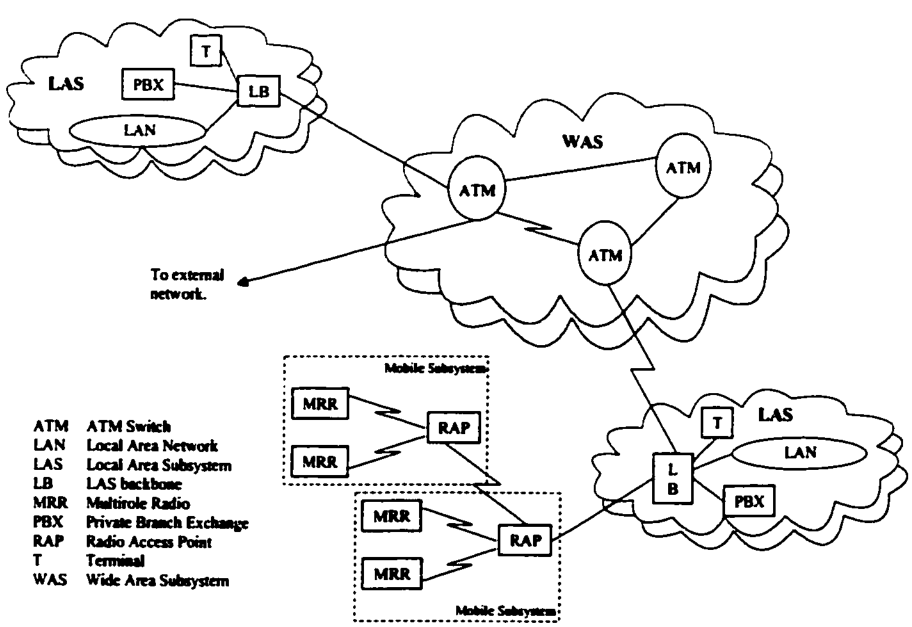

Figure 2.5: NATO Post-2000 communications architecture.

The Local Area Subsystem (LAS) is designed to support local and internal communications for a geographically restricted group of communication nodes (e.g., the LAS can be used to provide communications to the military headquarters). In addition the Local Area Subsystem can provide access to the Wide Area Subsystem, it can be the interface to the strategic networks and it can provide connection to commercial networks. The Wide Area Subsystem (WAS) allows for the interconnection of distant LAS users over a tactical transport system. The WAS can provide switching services at the network layer for LAS users crossing LAS boundaries. The Mobile Subsystem (MS) is designed for communications between mobile nodes. The MS can be operated as a stand-alone network or as part of the overall tactical network. The System Management and Control Subsystem (SMCS) provides for network management functions over the tactical network.

Due to the nature of tactical systems and the extended distances between WAS nodes, the POST-2000 for NATO architecture supports the use of radio links. The transmission characteristics of these radio links specify a throughput of 2 Mb/s as the maximum data rate for transmission between WAS nodes. Furthermore, it is recommended that for a maximum distance of 40 Km, radio frequencies between 1 GHz and 10 GHz should be used. The use of satellite links using frequencies between 1 GHz and 20 GHz is recommended for distances that are greater than 40 Km [10]. The distance between Wide Area Subsystems (WAS) and Local Area Subsystems (LAS) is expected to be less than 10 Km; in this case radio frequencies between 1 GHz and 10 GHz are expected to be appropriate. On the other hand, the radio link between RAP and WAS/LAS nodes is expected to be in the range of 1 Km and therefore the use of higher frequencies is recommended (e.g. EHF frequencies) [10].

From the NATO Post-2000 communication architecture, illustrated in Figure 2.5, we can identify several point-to-point links which can benefit from the bandwidth utilization improvement provided by the AAL2 standard. Recall, that the AAL2 standard improves bandwidth utilization by multiplexing information from multiple sources. Therefore the AAL2 standard can be used in point-to-point wireless links, such as to interconnect two Mobile Subsystems (via the Radio Access Points), to interconnect a MS and a LAS or to interconnect a LAS with a WAS.

This chapter has presented a description of the AAL2 standard, as defined by the ITU-T recommendation I.363.2. In addition we have illustrated how the AAL2 standard can be used to improve the bandwidth utilization in point-to-point wireless ATM links, as illustrated in the NATO Post-2000 communications architecture.

In Chapter 3 we present a study of the analytical models that are commonly used for the characterization of the error-prone wireless links. The analytical models described in this chapter are of great importance in the derivation of analytical expressions which are used in subsequent chapters to evaluate diverse performance metrics of interest at the AAL2 layer.

Chapter 3 Wireless Channel Characterization

3.1 Introduction

There are several publications related to the modeling of wireless channels. One very well known model is the Jake's model [24], which describes the fading process over the wireless channel as a Gaussian process. However, for this type of models it is difficult to derive analytical system performance parameters, which are of interest in the evaluation of a digital communication system over wireless links [34]. Other well-known analytical channel models include the Discrete Memoryless Channel (DMC) models and the Hidden Markov Models (HMM).

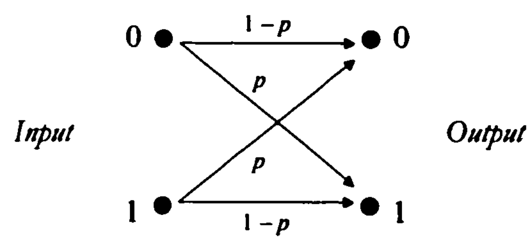

Figure 3.1: Transition diagram of a Binary Symmetric Channel.

The Binary Symmetric Channel (BSC) model is a special case of the DMC models. Figure 3.1 shows a transition diagram for a BSC model. Under the BSC a discrete-time input sequence $x_1, x_2, \ldots, x_n$ is mapped into a discrete-time output sequence $y_1, y_2, \ldots, y_n$. The input sequence is characterized by the elements of the input set $X = \{0, 1\}$, while the output sequence is characterized by the elements of the output set $Y = \{0, 1\}$. In addition, the BSC model has an associated set of conditional probabilities, which are related to the probability of observing a specific output element y_n given a specific input element x_n, as defined by,

$$Pr[y_n = 0 \mid x_n = 1] = Pr[y_n = 1 \mid x_n = 0] = p, \tag{1}$$

$$Pr[y_n = 1 \mid x_n = 1] = Pr[y_n = 0 \mid x_n = 0] = 1 - p. \tag{2}$$

The BSC is memoryless in the sense that errors occur at random intervals with a constant probability p [31]. However real wireless channels are subject to a variety of transmission impairments such as fading, interference and noise. Some of these impairments exhibit a significant degree of correlation [25], thus real wireless channels tend to have some memory, which causes errors to occur in bursts. It is for this reason that HMMs are extensively used throughout the literature [25 - 41] for the characterization of burst errors over error-prone wireless channels. In this work, the bit error process over the wireless channel is characterized by a HMMs unless specified otherwise.

Following the FSMC modeling approach, the wireless channel is characterized by a discrete-time Markov chain C_n, $n \geq 0$, where C_n is a random variable associated with the state of the channel at time instant n. Random variable C_n is defined in an N-dimensional state space $S = \{s_1, s_2, s_3, \ldots, s_N\}$, where $N \geq 2$. The time unit associated with the transitions in the Markov chain can be defined to be equal to the transmission time of one bit, the transmission time of one packet, or any other time unit frame of interest. In the context of this work, the time unit associated with the transitions of the Markov chain model is assumed to be equal to the transmission time of one bit, unless explicitly defined otherwise. Another characteristic of the FSMC models is that each state s_k has an associated probability of bit errors, which is directly related to the bit error process experienced at the receiving node.

The bit error process at the receiving node can be defined by a discrete-time random variable E_n, $n \geq 1$, where

$$E_n = \begin{cases} 0 & \text{If } n\text{-th bit is not in error,} \\ 1 & \text{Otherwise.} \end{cases} \tag{3}$$

In general, the bit error process E_n depends on the state of the Markov chain at time instants $n - 1$ and n. That is, the value of the error process at the end of a transition from state $C_{n-1} = i$ to state $C_n = j$ depends on both states i and j according to the probability distributions

$$p_{1,ij} = Pr[E_n = 1, C_n = j \mid C_{n-1} = i], \tag{4}$$

$$p_{0,ij} = Pr[E_n = 0, C_n = j \mid C_{n-1} = i] = 1 - p_{1,ij}, \tag{5}$$

where $i, j \in S$.

The special case, were E_n depends solely on C_n or C_{n-1} is most commonly used in practice because it is easier to associate the parameter of the analytical model to the parameter of the physical channel. The case where E_n depends on C_n only is considered in this work. In other words, the bit error process E_n is independent from the previous time instant C_{n-1}. Then Expression (4) can be re-written as

$$\begin{aligned} p_{1,ij} &= Pr[E_n = 1, C_n = j \mid C_{n-1} = i] \\ &= Pr[E_n = 1, C_n = j, C_{n-1} = i] / Pr[C_{n-1} = i] \\ &= Pr[C_{n-1} = i] Pr[C_n = j \mid C_{n-1} = i] Pr[E_n = 1 \mid C_n = j, C_{n-1} = i] / Pr[C_{n-1} = i] \\ &= Pr[E_n = 1 \mid C_n = j] Pr[C_n = j \mid C_{n-1} = i] \\ &= p_e(j) Pr[C_n = j \mid C_{n-1} = i], \end{aligned} \tag{6}$$

where $p_e(j) = Pr[E_n = 1 \mid C_n = j]$, $0 \leq p_e(j) \leq 1$. That is, given that the state of the channel during the transmission of the n-th bit is j, $C_n = j$, then the n-th bit in the bit-stream of information is in error with probability $p_e(j)$.

Figure 3.2 shows a simplified block diagram for the wireless channel where X_n represents the information bits transmitted, at time instants n = 1, 2, 3, ..., over the wireless channel. The received information bits are represented by $Y_n = X_n \oplus E_n$, where $\oplus$ is defined as the modulo-2 addition.

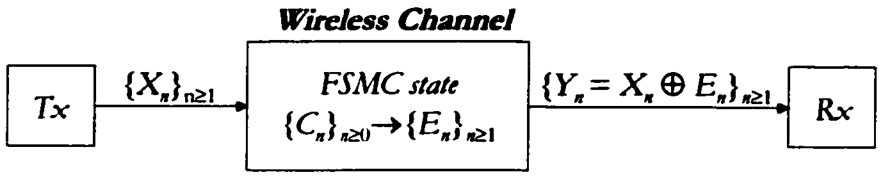

Figure 3.2: Wireless channel block diagram.

In this chapter, two approaches are presented for the characterization of the wireless link using FSMC models. One of these approaches is centered in modeling the bit error process at the receiver by statistically characterizing the "birth" and "death" process of the burst-error and error-free events. The Gilbert-Elliott model [27, 28] is a common example of this approach. The second approach characterizes the bit error process at the receiver by modeling the physical dynamics of the fading process. This last approach is considered a more general model for the characterization of the error process, as the burst-error and error-free events are a function of the fading dynamics of the wireless link.

3.2 Gilbert-Elliott Model

The Gilbert-Elliott model is characterized by a two-state (N = 2) Markov chain C_n, $n \geq 0$, where C_n is a random variable associated with the state of the channel at time instant n. Figure 3.3 shows the state transition diagram for the Gilbert-Elliott model.

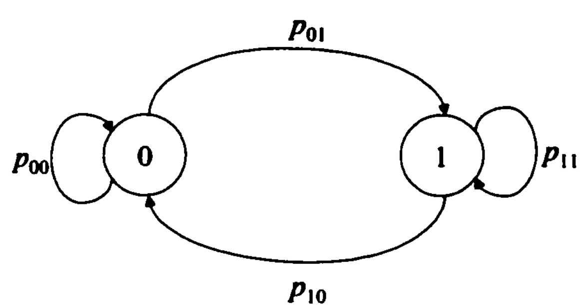

Figure 3.3: Gilbert-Elliott channel model.

Under the Gilbert-Elliott model, the physical channel assumes one of two states. One state is associated with a low probability of bit errors (state 0 or "good" state), while the other state is associated to a high probability of bit errors (state 1 or "bad" state). Thus, each state has an associated error probability $P_e(k)$, $k = 0, 1$.

The original model proposed by Gilbert [28] assumed a probability of bit error equal to zero for the "good" state (i.e., $P_e(0) = 0$) and a non-zero probability of bit errors in the "bad" state (i.e., $P_e(1) \neq 0$). Later, Elliott generalized Gilbert's model by allowing a non-zero error probability for the "good" state (i.e., $P_e(0) \neq 0$) [27]. In the generalized Gilbert-Elliott model the probability of bit errors in the "good" state is assumed to be lower than in the "bad" state (i.e., $P_e(0) << P_e(1)$). It should be noted there is an associated BSC to each state s_k of the Gilbert-Elliott model.

The state error probability vector $\mathbf{P_e}$ is defined as,

$$\mathbf{P_e} = \begin{bmatrix} P_e(0) & P_e(1) \end{bmatrix}. \tag{7}$$

The transition probability matrix, $\mathbf{P}$, of C_n, $n \geq 0$, is composed by the elements p_{ij}, where p_{ij} is defined as the probability of a transition from state i into state j. The transition probability matrix, $\mathbf{P}$, is denoted by

$$\mathbf{P} = \begin{bmatrix} p_{00} & p_{01} \\ p_{10} & p_{11} \end{bmatrix}, \tag{8}$$

and the stationary probability vector $\boldsymbol{\pi}$ is given by

$$\boldsymbol{\pi} = \begin{bmatrix} \pi_0 & \pi_1 \end{bmatrix} = \begin{bmatrix} \dfrac{p_{10}}{p_{01} + p_{10}} & \dfrac{p_{01}}{p_{01} + p_{10}} \end{bmatrix}. \tag{9}$$

The steady state channel bit error rate (BER), ε, of the Gilbert-Elliott model is given by

$$\varepsilon = \frac{P_e(0)p_{10} + P_e(1)p_{01}}{p_{01} + p_{10}}, \tag{10}$$

where $P_e(k)$ is the channel error probability in state k.

For Markov chain C_n, $n \geq 0$, the time spent in the state 1 (0) is geometrically distributed with mean $1/p_{10}$ $(1/p_{01})$. The mean burst length, τ, for the model is considered to be the time spent in the state 1, and is given by $\tau = 1/p_{10}$.

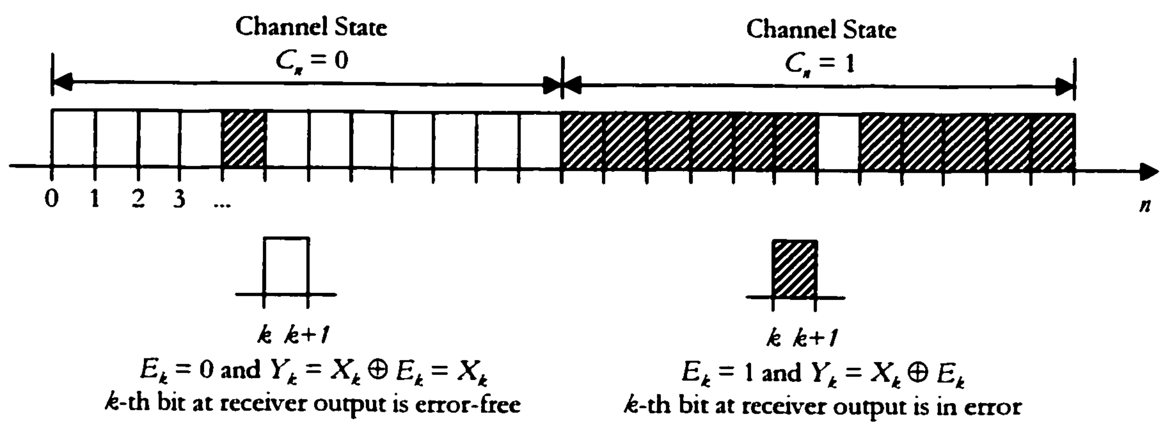

Figure 3.4: Sample realization of the bit error process E_n, $n \geq 1$.

From the definition of the Gilbert-Elliot channel model it is easy to observe that the bit error process E_n at the receiver becomes a function of the channel state C_n, $n \geq 0$, during which bit errors occur randomly with probability $P_e(k)$, $k = 0, 1$. Figure 3.4 shows a sample realization of the bit error process E_n, $n \geq 1$. For a given channel bit error rate, ε, and selected values of $P_e(0)$ and $P_e(1)$ the Expressions (8) and (9) can be represented in terms of the mean burst length, τ.

$$\mathbf{P} = \begin{bmatrix} 1-\alpha/\tau & \alpha/\tau \\ 1/\tau & 1-1/\tau \end{bmatrix}, \tag{11}$$

$$\boldsymbol{\pi} = \begin{bmatrix} \dfrac{1}{1+\alpha} & \dfrac{\alpha}{1+\alpha} \end{bmatrix}, \tag{12}$$

where α is defined as

$$\alpha = \frac{\varepsilon - P_e(0)}{P_e(1) - \varepsilon}. \tag{13}$$

The Gilbert-Elliott model is used extensively through out this work, as it provides a simple and suitable analytical work frame to derive performance metrics of interest for the transmission of AAL2 packets over wireless ATM links. It should be noted that the Gilbert-Elliott model is a simple 2-state Markov chain. However simplified models often provide enough insights into the underlying principles of the systems behaviour, which may be obscured by dealing with a myriad of details in more elaborate, though more accurate, models. Using the Gilbert-Elliott model it is easy to observe the system behaviour as a function of the burst error length τ for a given channel bit error rate, ε. Nevertheless, it is some times more useful to characterize the wireless channel using more elaborate models. Such is the case when modelling a system with diversity. For this type of channels (i.e., channels with diversity) it is not a straight forward issue to statistically characterize the "birth" and "death" process of the burst-error and error-free events. Under this situation, it is more useful to characterize the fading dynamics of the channel using an N-dimensional Finite State Markov Chain model to characterize the fading dynamics of the channel. Section 3.3 deals with the characterization of such wireless channels.

3.3 Modeling the Fading Dynamics of the Channel

The second approach for the characterization of the wireless channel is by defining a Finite State Markov Chain (FSMC) as a function of the fading process. A FSMC model can be derived from the fading dynamics of the channel by appropriately partitioning the dynamic range of the received Signal-to-Noise Ratio (SNR), γ, into a finite number, N, of non-overlapping intervals, such as, $[0, \gamma_1)$, $[\gamma_1, \gamma_2)$, ..., $[\gamma_{N-1}, \gamma_N)$, where $\gamma_N \rightarrow \infty$ [29]-[30], as shown in Figure 3.5. Each of the non-overlapping intervals represents a state in the resulting FSMC model and the channel is said to be in state s_k if $\gamma \in [\gamma_{k-1}, \gamma_k)$.

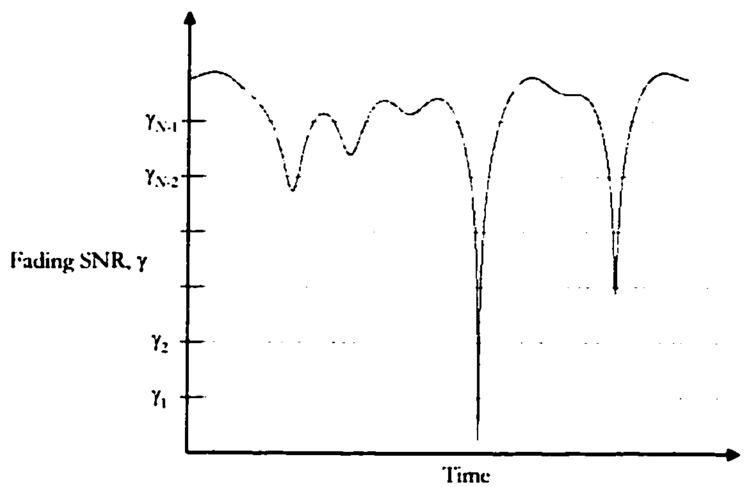

Figure 3.5: Partitioning of the fading dynamic range.

The FSMC model, which characterizes the fading dynamics of the channel, is uniquely defined by the transition probability matrix $\mathbf{P}$, the steady state vector $\boldsymbol{\pi}$ and the state error probability vector $\mathbf{P_e}$. The transition probability matrix, $\mathbf{P}$, is defined as an $N \times N$ matrix with elements p_{ij}, $i, j \in \{1, 2, \ldots, N\}$, where p_{ij} is defined as the probability of a transition from state i into state j, and is given by

$$p_{ij} = \frac{Pr\left[\gamma_{i-1} \leq \gamma' < \gamma_i, \gamma_{j-1} \leq \gamma'' < \gamma_j\right]}{Pr\left[\gamma_{i-1} \leq \gamma' < \gamma_i\right]} = \frac{\int_{\gamma_{j-1}}^{\gamma_j} \int_{\gamma_{i-1}}^{\gamma_i} f_{\Gamma',\Gamma''}(\gamma', \gamma'') d\gamma' d\gamma''}{\int_{\gamma_{i-1}}^{\gamma_i} f_{\Gamma'}(\gamma') d\gamma'}, \tag{14}$$

where $f_{\Gamma',\Gamma''}(\gamma', \gamma'')$ is the joint probability density function (jpdf) of Γ' and Γ'', $f_{\Gamma'}(\gamma')$ is the probability density function (pdf) of Γ', and Γ', Γ'' are random variables defining the fading instants of interest.

According to [30] the partitioning of the fading dynamics of the channel can be derived from the steady state probabilities of the FSMC model, which are evaluated following a recursive algorithm that is given by

$$\pi_k = \begin{cases} \dfrac{1}{2^N - 1} & k = 1 \\ 2 \cdot \pi_{k-1} & k = 2, \ldots, N \end{cases} . \tag{15}$$

The state error probability vector, $\mathbf{P_e}$, is composed by the elements $P_e(k)$, $k = 1, 2, \ldots, N$. It should be noted that the error probability $P_e(k)$, associated to each state s_k, is a function of the statistical time varying nature of the fading channel. That is, $P_e(k)$ can be defined in terms of the probability density function that characterizes the statistical fading dynamics of the channel. Then the state error probability $P_e(k)$ is given by

$$P_e(k) = \frac{1}{\pi_k} \int_{\gamma_{k-1}}^{\gamma_k} f_\Gamma(\gamma) \cdot e(\gamma) d\gamma , \tag{16}$$

where $p_\Gamma(\gamma)$ is the probability density function (pdf) of the SNR (γ), and $e(\gamma)$ represents the error probability as a function of the SNR (γ), which is closely related to the modulation/demodulation scheme.

Table 2: Bit error probability $e(\gamma)$ for different modulation schemes.

Modulation Scheme	$e(\gamma)$
Binary Phase Shift Keying (BPSK)	$Q\left(\sqrt{2\gamma}\right)$
Quadrature Phase Shift Keying (QPSK)	$Q\left(\sqrt{2\gamma}\right)$
Coherent Binary Frequency Shift Keying (BFSK)	$Q\left(\sqrt{\gamma}\right)$
Non-coherent Binary FSK	$\frac{1}{2}\exp\left(-\frac{\gamma}{2}\right)$

The probability of bit error, $e(\gamma)$, can be evaluated for many modulation schemes over Additive White Gaussian Noise (AWGN) and can be defined in terms of the Q-function, which is given by,

$$Q(x) = \int_x^\infty \frac{1}{\sqrt{2\pi}} \exp\left(-\frac{x^2}{2}\right) dx. \tag{17}$$

Table 2 shows the error probability, $e(\gamma)$, for some common modulation techniques [42].

3.4 Modeling of Flat Fading Channels

The analytical characterization of the wireless channel can be achieved by implementing a FSMC model, as described in Sections 3.2 and 3.3. In particular, Section 3.3 describes the derivation of a FSMC based on the dynamics of the fading process (i.e., it is related to the statistical time varying nature of the fading signal).

Based on the multipath time delay spread characteristics of the fading channel, the channel will behave as a flat fading or frequency selective channel. As defined in [42], "if a mobile radio has a constant gain and linear phase response over a bandwidth which is greater than the bandwidth of the transmitted signal, then the signal will undergo flat fading". Similarly from [42], "if the channel possesses a constant-gain and linear phase response over a bandwidth that is smaller than the bandwidth of the transmitted signal, then the channel creates frequency selective fading on the received signal". In addition, based on the Doppler spread a channel can be classified as a slow fading or fast fading channel [42].

In this work we are concerned with the flat fading channels. This section presents some of the most common probability density functions that are used to characterize the fading dynamics of the flat fading wireless channels.

3.4.1 Rayleigh Model

The Rayleigh distribution is commonly referred to model multipath fading with no direct line-of-sight (LOS) path. This model describes the statistical time varying nature of the fading amplitude, α, of the received signal over a flat fading channel. The probability density function (pdf) of a Rayleigh distributed random variable A, is given by [43, Eq. (2.6)]

$$f_A(\alpha) = \frac{2\alpha}{\Omega}\exp\left(-\frac{\alpha^2}{\Omega}\right), \quad \alpha \geq 0 \tag{18}$$

where $\Omega = \overline{\alpha^2}$ is the mean-square value of the fading amplitude α. Figure 3.6 shows the pdf of a Rayleigh distributed random variable, the plot assumes a normalized mean-square value, that is, $\Omega = 1$.

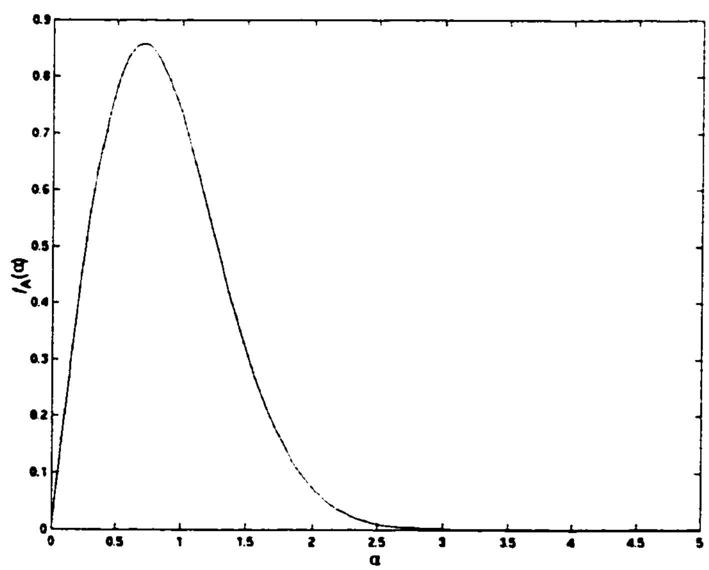

Figure 3.6: The pdf of a Rayleigh distributed random variable.

Some times it is more convenient to work with the pdf of the SNR, γ, which is proportional to the square of the signal amplitude, α. The pdf of a Rayleigh distributed random variable Γ, is given by [43, Eq. (2.7)]

$$f_{\Gamma}(\gamma) = \frac{1}{\bar{\gamma}} \exp\left(-\frac{\gamma}{\bar{\gamma}}\right), \quad \gamma \geq 0 \tag{19}$$

where $\bar{\gamma} = \mathrm{E}[\Gamma]$.

3.4.2 Nakagami-*n* (Rice) Model

When there is a dominant stationary (direct non-fading) signal component present, such as a line-of-sight (LOS) propagation path, the small-scale fading amplitude distribution of the signal amplitude, α, follows a Nakagami-*n* (Rice) distribution. The probability density function (pdf) of a Nakagami-*n* distributed random variable, A, is given by [43, Eq. (2.15)]

$$f_{\mathrm{A}}(\alpha) = \frac{2(1+n^2)e^{-n^2}\alpha}{\Omega} \exp\left[-\frac{(1+n^2)\alpha^2}{\Omega}\right] I_0\left(2n\alpha\sqrt{\frac{1+n^2}{\Omega}}\right), \quad \alpha \geq 0 \tag{20}$$

where $I_0(\cdot)$ is the zero-order modified Bessel function of the first kind, and n is the Nakagami-*n* fading parameter, which ranges from 0 to ∞. The Nakagami-*n* fading parameter n is related to the Ricean K factor by $K = n^2$ [43]. Figure 3.7 shows the pdf of a Ricean distributed random variable, the plot assumes a Ricean factor equal to K = 6 dB and a normalized mean-square value $\Omega = 1$.

The pdf for the SNR of a Nakagami-*n* distributed random variable Γ, is given by [43, Eq. (2.16)]

$$f_{\Gamma}(\gamma) = \frac{(1+n^2)e^{-n^2}}{\bar{\gamma}} \exp\left[-\frac{(1+n^2)\gamma}{\bar{\gamma}}\right] I_0\left(2n\sqrt{\frac{(1+n^2)\gamma}{\bar{\gamma}}}\right), \quad \gamma \geq 0 \tag{21}$$

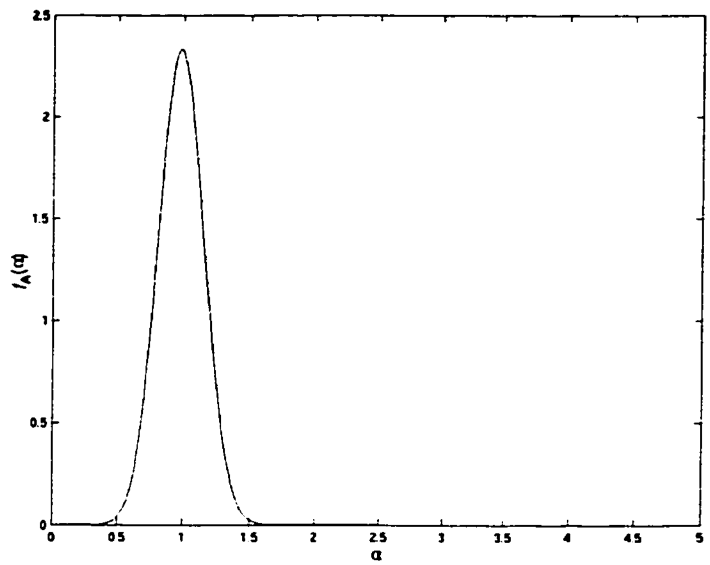

Figure 3.7: The pdf of a Rice distributed random variable.

3.4.3 Nakagami-*m* Model

The Nakagami-*m* distribution arises as an approximate solution to the general problem of the distribution of the magnitude of the sum of random vectors [44], whereas the Rayleigh and Ricean distributions are the particular solutions to the above problem [45].

One interesting characteristic of the Nakagami-*m* distribution is that it includes the Rayleigh distribution, as a special case (m = 1), and it also approximates the Ricean and Lognormal distributions [29]. Thus, the analytical derivations following the Nakagami-*m* distribution can easily be generalized to evaluate the Rayleigh and the Ricean fading channels.

The probability density function (pdf) of a Nakagami-m distributed random variable, A, is given by [43, Eq. (2.20)]

$$f_A(\alpha) = \frac{2\alpha^{2m-1}}{\Gamma(m)}\left(\frac{m}{\Omega}\right)^m \exp\left[-\frac{m\alpha^2}{\Omega}\right], \quad \alpha \geq 0 \tag{22}$$

where m is the Nakagami-m fading parameter, which ranges from ½ to ∞. Figure 3.8 shows the pdf of a Nakagami-m distributed random variable, the plot assumes a normalized mean-square value $\Omega = 1$.

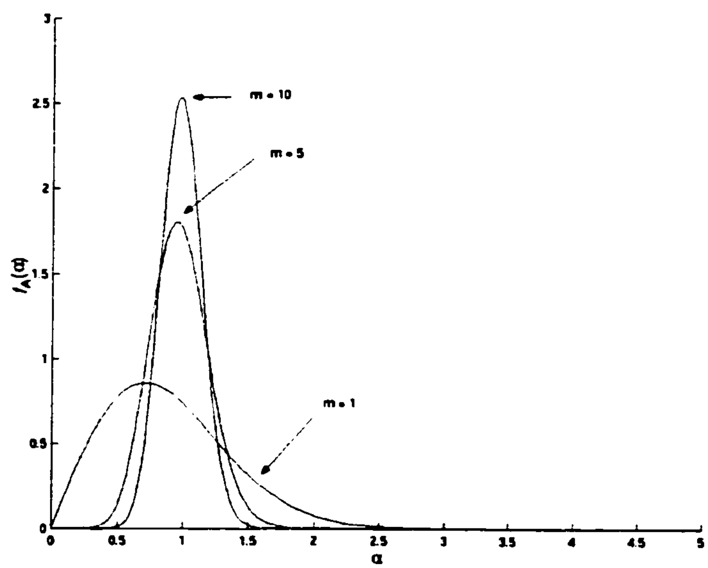

Figure 3.8: The pdf of a Nakagami-m distributed random variable.

The pdf for the SNR of a Nakagami-m distributed random variable Γ, is given by [43, Eq. (2.21)]

$$f_\Gamma(\gamma) = \frac{m^m \gamma^{m-1}}{\bar{\gamma}^m \Gamma(m)} \exp\left(-\frac{m\gamma}{\bar{\gamma}}\right). \quad \gamma \geq 0 \tag{23}$$

The Nakagami-*m* fading distribution can approximate the Nakagami-*n* (Rice) distribution by appropriately mapping the Ricean fading parameter *n* to the Nakagami-*m* fading parameter *m*. This mapping is given by [43, Eq. (2.26)]

$$m = \frac{(1+n^2)^2}{1+2n^2}. \quad n \geq 0 \tag{24}$$

The Nakagami-*m* distribution is of special interest in this work, as it is possible to statistically characterize a diverse number of flat fading distributions, as previously described (i.e., Rayleigh, Rice and Lognormal distributions). It is for this reason that the derivation of the FSMC models required for the characterization of the fading dynamics of the wireless channel (e.g., in the analysis of channels with diversity) are based on the Nakagami-*m* distribution.

Chapter 4 Performance Analysis of AAL2 over WATM

4.1 Introduction

The ATM Adaptation Layer 2 has been standardized by the ITU-T for the support of low data rate and delay sensitive traffic over ATM networks. Throughout the literature there are several research studies dealing with the performance of the AAL2 standard [46 - 54]. However most of these studies focus on how the AAL2 standard improves bandwidth utilization, as compared to other ATM adaptation layers, such as the AAL1, the AAL3/4 or the AAL5 [46, 47, 53]. Other studies focus on other performance metrics, such as, packetization delays or the optimization of AAL2 related parameters, such as the Timer_CU, aiming to improve the efficiency of the AAL2 standard [13, 14, 48, 52].

The AAL2 standard defines a new frame structure within the payload of the ATM cell and as a result the AAL2 standard introduces a mechanism for the delineation of AAL2 packets in the ATM payload. The delineation of the AAL2 packets is achieved by relying on the information that is provided as part of the STF and the CPS-PH (i.e., the AAL2 packet header) fields. Some of the ATM and AAL2 headers provide for limited error correction capability, such as the HEC field in the ATM header, while other header fields (e.g., the STF and the CPS-PH) do not provide for any error correction support. For example, the STF field has a single parity bit. This parity bit provides an extremely limited error control capability (e.g., a single parity bit cannot detect an even number of bit errors over the STF field). On the other hand each AAL2 packet has a 3 byte CPS-PH and each CPS-PH is composed by a 5-bit HEC field. The HEC field in the CPS-PH is not capable of correcting bit errors in the AAL2 packet header.

In this chapter, we are concerned with evaluating the performance of the AAL2 standard over an error-prone channel. The error-prone channels, such as wireless links, will introduce bit errors in the structure of the ATM and the AAL2 frames and the ATM and the AAL2 header fields are exposed to these channel impairments. Thus we are interested in deriving analytical expressions to evaluate performance metrics of interest (e.g., the loss probability) at the AAL2 layer.

This chapter is divided into five sections. Section 4.2 presents the analysis for the derivation of performance metrics of interest at the AAL2 layer over FSMC models. In Section 4.3 the numerical results over the Gilbert-Elliott channel are presented to evaluate the performance of the AAL2 standard over an error-prone channel. Section 4.4 presents the simulation results to validate the accuracy of the results obtained under the analytical derivation presented in Section 4.3. And Section 4.5 presents a brief summary of the analysis and the results presented throughout this chapter.

4.2 Performance Analysis of the AAL2 standard

The analysis of the AAL2 standard over FSMC channel models presented in the sequel considers the generic AAL2 CPS-PDU structure shown in Figure 4.1. The maximum number of CPS packets that can be accommodated in the CPS-PDU payload depends on the size of the CPS packets. Because the AAL2 standard allows for a CPS packet to be mapped across CPS-PDU payload boundaries, the CPS-PDU payload may include M' bits between the beginning of the first AAL2 packet and the STF field, as illustrated in Figure 4.1. That is, if the size of an AAL2 packet is greater than the available space in the CPS-PDU, then the AAL2 packet will be mapped to a subsequent CPS-PDU in another ATM cell.

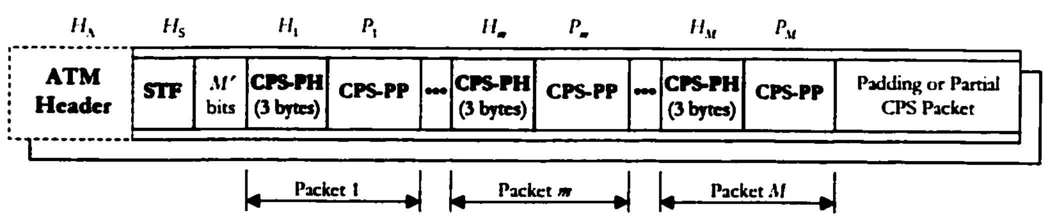

Figure 4.1: Standard AAL2 CPS PDU structure.

It should be noted that the analysis presented in this section applies to CPS packets that do not extend beyond the boundaries of the CPS-PDU, that is $M' = 0$ bits. This assumption is important in the derivation of closed form expressions for performance metrics of interest at the AAL2 layer.

The analysis begins by defining some useful notation. For convenience, the following notation is used to denote the different fields in the ATM cell structure depicted in Figure 4.1:

- H_A indicates the ATM cell header of size N_A bits ($N_A = 40$),
- H_S indicates the Start Field, STF, of size N_S bits ($N_S = 8$),
- H_m, $1 \leq m \leq M$, indicates the header of CPS packet m of size N_m bits ($N_m = 24$),
- P_m, $1 \leq m \leq M$, indicates the payload of CPS packet m of size L_m bits.
- M' is equal to the number of bits from a CPS packet that has exceeded the boundaries of the previous CPS-PDU.

It is assumed that the payload of an AAL2 CPS packet is successfully delivered to the next higher layer when all the relevant header and control fields in the ATM cell and the CPS-PDU are correct. That is, successful delivery of an AAL2 packet takes place when these fields are error-free or subject to correctable errors, whenever error correction is applied (as may be the case, for example, with the ATM cell header). The term "relevant headers" is defined as those headers on which an AAL2 packet must rely for it to remain delineated within the ATM payload. A CPS packet is considered lost (discarded) when at least one of the relevant header/control fields is subject to uncorrectable errors. For example, the CPS packet payload P_1 is considered lost when any of the headers H_A, H_S, or H_1 is corrupted by errors. Similarly, the CPS packet payload P_2 is lost when any of the headers H_A, H_S, H_1, or H_2 is corrupted. On the other hand, the CPS packet 1 is not affected by bit errors over the header of any subsequent AAL2 packets, as illustrated in Figure 4.2. In other words, the delineation of any given AAL2 packet m is not lost if H_n $\forall$ $n > m$ is corrupted by bit errors.

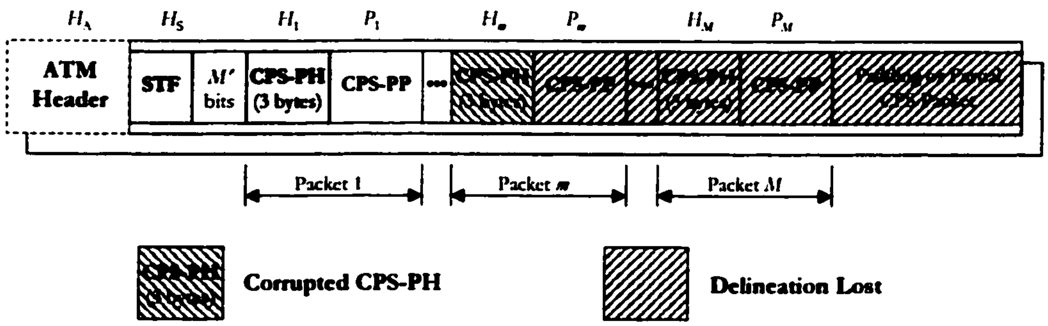

Figure 4.2: Delineation lost in the CPS-PDU.

The analysis presented in this section also accounts for the impact of undetectable errors on the performance of the AAL2 standard. Undetectable bit errors in the ATM or the AAL2 cell structure are treated as a special case of uncorrectable errors. This is explained by the fact that the analysis relies on the bit error process over the channel at the physical layer, which is characterized in this case by a FSMC model. In this way, undetectable errors at the ATM or AAL2 layers are only the result of multiple bit errors (more than the error correcting capability of the header error control mechanism); this case is accounted as an uncorrectable error case. In other words, the bit error process (as evaluated in the analysis) is observed at the physical layer. Therefore bit errors that may result in undetectable errors at higher layer are treated as bit errors that result in uncorrectable errors.

The following random variable definitions are associated with the CPS packets that are carried in the payload of an ATM cell and will be used through the analysis:

- β_m is equal to zero (0) if the CPS packet m is successfully delivered to the next higher layer. On the other hand, β_m is equal to one (1) if the CPS packet m is not successfully delivered to the next higher layer, due to corrupted ATM or AAL2 headers. For example, $\beta_1 = 0$ when the payload P_1 is delivered to the higher layers and $\beta_1 = 1$ when the payload P_1 is discarded at the ATM or the AAL layer.

- k_m denotes the number of errors in CPS packet payload P_m.

The joint probability of β_m and k_m is useful in the derivation of performance metrics of interest at the AAL2 layer.

When the channel is characterized by a FSMC model, the physical channel assumes one of N possible discrete states, each having an associated error probability $P_e(k)$, $k = 1, 2, \ldots, N$. Transitions on a N-dimensional state space $S = \{s_1, s_2, s_3, \ldots, s_N\}$ take place according to a N-state discrete-time Markov chain C_n, $n \geq 0$, where C_n is a random variable that denotes the channel state at time instant n. The analysis is facilitated by defining $\phi_{ij}(k, n)$ as the probability that exactly k bits are in error in $0, 1, \ldots, n-1$ time-units and the channel state at time instant n is j (i.e., $C_n = j$) given that the channel state at time instant 0 was i, (i.e., $C_0 = i$) [40]. Thus, $\phi_{ij}(k, n)$ is defined as,

$$\phi_{ij}(k,n) = Pr[C_n = j, U_n = k \mid C_0 = i], \tag{25}$$

where U_n is defined as the number of errors in a sequence of n bits, $U_n = \sum_{i=1}^{n} E_i$ and E_i is a random variable which takes a value equal to 0 if the i-th bit is error-free or a value equal to 1 if the i-th bit is in error.

The probabilities $\phi_{ij}(k, n)$ can be easily evaluated for $n \geq 0$, $0 \leq k \leq n$ in a recursive manner:

$$\begin{aligned}
\phi_{ij}(k,n) &= Pr[C_n = j, U_n = k \mid C_0 = i] \\
&= \sum_{m \in S} \sum_{k'=0}^{1} Pr[C_n = j, C_{n-1} = m, U_n = k, E_n = k' \mid C_0 = i] \\
&= \sum_{m \in S} \sum_{k'=0}^{1} Pr[C_n = j, C_{n-1} = m, U_{n-1} = k - k', E_n = k' \mid C_0 = i] \\
&= \sum_{m \in S} \sum_{k'=0}^{1} Pr[C_{n-1} = m, U_{n-1} = k - k' \mid C_0 = i] Pr[C_n = j, E_n = k' \mid C_{n-1} = m] \\
&= \sum_{m \in S} \sum_{k'=0}^{1} \phi_{im}(k - k', n-1) Pr[C_n = j, E_n = k' \mid C_{n-1} = m] \\
&= \sum_{m \in S} \left\{ \phi_{im}(k, n-1)\, p_{0,mj} + \phi_{im}(k-1, n-1)\, p_{1,mj} \right\},
\end{aligned} \tag{26}$$

where $p_{0,mj}$ and $p_{1,mj}$ define the probability that $C_n = j$ (i.e., the channel state at time unit n is j) given that $C_{n-1} = m$ (i.e., the channel state at time unit $n - 1$ is m) and E_n is equal to 0 or 1 respectively. These probabilities are evaluated by the Expressions (4) and (5).

Expression (26) can be use to keep track of the state of the channel, as well as, the number of error occurrences k in a block of n bits. Expression $\mathbf{\Phi}(k,n)$ will be used to denote the matrix with elements $\phi_{ij}(k, n)$, $i, j \in S$, $n \geq 0$, $0 \leq k \leq n$. Matrix $\mathbf{\Phi}(k,n)$ can be computed by using the following recursive algorithm: for $n = 0$, $k = 0$, $\mathbf{\Phi}(0,0) = \mathbf{I}$, where $\mathbf{I}$ is the identity matrix. For $n > 0$,

$$\mathbf{\Phi}(k,n) = \begin{cases} \mathbf{\Phi}(k,n-1)\mathbf{\Delta}_0 & k = 0 \\ \mathbf{\Phi}(k,n-1)\mathbf{\Delta}_0 + \mathbf{\Phi}(k-1,n-1)\mathbf{\Delta}_1 & 0 < k < n \\ \mathbf{\Phi}(k-1,n-1)\mathbf{\Delta}_1 & k = n \end{cases}, \tag{27}$$

where $\mathbf{\Delta}_0$ and $\mathbf{\Delta}_1$ are defined as

$$\mathbf{\Delta}_0 = (\mathbf{I} - \mathbf{D_e})\mathbf{P}\,,\ \mathbf{\Delta}_1 = \mathbf{D_e}\mathbf{P}\,, \tag{28}$$

where $\mathbf{P}$ is the transition probability matrix and $\mathbf{D_e}$ is defined as

$$\mathbf{D_e} = diag\{Pe(1), Pe(2), \ldots, Pe(N)\}. \tag{29}$$

Matrix $\mathbf{\Delta}_0$ accounts for the probability of no error occurrence after a one step transition, while matrix $\mathbf{\Delta}_1$ accounts for the probability of error occurrence after a one step transition.

The joint probability distribution of β_m and k_m is given by $Pr[\beta_m, k_m]$ and it can be easily evaluated as follows:

$$
Pr[\beta_m = 0, k_m = \ell] = \begin{cases} \sum_{i=0}^{1} \boldsymbol{\pi}\boldsymbol{\Phi}(i, N_A)\boldsymbol{\Phi}(0, N_S)\mathbf{P}^{M'}\boldsymbol{\Phi}(0, N_1)\boldsymbol{\Phi}(\ell, L_1)\mathbf{e} & m = 1 \\ \sum_{i=0}^{1} \boldsymbol{\pi}\boldsymbol{\Phi}(i, N_A)\boldsymbol{\Phi}(0, N_S)\mathbf{P}^{M'} \prod_{j=1}^{m-1} \boldsymbol{\Phi}(0, N_j)\mathbf{P}^{L_j}\boldsymbol{\Phi}(0, N_m)\boldsymbol{\Phi}(\ell, L_m)\mathbf{e} & 1 < m \leq M \end{cases}, \tag{30}
$$

$$
Pr[\beta_m = 1, k_m = \ell] = \boldsymbol{\pi}\boldsymbol{\Phi}(\ell, L_m)\mathbf{e} - Pr[\beta_m = 0, k_m = \ell], \tag{31}
$$

where $\boldsymbol{\pi} = [\pi_1, \pi_2, \ldots, \pi_N]$ is the steady state probability vector of C_n, $\mathbf{P}^{M'}$ is the M'-step transition probability matrix and $\mathbf{e} = [1, 1, \ldots, 1]^T$ is the unit column vector.

The single bit error correcting capability of the standard ATM HEC code is assumed in the derivation of the expressions above as reflected by the choice of values for index i in Expressions (30). That is, the HEC field in the ATM header is capable of correcting up to one bit in error. On the other hand, the STF as well as the CPS packet header, as defined in the ITU-T standard [12], do not provide for any error correction capability. It is assumed that a single bit error in the STF will disrupt the CPS packet delineation process causing the discard of the entire CPS-PDU payload.

The joint probability distribution $Pr[\beta_m, k_m]$ for a Binary Symmetric Channel (BSC) can be obtained from Expressions (30) and (31) by replacing the occurrences of matrix $\boldsymbol{\Phi}(k,n)$ by the scalar quantity $\Phi(k,n)$, which represents the probability that there are k errors in n bits. Expression $\Phi(k,n)$ is denoted by a binomial distribution and is given by

$$
\Phi(k,n) = \binom{n}{k} \varepsilon^k (1-\varepsilon)^{n-k}, \tag{32}
$$

where ε is the channel bit error rate.

Then for a Binary Symmetric Channel, as defined in Section 3.1, Expressions (30) and (31) become:

$$Pr[\beta_m = 0, k_m = \ell] = \sum_{i=0}^{1} \Phi(i, N_A)\Phi(0, N_S)\prod_{j=1}^{m} \Phi(0, N_j)\Phi(\ell, L_m), \tag{33}$$

$$Pr[\beta_m = 1, k_m = \ell] = \Phi(\ell, L_m) - Pr[\beta_m = 0, k_m = \ell]. \tag{34}$$

The joint probability distribution $Pr[\beta_m, k_m]$ can be used to evaluate several performance metrics of interest at the AAL2 layer. Define the mini-Cell Loss Rate (*mCLR*) as the probability that a CPS packet is lost due to uncorrectable errors in the ATM header, in the STF or in the CPS packet's header. Then the mini-Cell Loss Rate for the *m*-th AAL2 packets is just a marginal probability of Expression (31) and the mini-Cell Loss Rate for CPS packet *m* is given by

$$mCLR_m = Pr[\beta_m = 1] = \sum_{\ell=0}^{L_m} Pr[\beta_m = 1, k_m = \ell], \tag{35}$$

where L_m is the size of the payload of the *m*-th CPS packet. The *mCLR* can be used to evaluate the proposed ATM or AAL2 header protection schemes.

Another metric of interest is the probability of errors that is observed in the payload of those AAL2 packets that are not lost or discarded at the ATM or the AAL2 layers. Define the mini-cell Payload Error Rate (*mPER*) as the probability of errors in the payload of the CPS packets that are delivered by the AAL2 layer to the higher layers. Then the *mPER* is equal to the rate of bit errors $\bar{b}_E$ in the CPS packet payload given that the header/control fields (that affect the delivery of the CPS packet payload to the higher layers) are correct. The rate of bit errors $\bar{b}_E$ over the payload of the *m*-th AAL2 packet can be evaluated as the ratio between the average number of payload bit errors and the length of the CPS packet payload,

$$\bar{b}_E = \frac{1}{L_m} \sum_{\ell=0}^{L_m} \ell \cdot Pr[\beta_m = 0, k_m = \ell]. \tag{36}$$

The probability that the ATM and the AAL2 header fields are not corrupted by bit errors is given by the marginal probability,

$$Pr[\beta_m = 0] = \sum_{\ell=0}^{L_m} Pr[\beta_m = 0, k_m = \ell]. \tag{37}$$

Then, the mini-cell Payload Error Rate for CPS packet m is given by

$$mPER_m = \frac{\sum_{\ell=0}^{L_m} \ell \cdot Pr[\beta_m = 0, k_m = \ell]}{L_m \sum_{\ell=0}^{L_m} Pr[\beta_m = 0, k_m = \ell]}. \tag{38}$$

Finally, the mini-cell Payload Bit Error Rate (*mPBER*) is defined as the probability of errors seen by the higher layers, as a result of bit errors in the payload of non-discarded CPS packets and lost bits due to the discard of CPS packets. The probability of bit errors observed in the payload of non-discarded AAL2 packets is equal to the rate of bit errors in the payload of non-discarded AAL2 packets as defined in Expression (36). On the other hand, the probability of bit errors observed by the user of the AAL2 layer as a result of discarded AAL2 packets is equal to the probability of the AAL2 packets being discarded due to corrupted header fields, as defined in Expression (35). Then the mini-cell Payload Bit Error Rate for CPS packet m is given by

$$\begin{aligned} mPBER_m &= \sum_{\ell=0}^{L_m} \left[Pr[\beta_m = 1, k_m = \ell] + \frac{\ell}{L_m} Pr[\beta_m = 0, k_m = \ell] \right] \\ &= mCLR_m + \frac{1}{L_m} \sum_{\ell=0}^{L_m} \ell \cdot Pr[\beta_m = 0, k_m = \ell]. \end{aligned} \tag{39}$$

The *mPBER* provides an overall picture of the probability of bit errors experienced by the higher layers as it evaluates the combined impact of bit errors on the headers and the payload of the ATM and AAL2 frame structure. Then, *mPBER* can be used to evaluate the QoS requirements for the users of the AAL2 layer.

4.3 Performance Analysis of AAL2 over the Gilbert-Elliott Channel

In this section the numerical results for the performance metrics *mCLR*, *mPER* and *mPBER*, derived in Expressions (35), (38) and (39), are presented for the Gilbert-Elliott model. The CPS-PDU structure shown in Figure 4.3 is considered for the evaluation presented here in. The performance analysis assumes that the ATM cell does not carry information bits from a previous CPS packet (i.e., the analysis assumes that AAL2 packets cannot be mapped beyond the boundaries of the CPS-PDU and therefore $M' = 0$) and CPS packets are assumed to be of equal size. The channel BER for the Gilbert-Elliot Channel is $\varepsilon = 10^{-3}$ and the state error probabilities are equal to $P_e(0) = 0$ and $P_e(1) = 0.5$. Appendix B, Section B.1 presents the derivation of the Gilbert-Elliott model parameters that were used to derive the numerical results presented in this section.

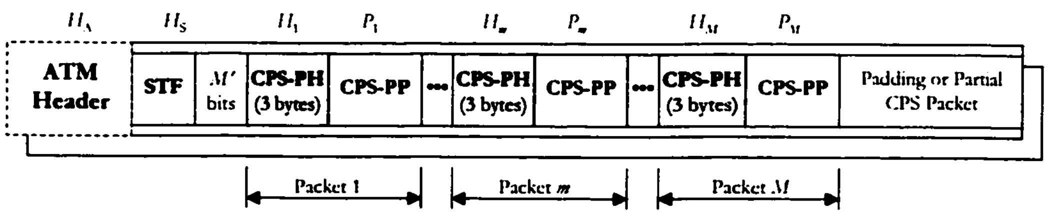

Figure 4.3: CPS-PDU structure used for numerical analysis.

Since one of the main characteristics of the AAL2 standard is its ability to multiplex information from multiple sources, it is of interest to study the performance of the AAL2 standard over the burst error channel for CPS packets with different payload (CPS-PP) sizes. There are several applications that have the characteristic of generating information that will result in AAL2 packets of variable size. For example, the ITU-T standard I.366.2 [18] defines several profiles that can be used for the transport of audio encoded data using the AAL2 standard. In Appendix A additional information is presented with respect to the standardized profiles for different audio encoders for the AAL2 standard.

The analysis presented in this section assumes CPS packets with different CPS-PP size, such as, CPS packets with payload size of 24 bits (small payload), 96 bits (intermediate payload) and 352 bits (large payload). The selection of a CPS-PP of 24 bits corresponds to the case with 50% overhead for each CPS packet, and the number of complete CPS packets within the CPS-PDU is seven (i.e., M = 7). The selection of CPS-PP equal to 96 bits corresponds to the case in which only three (i.e., M = 3) CPS packets fit completely within the CPS-PDU. Finally the selection of CPS-PP of size 352 bits corresponds to the case where one (i.e., M = 1) CPS packet fills the entire CPS-PDU payload.

The numerical results, in this section, are evaluated as a function of the mean burst length τ. The mean burst length τ is defined as the average time the channel, characterized by the Gilbert-Elliott model, is in the "bad" state (see Section 3.2). In the Gilbert-Elliot model the mean burst length τ is defined to be equal to

$$\tau = 1/p_{10}. \tag{40}$$

where p_{10} is defined as the probability of a transition from state "1" to state "0" (i.e., the probability of a transition from the "bad" state to the "good" state).

Figure 4.4 shows the performance results, as a function of the mean burst length τ, for each of the CPS packets in the CPS-PDU for the case CPS-PP of size 24 bits. For this case, the number of CPS packets that completely fill the CPS-PDU payload is M = 7.

From Figure 4.4 it is clear that the error performance, with respect to all metrics, improves as the mean burst length τ increases. As the value of τ increases ($\tau \rightarrow \infty$), *mCLR* and *mPBER* reach a limit, which can be shown to be equal to

$$mCLR(\infty) = 1 - \pi_0 - \pi_1 \left\{ [1 - P_e(1)]^{N_A} + N_A P_e(1) [1 - P_e(1)]^{N_A - 1} \right\} [1 - P_e(1)]^{N_S + N_1}, \tag{41}$$

while metric *mPER* decreases monotonically. This performance behaviour is attributed to the analytical model (Gilbert-Elliott) used for the characterization of the burst channel, as explained below.

(a)

(b)

(c)

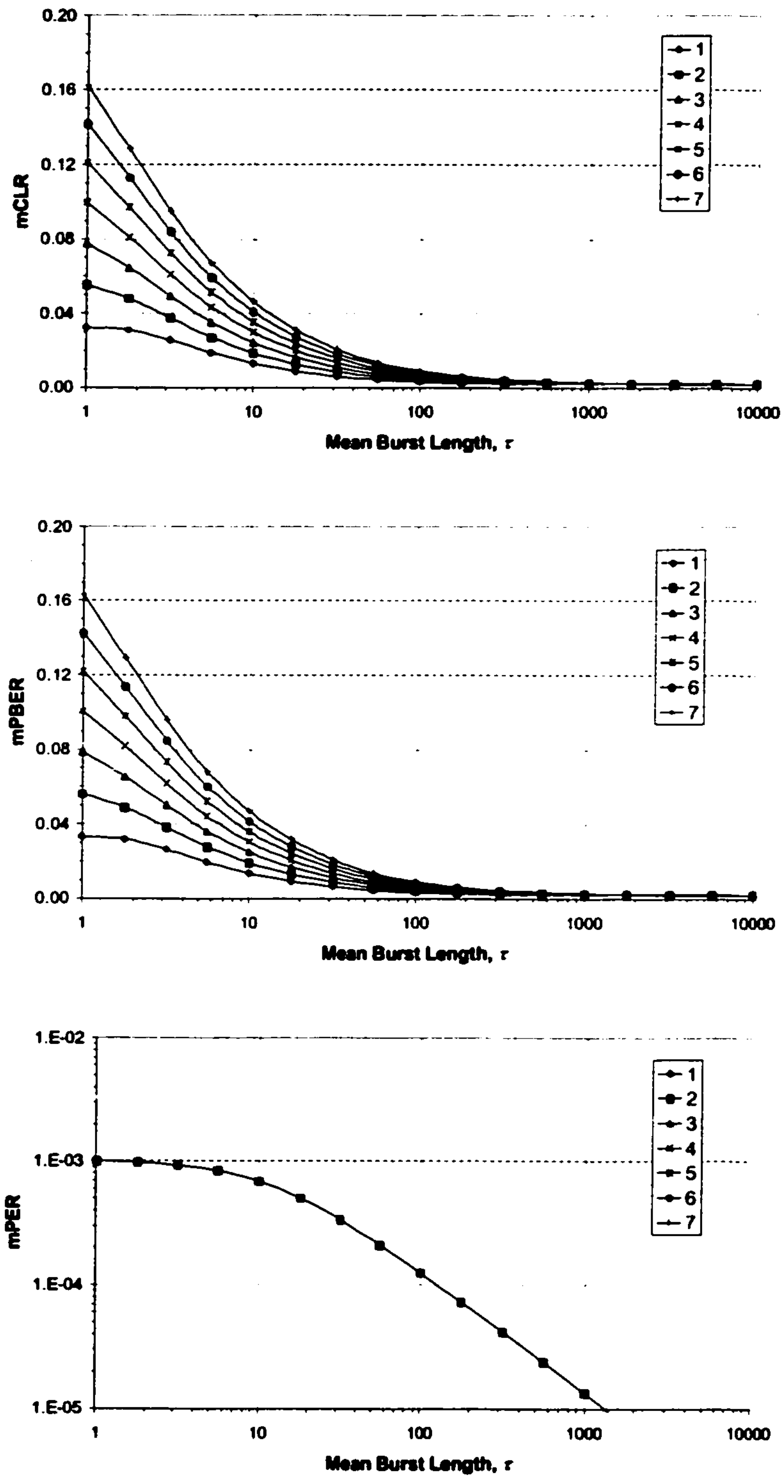

Figure 4.4: Performance metrics for CPS-PP size of 24 bits.

For large values of the mean burst length τ, the average time the channel model (i.e., the Gilbert-Elliott model) spends in the error-prone state (i.e., the "bad" state) increases. Similarly the average time the channel model spends in the error-free state (i.e., the "good" state) also increases, as the channel model BER is fixed. In the same way, as the mean bursts length τ decreases the average time the channel model spends in the error-prone and error-free states also decreases. Then large values of the mean burst length τ result in long, but infrequent, bursts of errors. Similarly, small values of τ result in small, but frequent, bursts of errors. An illustrative example of the error process for large and small values of τ is shown in Figure 4.5.

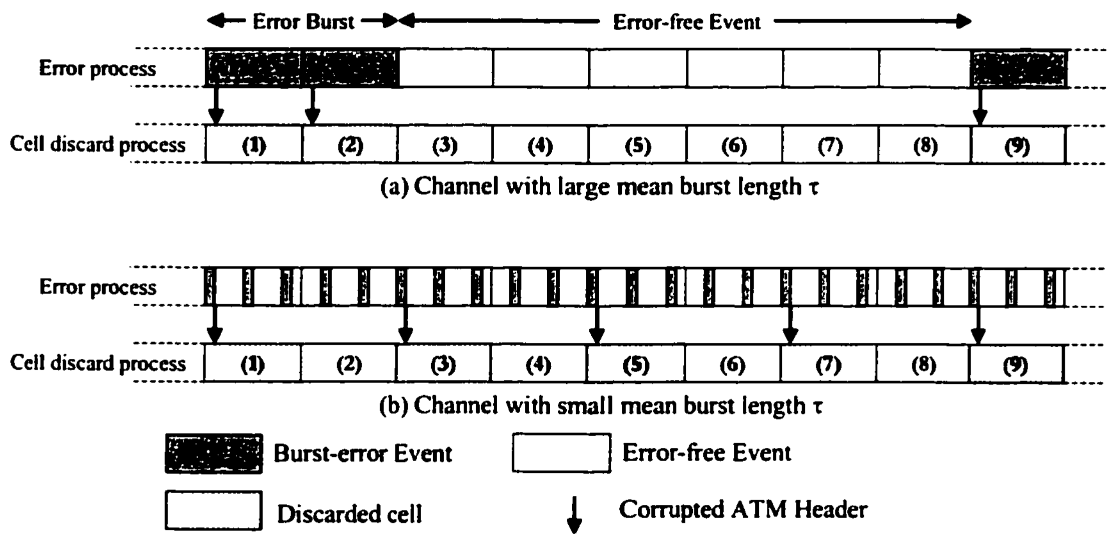

Figure 4.5: Burst error process.

For small values of τ, the ATM/AAL2 bit stream is affected by short and frequent error bursts, thus the probability of a header/control field being corrupted by errors, i.e. the *mCLR*, increases. Therefore, the *mCLR* performance degrades as τ decreases. For example, Figure 4.5 shows two events in which an ATM cell stream is exposed to an error-prone channel and therefore some bits are corrupted by bit errors. Figure 4.5(a) illustrates the case where the bit error process is characterized by long, but infrequent burst errors. On the other hand Figure 4.5(b) illustrates the case where the bit error process is characterized by small, but frequent burst errors. It should be noted that the channel BER is the same in both cases. From Figure 4.5(b) it is clear that the probability of a lost AAL2 packet (as a result of a greater number of lost ATM cells) is greater for small values of τ.

On the other hand, the performance behaviour of metric *mPER*, illustrated in Figure 4.4(c) can be explained as follows. For long error bursts spanning several ATM cells (large τ), the discarded CPS packets will very likely have several payload bits in error. Similarly, CPS packets that are not discarded will likely have error-free payloads. For example in Figure 4.5(a) (i.e., for a large mean burst length) the ATM cells 3, 4, 5, 6, 7 and 8 are not discarded and their corresponding payloads are error-free. On the other hand for a small mean burst length, illustrated in Figure 4.5(b), the ATM cells 2, 4, 6 and 8 are not discarded; however their payloads are corrupted by bit errors as illustrated by the error process. In this way, for large values of τ, the payload of the CPS packets delivered to the higher layers is more likely to be free of errors, and therefore performance metric *mPER* decreases as the mean burst length τ increases.

The Figure 4.6 shows the performance results for each of the CPS packets in the CPS-PDU for the case CPS-PP of size 96 bits. In this case, the number of CPS packets that completely fill the CPS-PDU payload is $M = 3$. It is interesting to note that the performance results for metrics *mCLR* and *mPBER*, shown in Figure 4.6(a) and Figure 4.6 (b) respectively, are similar to the results presented for the first three AAL2 packets with CPS-PP of size 24 bits, shown in Figure 4.4. This result is clearly related to the interdependency that exists between the AAL2 packets within a CPS-PDU, as a result of the delineation mechanism defined in the AAL2 standard. From the performance metric *mPER*, shown in Figure 4.6(c), it can be observed that the probability of errors on the payload of non-discarded AAL2 packets reaches the value of 10^{-5} for a mean burst length of $\tau \approx 5000$ bits. On the other hand for the AAL2 packets with CPS-PP of size 24 bits, metric *mPER* reaches the mark of 10^{-5} for a $\tau \approx 1500$. That is, the probability of bit errors in the payload of non-discarded AAL2 packets is greater for CPS-PP of size 96 bits than that of CPS-PP of size 24 bits. Figure 4.7 shows average performance results for all CPS packet sizes under consideration. From Figure 4.7(a) and Figure 4.7(b) it is observed that performance with respect to *mCLR* and *mPBER* improves for large CPS packet payloads. That is, the probability of losses is reduced for the ATM cells that carry CPS packets with large payloads.

(a)

(b)

(c)

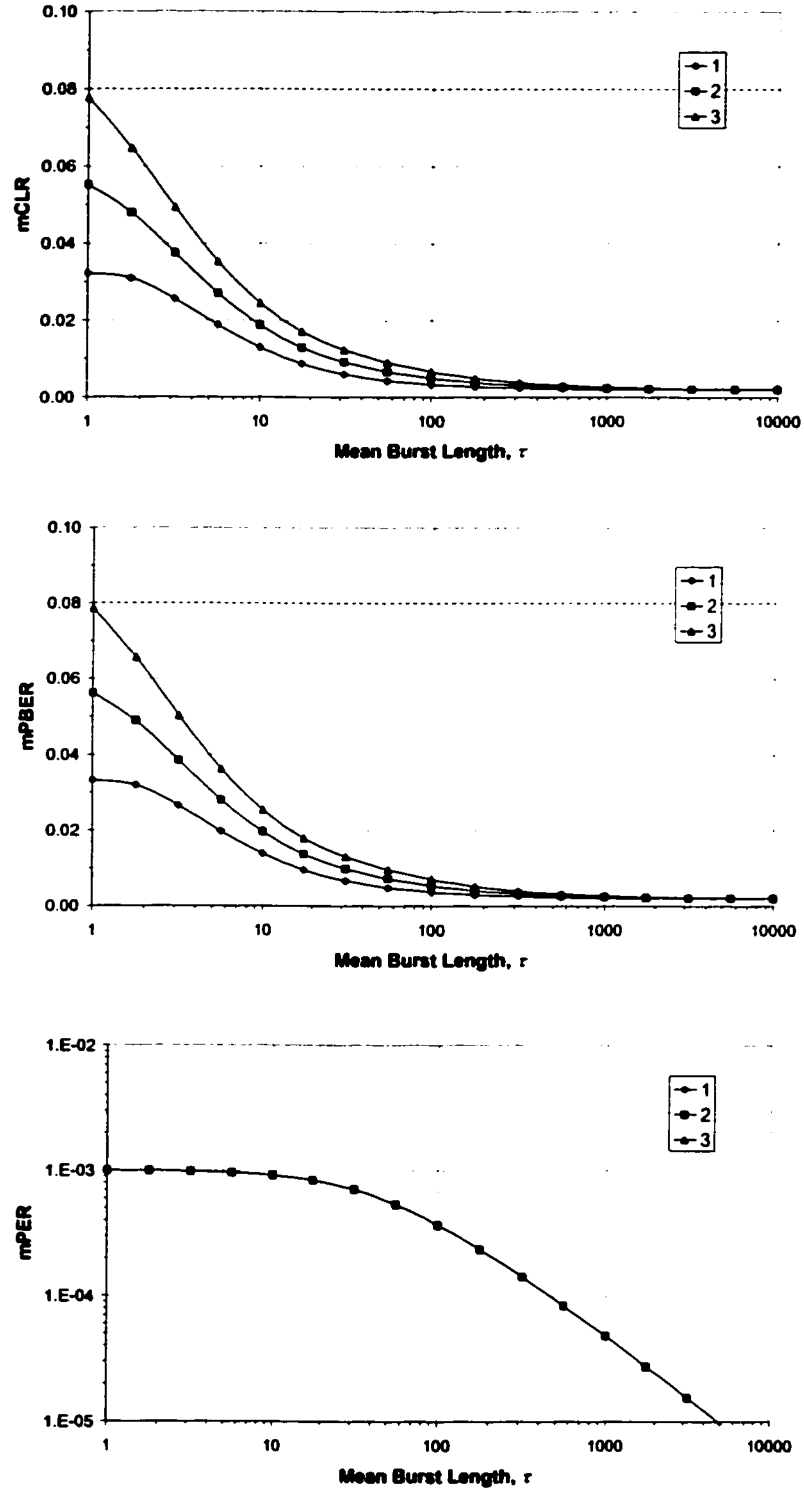

Figure 4.6: Performance metrics for CPS-PP size of 96 bits.

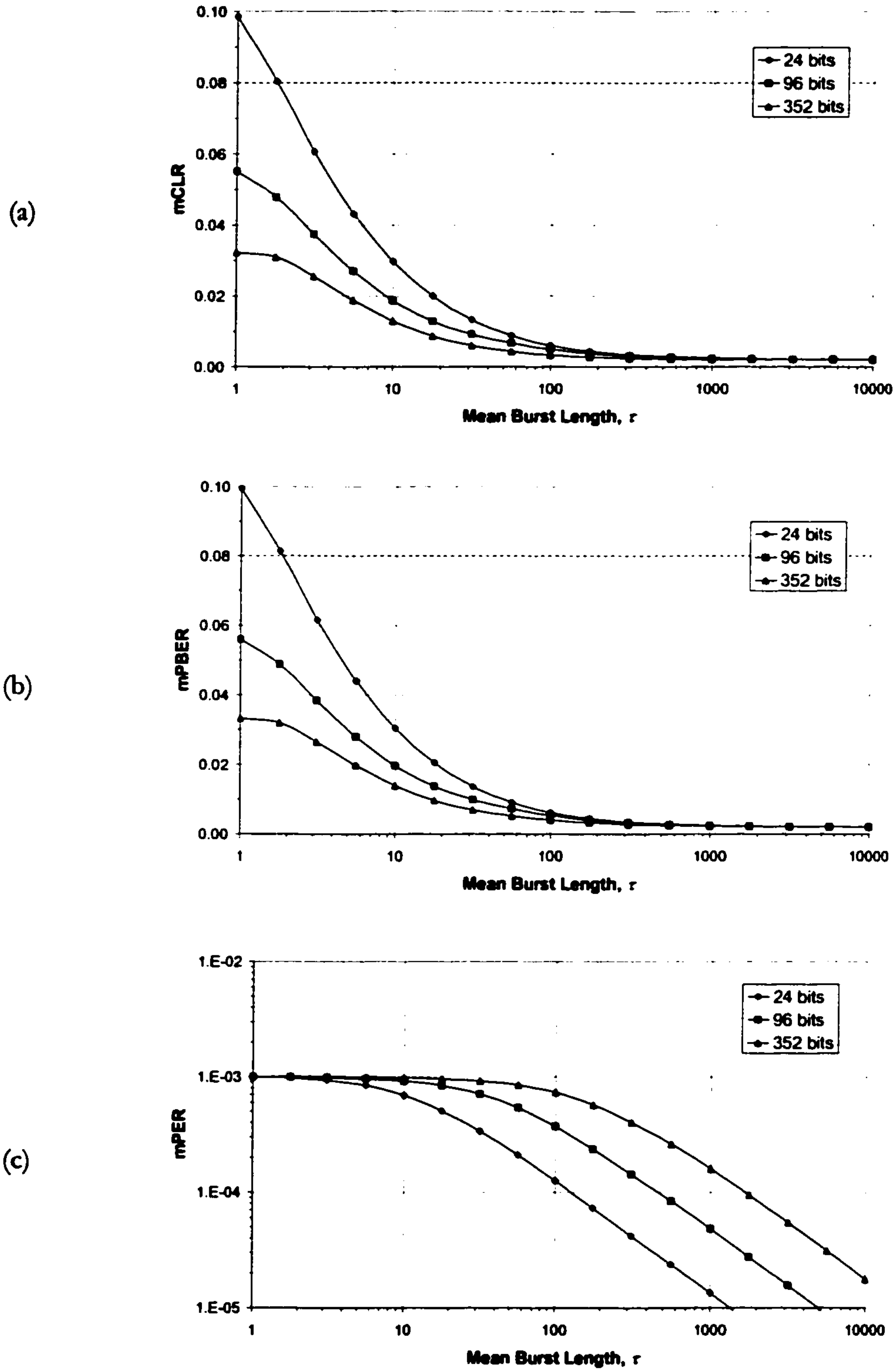

Figure 4.7: Average performance metrics.

For large CPS packet payloads the number of CPS packets that can be carried in the CPS-PDU decreases and so does the number of CPS packet headers, thus the probability of corrupted headers affecting CPS packet delineation is reduced, resulting in a decrease of CPS packet losses. Figure 4.7(c) shows the performance metric *mPER* for CPS packets of different payload size. Contrary to the behaviour exhibited by the performance metrics *mCLR* and *mPBER*, the performance with respect to metric *mPER* improves for CPS packets with small payload size. By definition, the metric *mPER* is associated with the rate of errors in the CPS packet payload given that the header/control fields are correct, and thus, metric *mPER* is a function of the error process affecting the CPS packet payload and the probability of errors in the CPS packet payload increases with the size of the payload. From these results it is clear that a system implementation using large CPS packet payloads will result in a reduced *mCLR* at the expense of increased *mPER* and packetization delays.

4.4 Performance Analysis Validation

Section 4.2 presented the performance analysis of the ATM Adaptation Layer 2 standard over a link characterized by a FSMC model and several performance expressions were derived to evaluate metrics of interest at the AAL2 layer. In Section 4.3, the numerical results were presented for the performance evaluation of the AAL2 standard over the Gilbert-Elliott channel model. However, it should be noted that the analysis presented in Section 4.2 relies on the transport of AAL2 packets that are not mapped beyond the boundaries of a single CPS-PDU. This assumption was introduced to simplify the derivation of closed form expressions, which are used to evaluate the performance metrics of interest at the AAL2 layer. Nevertheless, the AAL2 standard does allow for a single AAL2 packet to be mapped beyond the boundaries of a CPS-PDU (i.e., an AAL2 packet may be carried by one or two ATM cells). It is therefore important to evaluate the accuracy of the results derived from the analytical derivation presented in Section 4.2 and compare them with a "more realistic" implementation of the AAL2 standard.

This section presents the performance results obtained using the Network Simulator (ns-2) tool [55]. The simulation assumes two ATM nodes exchanging information over a FSMC modelled link. Figure 4.8 shows a block diagram of the network architecture implemented in the ns-2 simulation.

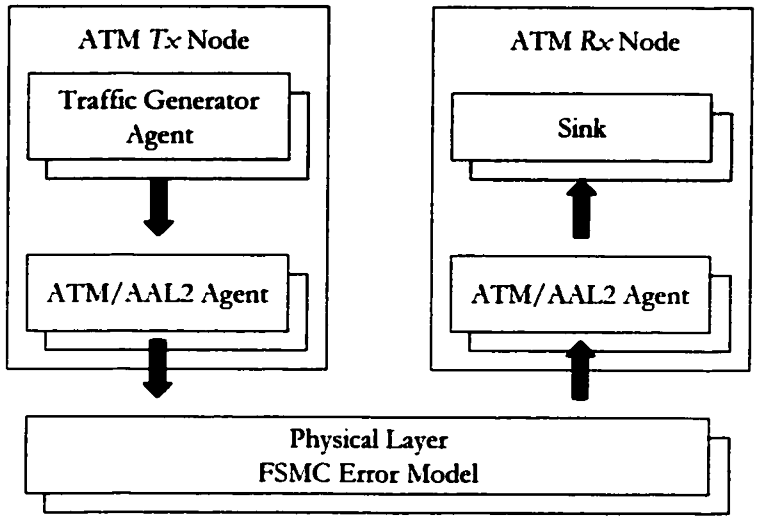

Figure 4.8: Block diagram of the ns-2 network architecture.

At the sender the Traffic Generator Agent generates 470 bytes of data every 4.24 ms. Recall that under AAL2 the first byte of the ATM payload corresponds to the Start Field (STF), thus 10 ATM cells are generated every 4.24 ms. The ATM/AAL2 Agent receives the information from the Traffic Generator Agent and encapsulates the information according to the standard AAL2 frame structure. Later the information is sent by the ATM/AAL2 Agent to the physical layer and transmitted over the link at a data rate of 1 Mbits/s. The size of the AAL2 packets is defined by a parameter specified as part of the simulation script. To keep track of the bit errors introduced by the link, a string of 424 bits (all equal to "1") is associated to each transmitted ATM cell. Bit errors introduced by the link will result in a bit switched from a value "1" to a value "0".

In the simulation, a FSMC model characterizes the error-prone channel. In this case the channel is characterized by a two-state Markov chain (i.e., Gilbert-Elliott model). Several parameters can be specified as part of the simulation script. These parameters include the channel BER, the mean burst length (i.e., the average time spent in the "bad" state) and the probability of bit error on each of the two states.

At the other end of the transmission link, the ATM cells are received and examined by the receiver's ATM/AAL2 Agent. If an ATM cell is flagged with bit errors, then the Agent will proceed to check the ATM and the AAL2 headers. The simulator assumes that the HEC code in the ATM header can correct up to one bit in error. The STF and the CPS-PH fields (i.e., AAL2 packet headers) do not provide for any error correction capability, as defined in the ITU-T AAL2 standard. Thus the AAL2 packets will be lost if there are two or more bit errors in the ATM cell header or if an AAL2 header field is corrupted by bit errors. In addition the ATM/AAL2 Agent keeps track of the bit errors on those AAL2 packets that are not lost or discarded at the ATM or AAL2 layer. Once the ATM cell has been inspected for bit errors it is sent to a sink module responsible of destroying the ATM cell.

The numerical results obtained with the ns-2 simulator are presented in Figure 4.9. These results are plotted against the mean burst length τ, which is defined to be the average time spent on the "bad" state of the two-state Markov link model.

The performance results shown in Figure 4.9 illustrate that the performance behaviour is similar to that of the performance results presented in Figure 4.7 in Section 4.3. The main difference between the results in Figure 4.9 and the results shown in Figure 4.7 is observed for small values of the mean burst lengths τ, as illustrated by performance metrics *mCLR* and *mPBER*. Table 3 lists the average *mCLR* results obtained using the analytical expression from Section 4.2, as well as, the numerical results obtained under the ns-2 simulation for a mean burst length of $\tau = 1$, including the confidence interval (CI) of 95%.

Table 3: Average *mCLR* results for $\tau = 1$.

CPS-PP Size (bits)	Average *mCLR*	
	Analytical	Simulation [95% CI]]
24	0.0985	0.108176 [0.108156, 0.108196]
96	0.0550	0.059307 [0.059284, 0.059331]
352	0.0322	0.032224 [0.032210, 0.032239]

(a)

(b)

(c)

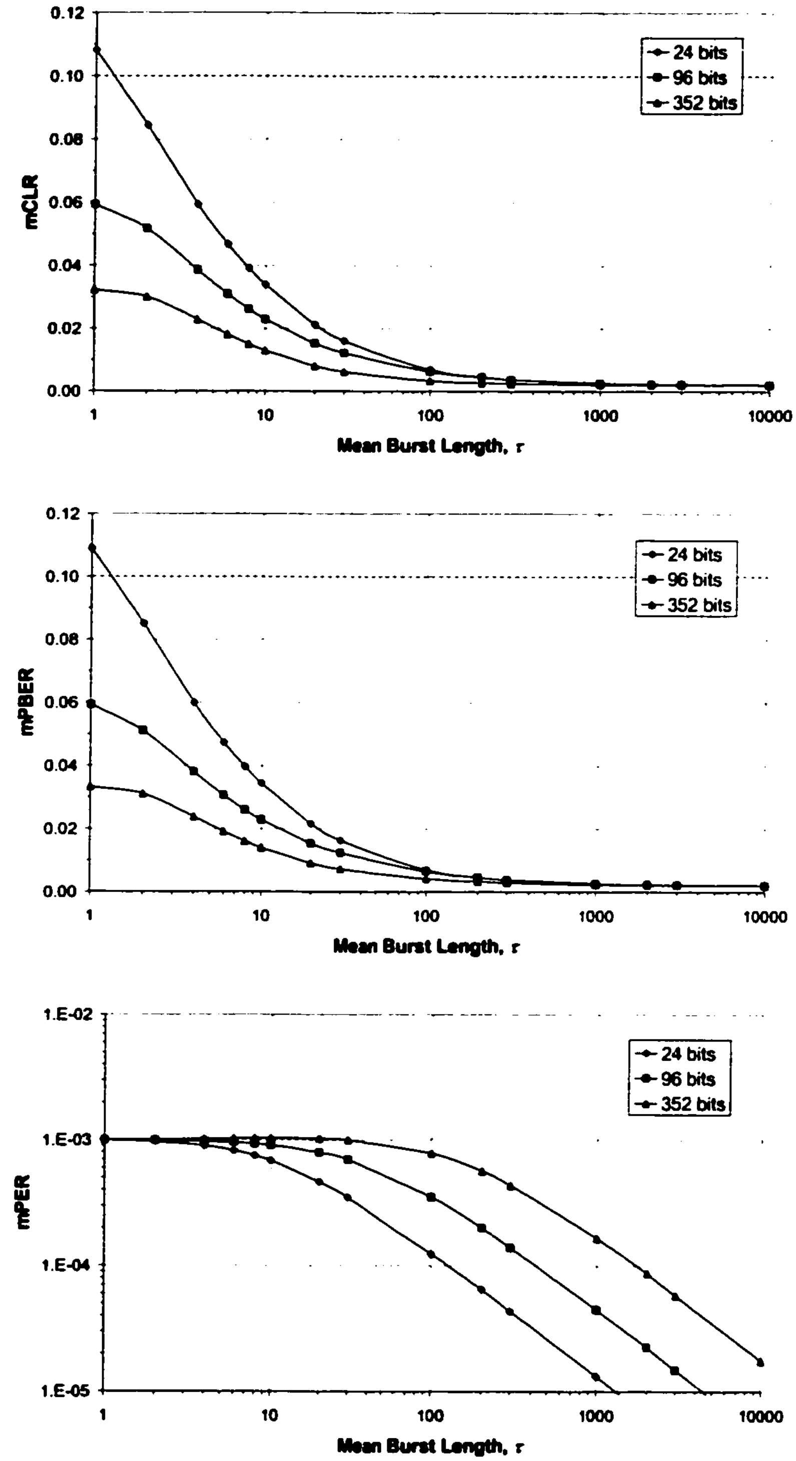

Figure 4.9: Average performance metrics.

From Table 3 it is observed that in general the average *mCLR* results are slightly higher for the numerical results obtained using the ns-2 simulation tool, except for the case where the CPS-PP size is equal to 352 bits. This can be explained by the fact that the results obtained under the ns-2 simulation account for the case where CPS packets are mapped beyond the boundaries of the CPS-PDU. In the case of CPS-PP size equal to 352 bits only one complete CPS packet is carried within a the payload of the CPS-PDU, therefore there are no CPS packets being mapped beyond the boundaries of the CPS-PDU and the numerical results are the same both in the analytical and in the simulation approaches. For the case where CPS packets are allowed to be mapped beyond the boundaries of a CPS-PDU, we have that CPS packets that are mapped between two ATM cells are exposed to a higher probability of losses. This is due to the fact that these CPS packets (i.e., AAL2 packets that are mapped in two CPS-PDUs) must rely on two error-free ATM header fields and two error-free STF fields before they can be successfully delivered to the higher layers. The same observation applies for the performance metric *mPBER*, shown in Figure 4.9(b). Table 4 lists the average *mPBER* results obtained using the analytical expression from Section 4.2, as well as, the numerical results obtained under the ns-2 simulation for a mean burst length of $\tau = 1$, including the confidence interval (CI) of 95%.

Table 4: Average *mPBER* results for $\tau = 1$.

CPS-PP Size (bits)	Average *mPBER*	
	Analytical	Simulation [95% CI]
24	0.0994	0.108917 [0.108897, 0.108937]
96	0.0560	0.059311 [0.059289, 0.059334]
352	0.0332	0.033192 [0.033178, 0.033206]

The numerical results for performance metric *mPER* in Figure 4.9(c) do not show a significant difference between the results obtained using the analytical derivation, presented in Figure 4.7(c).

4.5 Summary

In this chapter we have derived analytical expressions for performance metrics of interest at the AAL2 layer. These expressions allow the analysis of the impact of bit errors on the structure of the ATM and AAL2 frame structure.

The numerical results presented in this section demonstrate that the probability of errors experienced by the user of the AAL2 (i.e., higher layer applications) is greatly due to the impact of bit errors over the ATM and the AAL2 header fields, as demonstrated by the numerical results derived for performance metrics *mCLR* and *mPBER*. In particular the results presented for metric *mPBER* corroborate this observation, as the *mPBER* reflects the impact of bit errors over the CPS packets that are not discarded at the ATM or the AAL2 layers, as well as, the impact of discarded CPS packets. These results imply there is a need for an improved method for the protection of the ATM and the AAL2 header fields when they are exposed to an error-prone channel.

It has also been shown that the performance results depend on the relative position of the AAL2 CPS packet within the payload of the CPS-PDU. In this way, the first AAL2 packet that appears immediately after the STF field shows the best performance, as indicated by performance metric *mCLR*. In addition, it has been found that the use of large AAL2 CPS packets is preferable for the transport over wireless channels, as the probability of losses at the AAL2 layer is reduced for large CPS packets. However it must be observed that the use of large CPS packets may increase the packetization delays, as a large CPS-PP must be filled before transmitting the CPS-PDU. In addition, the use of large CPS packets increases the probability of errors in the payload of the AAL2 packets as illustrated by the performance results derived for performance metric *mPER*.

The analytical expressions derived in this chapter assumed that the AAL2 packets were not mapped beyond the boundaries of the CPS PDU (i.e., AAL2 packets are not carried by more than one ATM cell). This assumption simplified the derivation of closed form expressions for the analysis of performance metrics of interest at the AAL2 layer. However, the AAL2 standard does allow for AAL2 packets to be mapped beyond the boundaries of a single CPS PDU. Therefore a simulation using the ns-2 simulation tool was implemented and performance results were derived to verify the accuracy of the numerical results obtained using the analytical expressions (35), (38) and (39). The simulation results presented in this chapter demonstrate that the performance results under the analytical derivation provide a good approximation for the evaluation of the performance at the AAL2 layer. The numerical results obtained in the simulation show slightly worst performance (i.e., probability of losses was slightly higher) than the numerical results obtained under the analytical approach. This result is related to the fact that in the simulation the AAL2 packets are allowed to be mapped (transported) by more than one ATM cell, thus the probability of losses increases for these AAL2 packets as the successful delivery of these packets relies on the probability that both ATM cell headers are not corrupted by bit errors.

In Chapter 5 diverse mechanisms are proposed to improve the performance at the AAL2 layer and numerical results are presented to evaluate the performance improvements of such mechanisms.

Chapter 5 Improving Performance at the AAL2 Layer

5.1 Introduction

The numerical results presented in Chapter 4 were derived to evaluate the performance behaviour of the AAL2 standard over an error-prone channel. These results show that the probability of a lost AAL2 packet is related to the impact of the bit errors over the ATM and the AAL2 header fields. In particular the performance degradation observed by the users of the AAL2 is greatly related to the impact of bit errors in the AAL2 header fields, as these fields are required to provide the delineation of the AAL2 packets inside the payload of the ATM cell. Thus the importance to explore diverse mechanisms to protect and/or modify these header fields to improve the performance of the AAL2 standard over the error-prone links.

Digital communication systems make use of diverse techniques to improve the loss performance over error-prone channels. One of these techniques relies on the introduction of redundant data along with the information of interest; an example of this approach is the use of forward error control fields, which introduce parity bits for the detection and/or correction of bit errors. Other techniques try to take advantage of the statistical independence of the bit error process that might exist by transmitting or receiving multiple copies of the original signal; an example of this approach is the use of diversity techniques. In this chapter, we incorporate diverse mechanisms to improve the system performance of the AAL2 standard over an error-prone link and we evaluate the impact of these mechanisms on the performance observed at the AAL2 layer. The analysis of the performance metrics of interest at the AAL2 layer is based on the use of FSMC models to characterize the error process at the physical layer, as it has been described in Chapter 3 and Chapter 4.

This chapter is divided in three sections. Section 5.2 demonstrates the performance improvements at the AAL2 layer by introducing diverse implementations using Forward Error Correction codes. In Section 5.3 performance results are obtained for a system implementation using space diversity reception.

5.2 Impact of FEC on WATM/AAL2 over the Gilbert-Elliott channel

The transmission of digital data over an error-prone channel can benefit from the use of channel coding to protect the information from bit errors by selectively introducing redundancies in the transmitted data. Depending on the system requirements a channel coder can be used to provide diverse levels of protection. For example, a channel coder can be used to detect bit errors, while some other coders are even capable of correcting a limited number of bit errors. System implementations that are not delay sensitive may benefit from the use of error detection codes, which are relatively easy to implement and usually result in relatively small fields, thus allowing for the reduction of the coder overhead at the expense of the retransmission of corrupted messages. On the other hand, delay sensitive application may have to rely on an error correction coder to avoid the delays introduced by the retransmission of corrupted messages at the expense of increased overhead and more complex coding/decoding mechanisms.

A channel coder generates an encoded version of the digital message (or source data) for transmission over an error-prone channel. There are two basic types of error correction and detection codes: block codes and convolutional codes. Block codes are characterized by codewords with a fixed length. Each codeword is created by introducing a fixed number of parity bits (i.e., redundant information) to a fix number of source data bits. On the other hand, convolutional codes differ from block codes in that data bits are not grouped to create a block to be encoded. Instead a continuous sequence of information bits is mapped into a continuous sequence of encoded bits. In this work we demonstrate the performance that is achieved by introducing block codes to protect the frame structure of the ATM cell and that of the AAL2 packets. Several research studies have addressed the impact of introducing FEC mechanisms at the ATM layer [56] – [70]. In this section we are interested in evaluating the impact of FEC mechanisms at the AAL2 layer. The use of convolutional codes is not addressed in this work, as block codes are better suited for the protection of block structured data [61], such as that of ATM cells.

A block code can be used to detect and correct a limited number of bit errors, this in turn results in a reduction of the retransmissions of messages due to corrupted header fields. The use of block codes results in an effective way to increase the performance of a digital communication system, when other means of improvement may be impractical or difficult to implement (e.g., it might not be possible to increase the transmitter power). The use of block codes involves the introduction of parity bits to a block of information bits, thus creating a codeword or code block. In a block encoder, k information bits are encoded into n code bits. A total of $(n - k)$ redundant bits are added to the k information bits for the purpose of detecting and correcting errors. The block code is referred to as an (n, k) code, and the rate of the code is defined as $R_c = k/n$ and is equal to the rate of information divided by the raw channel rate.

An important characteristic of the block codes is the minimum distance, d_{min}. This parameter is associated to the error-detecting and/or error-correcting capability of the block code. The concept of minimum distance can be explained by defining the concept of Hamming distance. The Hamming distance $d(\mathbf{v},\mathbf{w})$ of two codewords $\mathbf{v}$ and $\mathbf{w}$ is defined to be equal to the number of places where the two codewords differ. For example, let $\mathbf{v} = (1\ 0\ 0\ 0\ 1\ 1\ 1\ 0)$ and $\mathbf{w} = (0\ 1\ 0\ 1\ 1\ 1\ 1\ 1)$, then $d(\mathbf{v},\mathbf{w})$ is equal to 4, as the codewords $\mathbf{v}$ and $\mathbf{w}$ differ on the first, second, forth and eighth elements. Then, the minimum distance of a block code $\mathbf{C}$, where $\mathbf{C}$ is equal to the set of all codewords, is defined as

$$d_{min} = \min\{d(\mathbf{v},\mathbf{w}) : \mathbf{v},\mathbf{w} \in \mathbf{C}, \mathbf{v} \neq \mathbf{w}\}. \tag{42}$$

Several schemes have been addressed for the implementation of Forward Error Correction (FEC) codes within an ATM cell. Some of these schemes apply a FEC code to the entire ATM cell (header and payload), while other schemes propose the protection of the ATM header independently of the ATM payload. The first method results in an inefficient use of the FEC code, as the header and the payload are given the same amount of protection. In the later method a stronger FEC code is applied to the ATM header and upon the application requirements a FEC code can be applied to the ATM payload. Furthermore, once a FEC code has been applied to the header, these bits can be interleaved with the payload bits to protect the header information from burst errors.

In this section, numerical results are presented to demonstrate the performance of the AAL2 standard by implementing block codes to protect the headers of the ATM and AAL2 frame structure. For the purpose of analysis, four scenarios are considered in this section:

1. The HEC field, from the standard ATM header, is replaced by a BCH code to protect the ATM header.

2. The HEC field, from the standard ATM header, is removed and a BCH code is used to protect the remaining 4 ATM header octets, plus the single octet STF field (only 7 bits are encoded from the STF field, as the bit used for parity is not required).

3. The HEC field, from the standard ATM header, is removed and a BCH code is used to protect the remaining 4 ATM header octets, plus the single octet STF field. In addition, the HEC field from the AAL2 CPS packet is replaced by a BCH code to protect the AAL2 CPS packet header.

4. The payload field of a sequence of ATM cells is protected using a Reed-Solomon code.

The performance results presented in Sections 5.2.1 through 5.2.3 rely on the use of BCH codes to protect the different header fields of the ATM and the AAL2 frame structure. These results were obtained by following the analytical derivation presented in Section 4.2. However it should be noted that each of the previous scenarios (i.e., the three scenarios using BCH codes) required the use of a modified representation of Expression (30), which is used to evaluate the probability function $Pr[\beta_m=0, k_m=\ell]$.

The protection of the ATM and the AAL2 header fields rely on the use of shortened BCH codes. Shorten BCH codes are used when the natural length n of an (n, k) BCH code is not suitable for the requirements of the application [72]. Given an (n, k) BCH code set $\mathbf{C}$, it is possible to create a linear subset $\mathbf{D}$ by considering that the l leading high-order information digits are equal to zero, as illustrated in Figure 5.1. The linear subset $\mathbf{D}$ is conformed by 2^{k-l} code vectors.

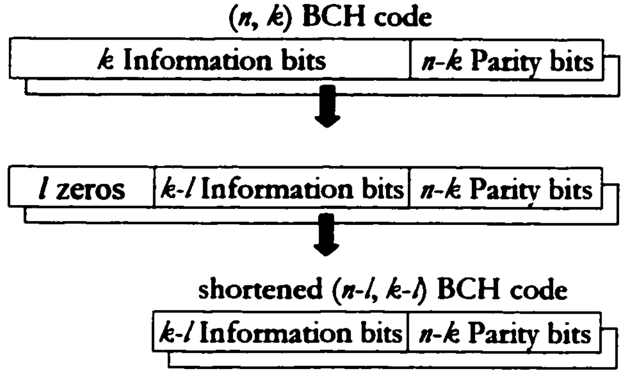

Figure 5.1: A shortened (*n-l*, *k-l*) BCH code.

It should be noted that a shortened (*n-l*, *k-l*) BCH code has at least the same error-correcting capability as the (*n*, *k*) BCH code from which it was derived [72].

5.2.1 BCH Encoded ATM Header

This scenario is used to evaluate the performance improvements at the AAL2 layer when a BCH code is used to replace the HEC field (which is capable of correcting single bit errors) from the ATM header. In this way, the remaining ATM header fields (i.e., 32 bits) are encoded using the shortened codes BCH(44,32), BCH(50,32), BCH(56,32) and BCH(59,32), which are capable of correcting up to t = 2, 3, 4 and 5 bits in error respectively.

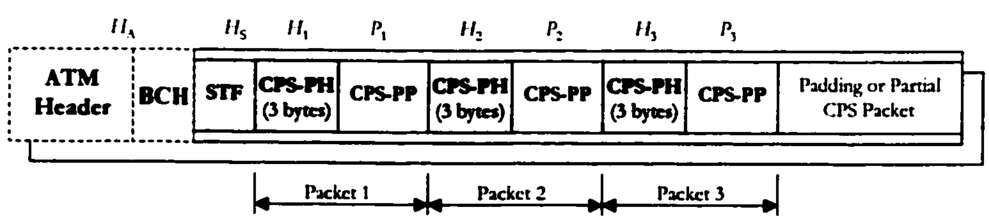

Figure 5.2: BCH encoded ATM header.

Table 5 shows the original BCH codes from where the shortened BCH codes are derived [72].

Table 5: Shortened BCH codes used to protect the ATM header.

(n, k) BCH Code	**Shortened (n-l, k-l) BCH Code**	**Length l (bits)**	**Error-correcting strength (t)**
BCH(63,51)	BCH(44,32)	19	2
BCH(63,45)	BCH(50,32)	13	3
BCH(63,39)	BCH(56,32)	7	4
BCH(63,36)	BCH(59,32)	4	5

The CPS-PDU structure shown in Figure 5.2 is considered for the derivation of numerical results and it is assumed that the CPS packets are not mapped beyond the boundaries of the CPS-PDU (i.e., $M' = 0$). The analysis assumes CPS packets of equal size and the CPS packet payload size is 96 bits. The error-prone channel is characterized by the Gilbert-Elliott model and the model parameters assume an BER of $\varepsilon = 10^{-3}$ with state error probabilities equal to $P_\varepsilon(0) = 0$ and $P_\varepsilon(1) = 0.5$.

It should be noted that the HEC field from the ATM header has been replaced by an (n, k) BCH code, which is capable of correcting up to t bits in error. For this scenario it is assumed that the m-th AAL2 packet is successfully delivered to the higher layers only when there are t or less bit errors in the ATM header, zero bit errors in the STF field and zero bit errors in all of the CPS-PHs beginning with the first CPS packet up to the m-th CPS packet. Then the numerical results presented in this scenario rely on a modified representation of the joint probability $Pr[\beta_m=0, k_m=\ell\,]$ defined in Expression (30). Then $Pr[\beta_m=0, k_m=\ell\,]$ is given by

$$Pr[\beta_m = 0, k_m = \ell] = \begin{cases} \sum_{i=0}^{\ell} \boldsymbol{\pi}\boldsymbol{\Phi}(i, N_A)\boldsymbol{\Phi}(0, N_S)\mathbf{P}^{M'}\boldsymbol{\Phi}(0, N_1)\boldsymbol{\Phi}(\ell, L_1)\mathbf{e} & m = 1 \\ \sum_{i=0}^{\ell} \boldsymbol{\pi}\boldsymbol{\Phi}(i, N_A)\boldsymbol{\Phi}(0, N_S)\mathbf{P}^{M'} \prod_{j=1}^{m-1} \boldsymbol{\Phi}(0, N_j)\mathbf{P}^{L_j}\boldsymbol{\Phi}(0, N_m)\boldsymbol{\Phi}(\ell, L_m)\mathbf{e} & 1 < m \leq M \end{cases}, \quad (43)$$

and the probability function $Pr[\beta_m = 1, k_m = \ell]$ remains the same as denoted in Expression (31).

Results presented in Figure 5.3 correspond to the performance of the CPS packet 1, as it is shown in Figure 5.2. For comparison purposes, the performance results obtained under the standard ATM/AAL2 frame structure are also presented in this figure. The performance results for the standard ATM/AAL2 frame structure are denoted under the HEC label.

From Figure 5.3(a) it is observed that improvements for performance metric *mCLR* are small and they are only noticeable for relatively small mean burst lengths, $\tau < 10$ bits, as the BCH encoded header is only capable of correcting some of the ATM header errors. This is a result of the limited error correcting capability of the BCH encoded header. On the other hand, for mean burst lengths greater than 10 bits, $\tau > 10$, the error correcting capability of the BCH codes is far exceeded, thus the loss performance at the AAL2 layer remains the same for all the different code rates.

Performance results for metric *mPBER* are presented in Figure 5.3(b). It should be noted that performance results obtained for this metric are similar to the results of metric *mCLR*, presented in Figure 5.3(a). This is explained in terms of the definition of *mPBER*, which is the probability of errors experienced by the layers above the AAL2 and it is given by Expression (39). From Expression (39) it is clear that the *mPBER* is a function of the *mCLR* and it is also a function of the probability of bit errors in the payload of non-discarded AAL2 packets. Therefore, the results presented in Figure 5.3(b) imply that the probability of bit errors observed by the layers above the AAL2 is greatly due to the impact of discarded AAL2 packets.

(a)

(b)

(c)

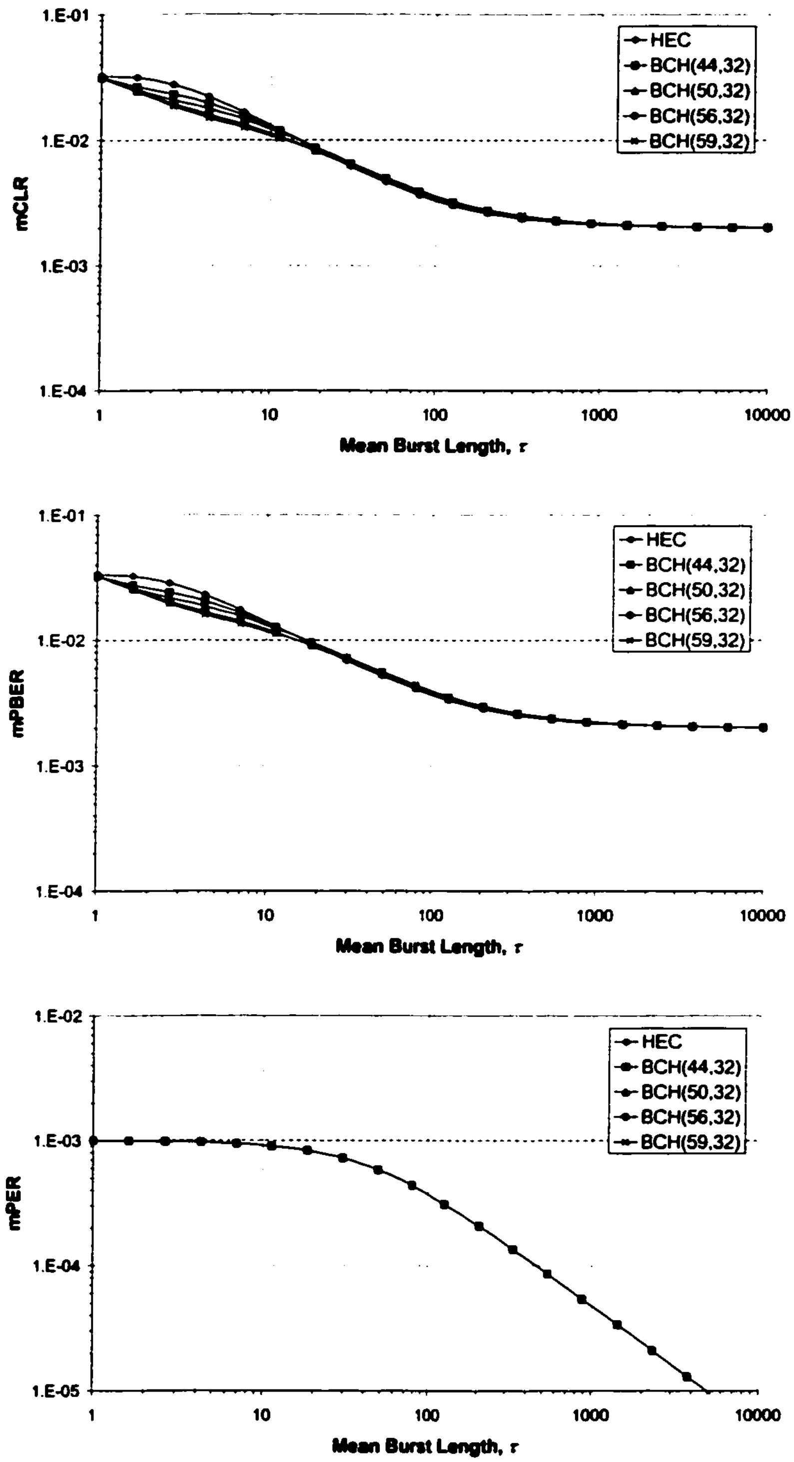

Figure 5.3: BCH Encoded ATM Header.

Figure 5.3(c) shows the results for performance metric *mPER*. From this figure it is observed that the performance remains the same for all the protection schemes. This result is expected, as the metric *mPER* reflects the average BER on the payload of non-discarded AAL2 packets. Consequently, the BER remains unaffected as none of the analysed scenarios provide any error correction capability for the payload of the AAL2 CPS packets.

5.2.2 BCH Encoded ATM/STF Header

This scenario is presented to evaluate the performance improvements at the AAL2 layer when a BCH code is used to protect both the ATM header and the STF field. The CPS-PDU structure shown in Figure 5.4 is considered for the derivation of numerical results.

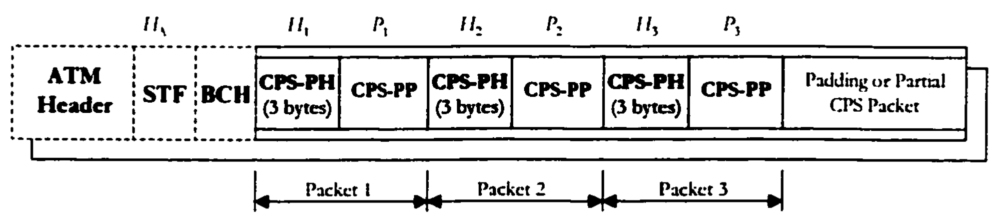

Figure 5.4: BCH encoded ATM/STF headers.

It should be noted that the HEC field and the parity bit have been removed from the ATM header and the STF field respectively, as the BCH code replaces the functionality provided by these fields. In this way, the ATM header and the STF field (the combined size of the ATM header plus the STF field is 39 bits) are encoded using the shortened codes BCH(51,39), BCH(57,39), BCH(63,39) and BCH(74,39), which are capable of correcting up to t = 2, 3, 4 and 5 bits in error respectively. Table 6 shows the original BCH codes from where the shortened BCH codes are derived [72]. The CPS packets are assumed to be of equal size and the CPS packet payload size is equal to 96 bits. In addition, the analysis assumes that the CPS packets are not mapped beyond the boundaries of the CPS-PDU, thus $M' = 0$. The error-prone channel is characterized by the Gilbert-Elliott model and the model parameters assume a channel BER of $\varepsilon = 10^{-3}$ with state error probabilities equal to $P_e(0) = 0$ and $P_e(1) = 0.5$.

Table 6: Shortened BCH codes used to protect the ATM/STF headers.

(*n*, *k*) BCH Code	Shortened (*n-l*, *k-l*) BCH Code	Length *l* (bits)	Error-correcting strength (*t*)
BCH(63,51)	BCH(51,39)	12	2
BCH(63,45)	BCH(57,39)	6	3
BCH(63,39)	BCH(63,39)	0	4
BCH(127,92)	BCH(74,39)	53	5

For this scenario it is assumed that the m-th CPS packet is successfully delivered to the higher layers only when there are t or less bit errors in the ATM/STF encoded header and zero bit errors in all of the CPS-PHs beginning with the first CPS packet up to the m-th CPS packet. Then the numerical results presented in this scenario rely on a modified representation of the joint probability $Pr[\beta_m=0, k_m=\ell]$ defined in Expression (30). Then $Pr[\beta_m=0, k_m=\ell]$ is given by

$$Pr[\beta_m = 0, k_m = \ell] = \begin{cases} \displaystyle\sum_{i=0}^{t} \boldsymbol{\pi}\boldsymbol{\Phi}(i, N_A)\mathbf{P}^{M'}\boldsymbol{\Phi}(0, N_1)\boldsymbol{\Phi}(\ell, L_1)\mathbf{e} & m = 1 \\ \displaystyle\sum_{i=0}^{t} \boldsymbol{\pi}\boldsymbol{\Phi}(i, N_A)\mathbf{P}^{M'}\prod_{j=1}^{m-1}\boldsymbol{\Phi}(0, N_j)\mathbf{P}^{L_j}\boldsymbol{\Phi}(0, N_m)\boldsymbol{\Phi}(\ell, L_m)\mathbf{e} & 1 < m \leq M \end{cases}, \tag{44}$$

where N_A is defined to be the size of the protected ATM/STF field. The probability function $Pr[\beta_m=1, k_m=\ell]$ remains the same as denoted in Expression (31).

(a)

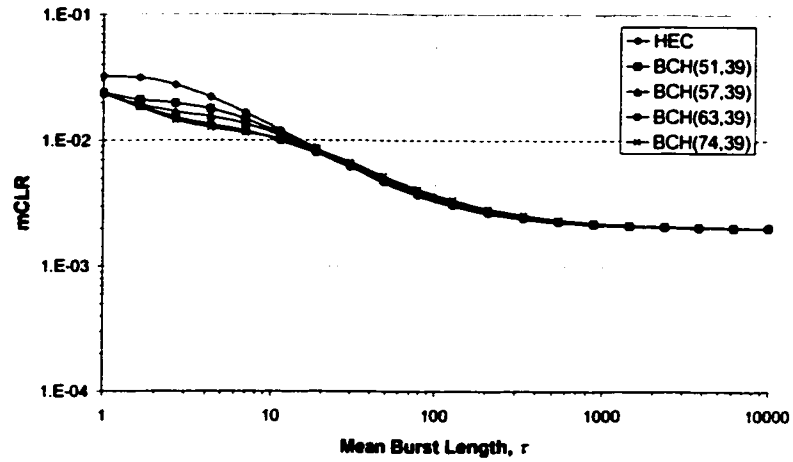

(b)

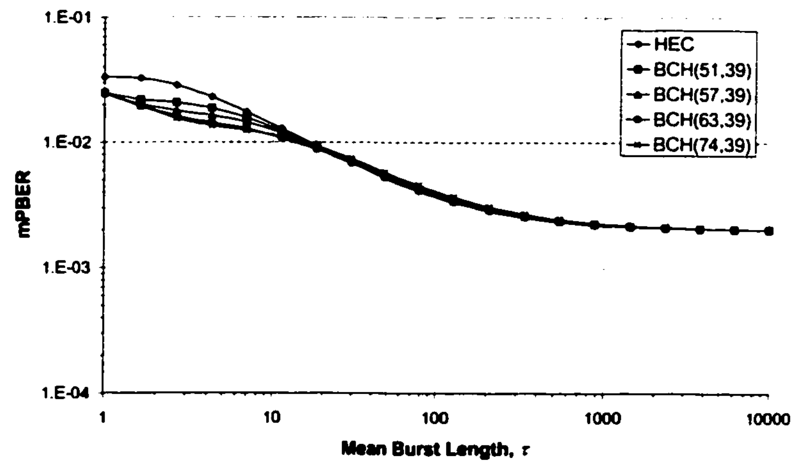

(c)

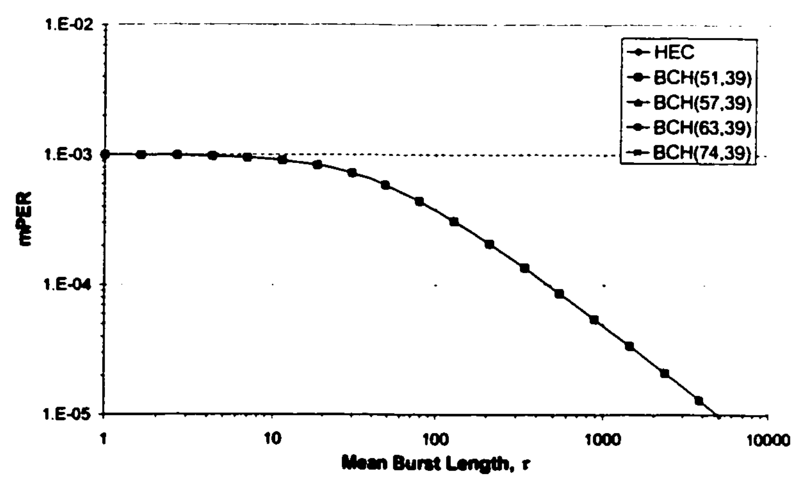

Figure 5.5: BCH Encoded ATM/STF Headers.

The numerical results presented in Figure 5.5 correspond to the evaluation of performance metrics for the first AAL2 packet (i.e., CPS packet 1). From the performance results shown in Figure 5.5, it is observed that performance improvements are small as compare to the results presented in section 5.2.1.

Figure 5.5(a) shows the results for the performance metric *mCLR*. From this figure it is clear that performance improvements are mainly noticeable for a small mean burst length in the order of $\tau \approx 1$. It is interesting to note that for a mean burst length of $\tau = 1$ all the results are basically the same regardless of the code rate used to protect the ATM header along with the STF field. This result implies that for $\tau = 1$ the probability of losing an AAL2 packet is greatly due to corrupted CPS-PH fields. In other words, the performance improvements that are gained by increasing the code rate of the BCH code are shadowed by the probability of those AAL2 packets being lost due to corrupted CPS-PH.

Figure 5.5(b) shows the results for the performance metric *mPBER*. Once again it is observed that this performance metric follows very closely the behaviour of the performance metric *mCLR*. The result implies that the impact of bit errors over the structure of the ATM and AAL2 frames is mainly due to corrupted ATM and AAL2 header fields. Figure 5.5(c) shows the results for performance metric *mPER*. Performance results for this performance metric are the same as those presented in Section 5.2.1.

5.2.3 BCH Encoded ATM/STF/AAL2 Headers

The numerical results presented in Sections 5.2.1 and 5.2.2 clearly indicate that performance improvements are marginal when at least one of the ATM or AAL2 header fields remains without any error correcting capability. This was particularly obvious for small mean burst lengths in the order of $\tau \approx 1$. The scenario presented in this section deals with the protection (i.e., a FEC code was introduce to provide for error correcting capabilities) of all the ATM and the AAL2 header fields. This scenario is presented to evaluate the performance improvements at the AAL2 layer when a BCH code is used to protect both the ATM header and the STF field. In addition, a second BCH code is used to replace the HEC field from the CPS-PH. The CPS-PDU structure shown in Figure 5.6 is considered for the derivation of numerical results. The analysis assumes that AAL2 packets are not mapped beyond the boundaries of a CPS-PDU and therefore $M' = 0$. The CPS packets are assumed to be of equal size and the CPS packet payload size is equal to 96 bits. The Gilbert-Elliott model is used to characterize the bit error process at the physical layer and the model parameters assume a channel BER of $\varepsilon = 10^{-3}$ with state error probabilities equal to $P_e(0) = 0$ and $P_e(1) = 0.5$.

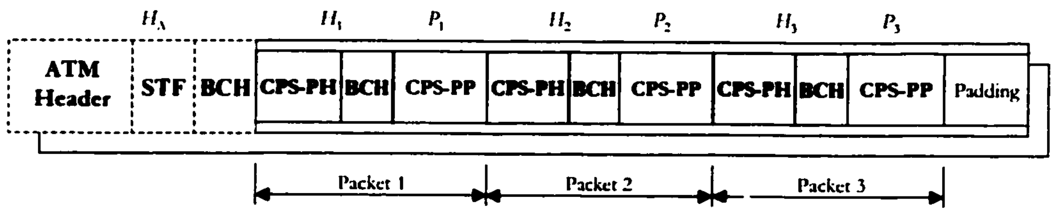

Figure 5.6: BCH encoded ATM/STF/AAL2 headers.

The derivation of the numerical results presented in this section, relies on the generic CPS-PDU structure shown in Figure 5.6. In this scenario the HEC field is removed from the ATM header and the parity bit is removed from the STF field. Then the remainder of the ATM header is encoded along with the remainder of the STF filed using an (n_1, k_1) BCH code, which is capable of correcting up to t_1 bit errors. In addition, the HEC field from each CPS packet is replaced by an (n_2, k_2) BCH code, which is capable of correcting up to t_2 bit errors. For this scenario it is assumed that the m-th CPS packet is successfully delivered to the higher layers only when there are t_1 or less bit errors in the ATM/STF encoded header and t_2 or less bit errors in each of the CPS-PHs beginning with the first CPS packet up to the m-th CPS packet. Then Expression (30) becomes

$$Pr[\beta_m = 0, k_m = \ell] = \begin{cases} \displaystyle\sum_{i_0=0}^{t_1}\sum_{i_1=0}^{t_2} \boldsymbol{\pi}\boldsymbol{\Phi}(i_0, N_A)\mathbf{P}^{M'}\boldsymbol{\Phi}(i_1, N_1)\boldsymbol{\Phi}(\ell, L_1)\mathbf{e} & m = 1 \\ \displaystyle\sum_{i_0=0}^{t_1}\sum_{i_1=0}^{t_2}\cdots\sum_{i_m=0}^{t_2} \boldsymbol{\pi}\boldsymbol{\Phi}(i_0, N_A)\mathbf{P}^{M'}\prod_{j=1}^{m-1}\boldsymbol{\Phi}(i_j, N_j)\mathbf{P}^{L_j}\boldsymbol{\Phi}(i_m, N_m)\boldsymbol{\Phi}(\ell, L_m)\mathbf{e} & 1 < m \le M \end{cases} \quad (45)$$

and the probability function $Pr[\beta_m = 1, k_m = \ell\,]$ remains the same as denoted in Expression (31).

The scenario presented in this section is divided in two groups. Both groups are evaluated using the same code rates for the BCH code that is used to protect the ATM header and the STF field. The main difference is with respect to the code rate that is used to protect the header of the AAL2 packets.

- AAL2 CPS packet header protected with shortened BCH(24,19)

This scenario evaluates the performance improvements at the AAL2 layer when a BCH code is used to protect both the ATM header and the STF field. In this way, the ATM header and the STF field (the combined size of the ATM header plus the STF field is 39 bits) are encoded using the shortened codes BCH(51,39), BCH(57,39), BCH(63,39) and BCH(74,39), which are capable of correcting up to t = 2, 3, 4 and 5 bits in error respectively. In addition, the HEC field from the AAL2 CPS packet header is replaced by a shortened BCH(24,19) code with error correcting capability of t = 1 bit. Table 7 shows the original BCH codes from where the shortened BCH codes are derived [72].

Table 7: Shortened BCH codes used to protect the ATM/STF/AAL2 headers.

(n, k) BCH Code	Shortened (n-l, k-l) BCH Code	Length l (bits)	Error-correcting strength (t)
BCH(31,26)	BCH(24,19)	7	1
BCH(63,51)	BCH(51,39)	12	2
BCH(63,45)	BCH(57,39)	6	3
BCH(63,39)	BCH(63,39)	0	4
BCH(127,92)	BCH(74,39)	53	5

Figure 5.7(a), shows the performance results for metric *mCLR*. From these results it is observed that the performance is improved for mean burst lengths smaller than 2 bits (i.e., $\tau \leq 2$), as compared to the results presented in sections 5.2.1 and 5.2.2. In particular, for $\tau = 1$ metric *mCLR* is approximately 2.5×10^{-4}, whereas in the previous two scenarios the performance metric *mCLR* was approximately 2.5×10^{-2}. That is an improvement of two orders of magnitude, which is achieved by adding the error-correcting capability to the header of the CPS packets.

Similarly, the performance results for metric *mPBER* also present an improvement for small mean burst lengths in the order of $\tau \leq 2$. An interesting observation is that metric *mPBER*, shown in Figure 5.7(b), no longer follows metric *mCLR* for a mean burst lengths smaller than 2 bits, $\tau \leq 2$. This observation is explained by the fact that the probability of a lost AAL2 packet, due to corrupted ATM/AAL2 headers, is smaller than the probability of errors on the payload of non-discarded AAL2 packets. Then for $\tau \leq 2$, the contributing factor over the performance metric *mPBER* is the probability of bit errors in the payload of non-discarded AAL2 CPS packets, as the information bits carried in the AAL2 CPS-PP are not protected against bit errors.

Figure 5.7(c) shows the performance results for metric *mPER*. The numerical values for this metric remain unaffected, as compared to the results presented in sections 5.2.1 and 5.2.2. This result is explained by the fact that none of these scenarios provide any protection for the payload of the AAL2 packets and therefore the probability of bit errors remains the same for all the analysed scenarios.

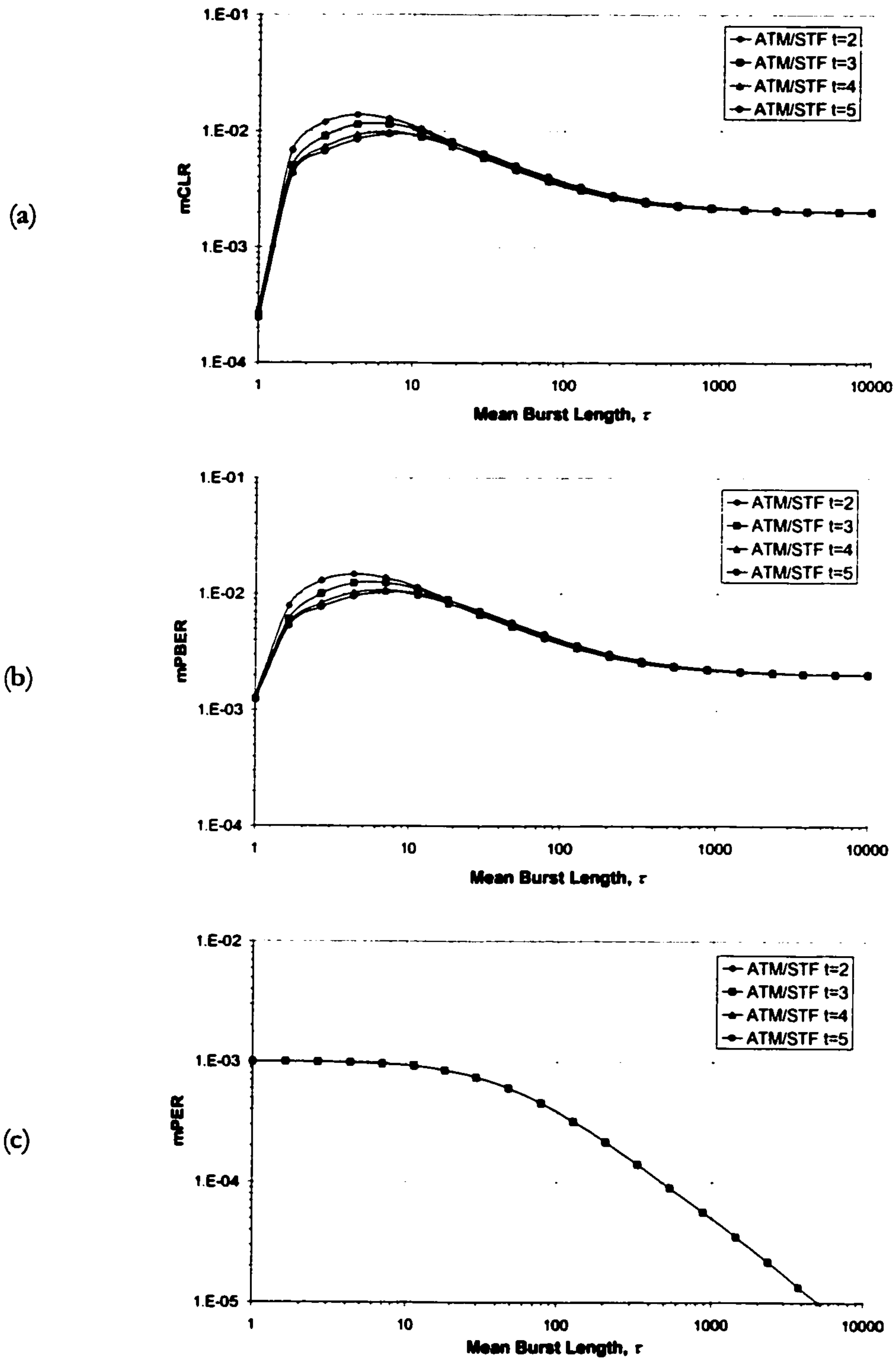

Figure 5.7: BCH Encoded ATM/STF/AAL2 Headers.

- AAL2 CPS packet header protected with shortened BCH(29,19)

This scenario evaluates the performance improvements at the AAL2 layer when a BCH code is used to protect both the ATM header and the STF field. In this way, the ATM header and the STF field (the combined size of the ATM header plus the STF field is 39 bits) are encoded using the shortened codes BCH(51,39), BCH(57,39), BCH(63,39) and BCH(74,39), which are capable of correcting up to t = 2, 3, 4 and 5 bits in error respectively. In addition, the HEC field from the AAL2 CPS packet header is replaced by a shortened BCH(29,19) code with correcting capability t = 2 bits. Table 8 shows the original BCH codes from where these shortened BCH codes are derived [72].

Table 8: Shortened BCH codes used to protect the ATM/STF/AAL2 headers.

(n, k) BCH Code	Shortened (n-l, k-l) BCH Code	Length l (bits)	Error-correcting strength (t)
BCH(31,21)	BCH(29,19)	2	2
BCH(63,51)	BCH(51,39)	12	2
BCH(63,45)	BCH(57,39)	6	3
BCH(63,39)	BCH(63,39)	0	4
BCH(127,92)	BCH(74,39)	53	5

(a)

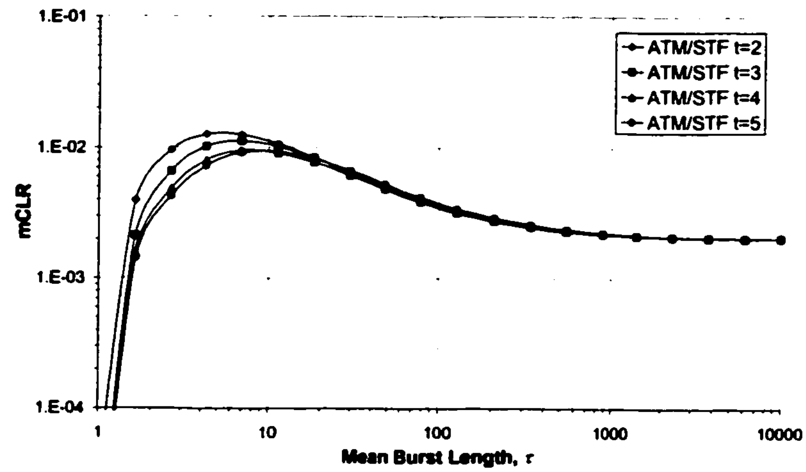

(b)

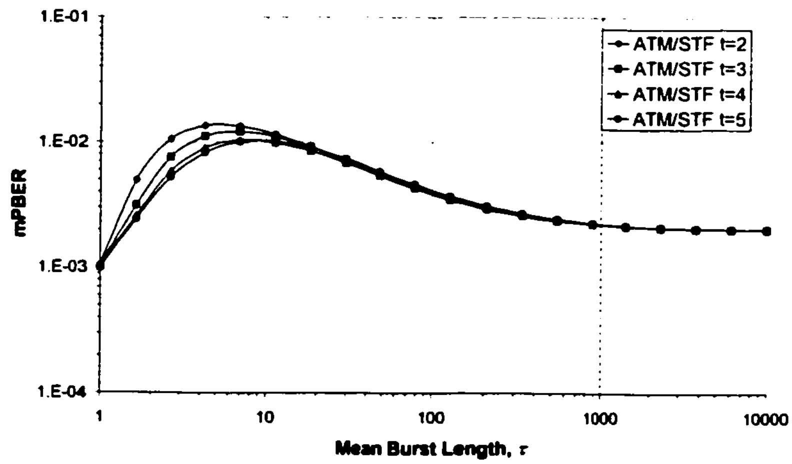

(c)

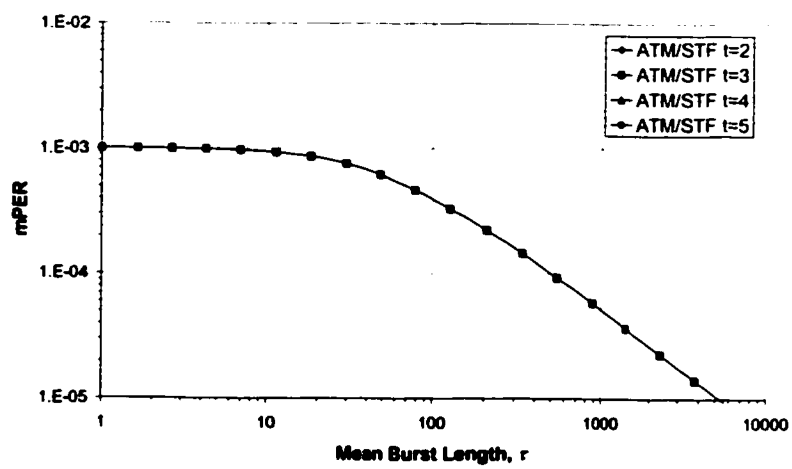

Figure 5.8: BCH Encoded ATM/STF/AAL2 Headers.

From the results presented in Figure 5.8 we can derive similar conclusions, as those presented for the previous scenario (AAL2 packet with BCH encoded header with correcting capability of $t = 1$ bit). The main difference, are the results presented for metric *mCLR*. In particular for a mean burst length of $\tau = 1$ bit, where *mCLR* is reduced to approximately 3.5×10^{-5}. However, the probability of errors experienced by the layer above the AAL2 does not benefit by the improvement over *mCLR* (for $\tau = 1$) as the probability of errors in the payload of non-discarded AAL2 packets remains the main factor contributing to the performance of *mPBER*.

5.2.4 Reed-Solomon Encoded CPS-PDU

The previous section addressed the use of BCH codes to protect the ATM and AAL2 header fields. From the numerical results presented in Sections 5.2.1, 5.2.2 and 5.2.3 it is clear that the use of BCH encoded ATM and AAL2 headers results in limited improvements with respect to the performance results of the AAL2 standard, presented in Section 4.3.

In this section we evaluate the use of Reed-Solomon (RS) codes to protect the frame structure of the AAL2 packets. The Reed-Solomon codes correspond to a special class of non-binary BCH codes. The block length of a (n, k) Reed-Solomon codeword is given by

$$n = 2^m - 1, \tag{46}$$

where m is equal to the size (in bits) of a codeword symbol. The minimum distance of a Reed-Solomon code is given by

$$d_{min} = n - k + 1, \tag{47}$$

where k is equal to the number of information symbols that are used to form a codeword of length n. The rate R_c of a Reed-Solomon coder is defined as

$$R_c = k/n \, . \tag{48}$$

The analysis presented in this section assumes a Reed-Solomon system which is capable of correcting symbol erasures. A Reed-Solomon decoder using symbol erasures can increase the error correcting capability of the code [71]. That is, a Reed-Solomon coding system which corrects symbol erasures can correct up to t symbol errors and e symbol erasures provided that

$$2t + e \leq d - 1 \, , \tag{49}$$

where the distance $d \leq d_{min}$.

From Expression (49) it is clear that the error correcting capability of a Reed-Solomon code is upper-bounded by the minimum distance d_{min} of the RS code. Another observation from Expression (49) is that for a given code distance d, the error correcting capability of the Reed-Solomon code decreases by a factor of two for symbols in error t. On the other hand, the error correcting capability of the Reed-Solomon code decreases by a factor of one for symbol erasures e. This observation agrees with the previous statement which implies that symbol erasures can increase the error correcting capability of the RS code. Table 9 shows the length n of a Reed-Solomon codeword for different values of the symbol size m.

Table 9: Reed-Solomon Codeword information.

Symbol Size m (Bits)	Codeword Length n (Number of Symbols)	Codeword Length n (Bits)
8	255	2040
9	511	4599
10	1023	10230
11	2047	22517

The derivation of the numerical results following the analytical approach presented in Section 4.2 results impractical and complex for a system that implements a Reed-Solomon coder when used to encode a block of several ATM cells. This observation is explained by the fact that performance metrics derived in Expressions (35), (38) and (39) rely on the evaluation of the joint probability distribution $Pr[\beta_m, k_m]$ and it is here where the problem lies. The set of rules that are required to evaluate the probability that an AAL2 packet is successfully delivered to the higher layers (i.e., the probability that the random variable β_m is equal to zero) become a function of all the possible combinations that result in a successfully decoded RS codeword. That is, random variable β_m will be equal to zero for all the possible combinations of symbols in error t and symbol erasures e that result in a successfully decoded RS codeword. Because of this limitation the numerical results in this section are derived by running simulations using the ns-2 tool.

The simulation assumes two ATM nodes exchanging information over a FSMC modeled link. Figure 5.9 shows the block diagram of the network architecture implemented in the ns-2 simulation. The functionality of the RS encoder and decoder is implemented as part of the ATM/AAL2 Agents at the transmitter and receiver nodes, as illustrated in Figure 5.9.

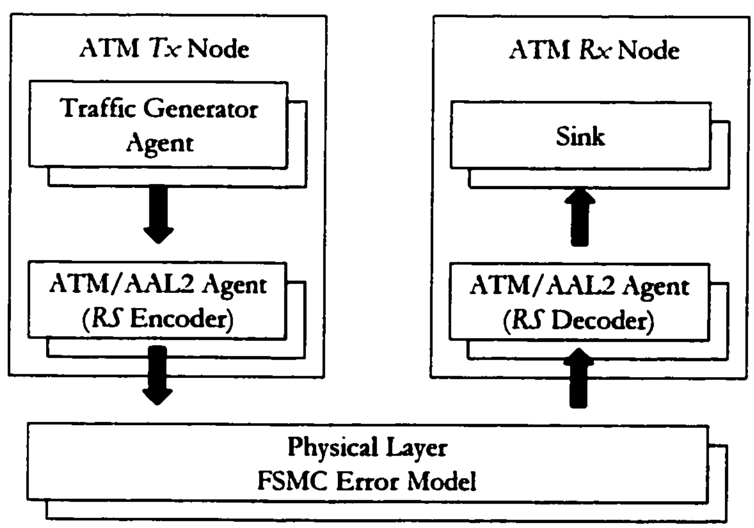

Figure 5.9: Block diagram of the ns-2 network architecture using RS encoder/decoder.

The numerical results evaluate the performance at the AAL2 layer when an (n, k) Reed-Solomon code is used to protect the payload of a sequence of n_{ATM} ATM cells. Thus the number of information bits d_{ATM} that are protected is equal to $d_{\text{ATM}} = n_{\text{ATM}} \times 384$ (recall that the payload of an ATM cell is composed of 48 bytes or 384 bits). The relation between the number of payload information bits d_{ATM} and the number of information symbols k is given by

$$k = \left\lceil \frac{d_{\text{ATM}}}{m} \right\rceil, \tag{50}$$

where m is equal to the RS symbol size and $\lceil . \rceil$ is defined as the ceiling function. In other words, a sequence of d_{ATM} information bits will result in k information symbols.

The number of ATM cells n_{RS} that are required to transport a Reed-Solomon codeword of length n is given by

$$n_{\text{RS}} = \left\lceil {}^{n}\!/_{n_s} \right\rceil, \tag{51}$$

where n_s is defined as the number of RS symbols in each ATM cell payload. It should be noted that the analysis assumes that RS symbols are not mapped between the ATM cells, as illustrated in Figure 5.10, so the number of RS symbols in each ATM cell is given by.

$$n_s = \left\lfloor {}^{384}\!/_{m} \right\rfloor, \tag{52}$$

where $\lfloor . \rfloor$ is defined as the floor function and m is defined as the RS symbols size.

The analysis presented in this section assumes a Reed-Solomon symbol size of $m = 10$ bits, therefore the RS codeword length is equal to $n = 1{,}023$ symbols. Following Expression (51), each Reed-Solomon codeword will require a sequence of $n_{\text{RS}} = 27$ ATM cells. From Expression (52) the number of RS symbols in each ATM cell is equal to $n_s = 38$. It should be noted that as a result of the symbol alignment there are n_p bits required for padding at the end of each ATM cell. For the particular case of $m = 10$ then number of padding bits in each ATM cell is $n_p = 4$.

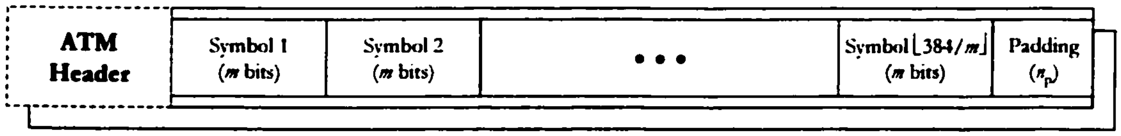

Figure 5.10: Reed-Solomon symbol alignment in the ATM cell.

The performance results at the AAL2 layer are evaluated by encoding a block of ATM cells with an RS coder for different code rates. Table 10 lists the different code rates that are used to derive the analytical results presented in this section.

Table 10: Reed-Solomon code rates.

ATM Cells (n_{ATM})	Information bits (d_{ATM})	Information Symbols (k)	Codeword Length (n)	Approx. code rate (R_c)
13	4,992	500	1023	0.5
16	6,144	615	1023	0.6
19	7,296	730	1023	0.7
21	8,064	807	1023	0.8
24	9,216	922	1023	0.9

For an approximated code rate of 0.5, the minimum distance of the code is $d_{min} = 524$, as dictated by Expression (47). Then the RS decoder is capable of correcting up to a maximum of $t = \lfloor 523/2 \rfloor = 261$ symbols in error (i.e., assuming there are no symbol erasures) or it can correct up to a maximum of e = 523 symbol erasures (i.e., assuming there are no symbol errors), as dictated by Expression (49). In the same way it is possible to calculate the theoretical error correcting capability for all the RS code rates listed in Table 10. The error correcting capabilities are listed in Table 11.

Table 11: Error correcting capability of the RS decoder.

Codeword Length (n)	Information Symbols (k)	Symbols in Error (t)	Symbol Erasures (e)
1023	500	261	523
1023	615	204	408
1023	730	146	293
1023	807	108	216
1023	922	50	101

Figure 5.11 shows the performance results at the ATM and AAL2 layers for different code rates. The simulations assumed AAL2 packets of equal size and the AAL2 packets were allowed to be mapped beyond the boundaries of the CPS-PDU. The performance results presented in Figure 5.11 correspond to AAL2 packets with payload of size 24 bits. However, it should be noted that performance results derived for different AAL2 packet payload size resulted in plots similar to those presented in Figure 5.11. That is the numerical results were insensitive to variations in the AAL2 payload size. The Gilbert-Elliott model is used to characterize the bit error process at the physical layer and the model parameters assume a channel BER of $\varepsilon = 10^{-3}$ with state error probabilities equal to $P_e(0) = 0$ and $P_e(1) = 0.5$.

The performance results for code rates 0.5, 0.6, 0.7, 0.8 and 0.9 correspond to the probability that an AAL2 packet will be lost/discarded due to corrupted ATM or AAL2 header fields. In other word these performance results correspond to the metric $mCLR$. The performance results denoted by the label "ATM" correspond to the probability that an ATM cell will be discarded at the ATM layer due to a corrupted ATM header. It should be noted that the ATM headers are not protected by any FEC codes and the only error correcting capability is that provided by the standard HEC field, which is capable of correcting up to 1 bit in error.

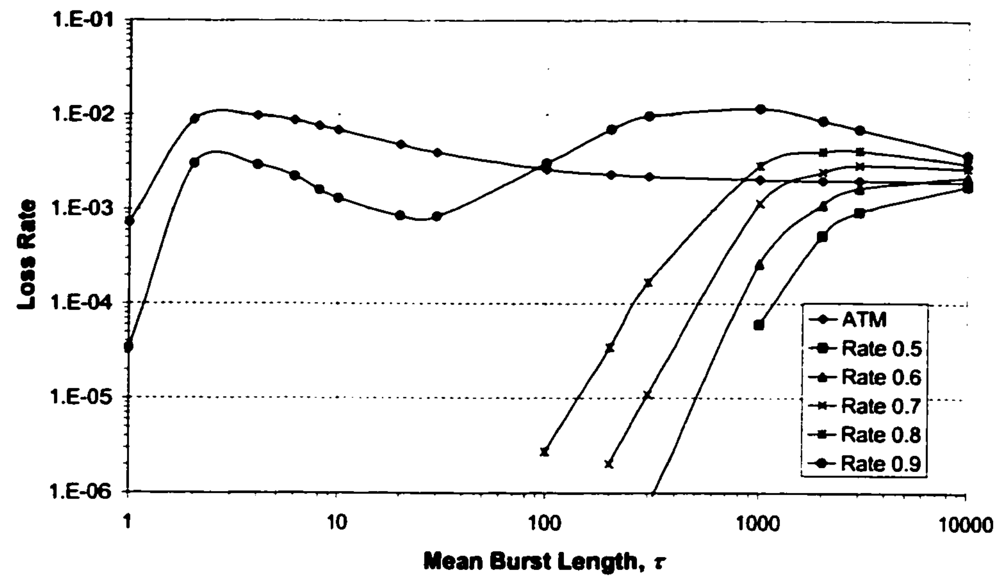

Figure 5.11: Reed-Solomon Encoded CPS-PDU.

From Figure 5.11 it is observed that the performance improves as the code rate decreases. This observation is explained by the fact that the smaller code rates result in an increase of the error correcting capability of the RS code, as indicated in Table 11. However this increase in performance comes with a price in terms of overhead.

An interesting observation from Figure 5.11 is that performance plots follow a similar pattern (or behaviour) for code rates 0.5, 0.6, 0.7 and 0.8. That is, as the mean burst length τ increases, the *mCLR* increases and then converges as $\tau \rightarrow \infty$. However the performance curve for code rate 0.9 behaves differently. A careful observation of this curve reveals that the performance behaviour for code rate 0.9 is similar to the behaviour of the ATM cells loss rate for values of the mean burst length that are smaller or equal to 20 bits, i.e. $\tau \leq 20$. On the other hand, the performance behaviour for code rate 0.9 begins to follow the performance behaviour of the other curves for values of the mean burst length that are greater than 20 bits, $\tau > 20$. This performance behaviour can be explained as follows: the error correcting capability of the RS code is a function of two distinct processes. Namely the process related to the symbol erasures and the process related to the symbols in errors, as indicated in Expression (49). In the analysis, each RS codeword is carried by a sequence of 27 ATM cells and each ATM cell carries 38 symbols. Then a sequence of 38 symbols is lost (i.e., the RS codeword symbols are erased) every time an ATM cell is discarded and therefore RS codewords are vulnerable to ATM cell losses.

For a code rate of 0.9 the maximum number of symbol erasures is 101, assuming there are no symbols in errors. Then a RS codeword will be successfully decoded if at most 2 out of 27 ATM cells are discarded due to errors in the ATM header. Recall that each ATM cell carries 38 symbols, therefore two ATM cells lost will result in 76 symbols erasures and the RS decoder will still be able to successfully decode the RS codeword.

For a mean burst length of $\tau = 20$ bits the average number of bits in errors is equal to 10 bits (recall that the probability of bit errors in the "bad" state is equal to 0.5). On the other hand the channel BER is $\varepsilon = 10^{-3}$, then in steady-state the error-free state will have an average duration of 9990 bits (recall that the Gilbert-Elliott model assumes a time unit equal to the duration of one bit). So the case $\tau = 20$ represents the boundary situation where there exists a relatively high probability that at least 2 out of 27 ATM cells will be discarded due to bit error in the ATM header. This last statement results from the fact that in steady-state the channel model will make a transition to the bad state every 10,000 bits (i.e., assuming the mean burst length is $\tau = 20$) and a block of 27 ATM cells is composed by a sequence to 11,448 bits. For values of $\tau < 20$ the probability of corrupted ATM headers increases and the performance behaviour for code rate 0.9 becomes more a function of the ATM cell loss process as it is observed by the behaviour illustrated in Figure 5.11.

Now for code rate 0.9 and values of the mean burst length in the order of $\tau > 20$, the probability that two ATM headers are corrupted by bit errors decreases as the duration of the error-free event increases. Therefore the performance metric *mCLR* is less related to the ATM cell loss process, as illustrated in Figure 5.11.

The numerical results for performance metric *mPER* (not shown) are meaningless, as the probability of bit errors in the payload of the AAL2 packets, given that the AAL2 packet is not discarded, is always equal to zero. This statement is explained by observing that the AAL2 packets are encoded into RS codewords and the RS codewords are carried by a sequence of ATM cells. Therefore there are only two possible outcomes:

1 – The codeword is successfully decoded (i.e., because there are no symbol errors or erasures within the RS codeword, or the number of symbol errors and erasures is less or equal than the error correcting capability of the RS code) and all the AAL2 packets are successfully delivered to the higher layers without any errors. And therefore the performance metric *mPER* is equal to zero, as there are no errors in the payload of the AAL2 packets.

2 – The codeword is discarded (i.e., the number of symbol errors and erasures is greater than the error correcting capability of the RS code) and all the AAL2 packets are lost at the ATM layer.

Similarly, it is easy to observe that performance metric *mPBER* is similar to *mCLR* (i.e., for the scenario presented in this section), as the bit error process observed by the layers above the AAL2 is only a function of lost/discarded AAL2 packets.

5.2.5 Summary

The analysis presented in section 4.3 clearly indicated that the performance degradation at the AAL2 layer was greatly due to the impact of bit errors over the ATM and the AAL2 header fields. Consequently we proposed the use of diverse FEC mechanisms, such as block codes, to protect the ATM and the AAL2 header fields. In addition we present numerical results to evaluate the impact of introducing block codes, such as BCH and Reed-Solomon codes, to protect the ATM and the AAL2 header fields.

The first approach involved the use of BCH codes to protect the ATM and the AAL2 header fields. The numerical results presented in sections 5.2.1, 5.2.2 and 5.2.3 indicate that the use of BCH codes for the protection of the ATM and the AAL2 header fields results in a marginal improvement for performance metrics *mCLR* and *mPBER*. This last statement is especially true when at least one of the header fields is not protected by a block code, as demonstrated by the numerical results presented in sections 5.2.1 and 5.2.2, where the CPS-PH field was not protected by a BCH code. The numerical results presented in section 5.2.3 evaluate the scenario in which all the header fields are protected by a BCH code. For this particular scenario it was possible to observe significant performance improvements in terms of the probability of losing AAL2 packets at the AAL2 layer, as illustrated by the performance metric *mCLR*. However, the gains observed for performance metric *mCLR* are only significant for small burst lengths in the order of 1 or 2 bits. In general the introduction of the BCH codes for the protection of the ATM and AAL2 header fields do not provide good performance improvements as illustrated by the numerical results presented in sections 5.2.1, 5.2.2 and 5.2.3. Nevertheless, it is important to present the analysis of the ATM Adaptation Layer 2 when BCH codes are used to protect the ATM and AAL2 header fields, as it is not possible to arrive to such conclusions without a proper analysis as the one presented in these sections.

The second approach involved the use of Reed-Solomon codes to protect the payload of a sequence of ATM cells. The numerical results illustrate that the performance improvements at the AAL2 layer are significant for code rates that are equal or lower than 0.8. Furthermore, the performance results (e.g., the probability of a lost AAL2 packet) are improved for a mean burst length of up to a couple hundred bits. However, it should be pointed out that the introduction of Reed-Solomon codes greatly increases the overhead required by the resulting RS codewords (due to the additional parity bits). For example, for a RS coder with a code rate equal to 0.8 the number of ATM cell that are protected is 21 while the resulting RS codeword requires 27 ATM cells (see Table 10); this represents an overhead of approximately 20%.

In conclusion, the use of BCH codes may be of benefit for telecommunication systems in which the error-prone link is characterize by small burst of errors in the order of 1 or 2 bits. On the other hand for telecommunication systems in which the error-prone link is characterized by a mean burst length in the order of a couple of hundred bits then the implementation of RS codes becomes a better choice, at the expense of the additional overhead.

5.3 AAL2 Performance Analysis over Correlated Fading Channels with Diversity

In previous sections we evaluated the performance improvements at the AAL2 layer by introducing Forward Error Correction codes, such as block codes like BCH and Reed-Solomon codes. The numerical results demonstrated that the performance improvements at the AAL2 layer were good, as long as, the error correcting capability of the code was not exceeded. Therefore a different approach is required to improve the system performance for large values of the mean burst length.

In this section we are interested in evaluating the impact of the bit errors on the performance of the AAL2 standard by introducing the use of diversity. A diversity receiver can improve the system performance by processing multiple copies of the transmitted signal over independent (or uncorrelated) transmission paths.

We begin the analysis by defining a suitable model for the characterization of an error-prone link. The Gilbert-Elliott model has been extensively used in previous sections to characterize the bit error process of the wireless channel. The Gilbert-Elliott model relies on the statistical characterization of the birth and death process of the burst-error and error-free events. It is clear that the introduction of diversity will have an impact on the statistical behaviour of the burst-error and error-free events and therefore the derivation of the channel model parameters must account for the introduction of diversity at the physical layer. However it is not a simple matter to derive the Gilbert-Elliott model parameters (e.g., the transition probability matrix $\mathbf{P}$ and the steady state vector $\boldsymbol{\pi}$) once diversity is introduce into the system. An alternate approach is to characterize the statistical behaviour of the fading dynamics of the channel. This approach can easily introduce the impact of diversity and there are several publications that address the derivation of analytical expressions for the statistical characterization of channels using diversity [73]-[81]. In this way it is possible to implement a FSMC model to characterize the bit error process at the physical layer, which can be derived in terms of the statistical time varying dynamics of the fading channel.

The analytical derivation presented in this section follows the implementation of a Finite State Markov Chain (FSMC) model using the Nakagami-*m* distribution for the characterization of the statistical time varying fading dynamics of the channel, as described in Section 3.3. The Nakagami-m distribution was chosen for the analysis as it can be used to characterize a diverse number of statistical time varying fading channels, such as, Rayleigh or Ricean fading channels. Furthermore, the analytical results are presented to account for the introduction of space diversity reception, which is a very well know technique used to improve system performance in telecommunication systems.

The FSMC model is uniquely defined by its transition probability matrix $\mathbf{P}$, the steady state vector $\boldsymbol{\pi}$ and the state error probability vector $\mathbf{P_e}$. The transition probability matrix, $\mathbf{P}$, is defined as a $N \times N$ matrix with elements p_{ij}, $i,j \in \{1,2, \ldots, N\}$, where p_{ij} is defined as the probability of a transition from state i into state j, and is given by Expression (14), which can be expressed in terms of the fading amplitude α of the signal by

$$p_{ij} = \frac{Pr\left[\alpha_{i-1} \leq \alpha_1 < \alpha_i, \alpha_{j-1} \leq \alpha_2 < \alpha_j\right]}{Pr\left[\alpha_{i-1} \leq \alpha_1 < \alpha_i\right]} = \frac{\int_{\alpha_{j-1}}^{\alpha_j} \int_{\alpha_{i-1}}^{\alpha_i} p_{A_1,A_2}(\alpha_1, \alpha_2) d\alpha_1 d\alpha_2}{\int_{\alpha_{i-1}}^{\alpha_i} p_{A_1}(\alpha_1) d\alpha_1}, \tag{53}$$

where $p_{A_1,A_2}(\alpha_1, \alpha_2)$ is the joint probability density function (jpdf) of A_1 and A_2, $p_{A_1}(\alpha_1)$ is the probability density function (pdf) of A_1, and A_1, A_2 are two random variables defining the amplitude of the signal at the fading instants of interest. The probability density function and the joint density function of a Nakagami-m distributed random variable are presented in [29, 44] and are given by

$$p_A(\alpha) = \frac{2\alpha^{2m-1}}{\Gamma(m)} \left(\frac{m}{\Omega}\right)^m \exp\left[-\frac{m\alpha^2}{\Omega}\right], \tag{54}$$

$$p_{A_1,A_2}(\alpha_1, \alpha_2) = \frac{4(\alpha_1\alpha_2)^m \exp\left[-\frac{m}{\Omega}\frac{\alpha_1^2 + \alpha_2^2}{1-\rho}\right]}{\Gamma(m)(1-\rho)(\sqrt{\rho})^{m-1}} \left(\frac{m}{\Omega}\right)^{m+1} I_{m-1}\left(\frac{2m\alpha_1\alpha_2\sqrt{\rho}}{\Omega(1-\rho)}\right), \tag{55}$$

where $\Omega = \overline{\alpha^2}$ is the mean-square value of the fading amplitude α, m represents the Nakagami-m fading parameter, $\Gamma(\cdot)$ represents the Euler gamma function, $I_m(\cdot)$ represents the m-th order modified Bessel function of the first kind and ρ is the correlation coefficient between α_1 and α_2.

The steady state vector $\boldsymbol{\pi}$ is defined as a row vector with elements π_k, $k = 1, 2, \ldots, N$, and is given by

$$\pi_k = \int_{\alpha_{k-1}}^{\alpha_k} p_A(\alpha)d\alpha . \tag{56}$$

A closed form expression of (56) can be derived by substituting Expression (54) into (56). Then Expression (56) becomes

$$\pi_k = \frac{\Gamma(m,0,m \times \alpha_k{}^2/\Omega) - \Gamma(m,0,m \times \alpha_{k-1}{}^2/\Omega)}{\Gamma(m)}, \tag{57}$$

where $\Gamma(a, z_0, z_1) = \Gamma(a, z_0) - \Gamma(a, z_0)$ is the generalized incomplete gamma function and $\Gamma(a, z)$ is given by

$$\Gamma(a,z) = \int_z^{\infty} t^{a-1} \exp[-t]dt . \tag{58}$$

Expression (57) is the close-form representation of the denominator in Expression (53). However the numerator of Expression (53), after being substituted by equation (55), does not have a simpler form and therefore needs to be evaluated numerically [29].

The state error probability vector $\mathbf{P_e}$, as described in Section 3.3, is a row vector with elements $P_e(k)$, $k = 1, 2, \ldots, N$, where $P_e(k)$ is defined as the error probability associated to each state s_k, as defined by Expression (16), and is closely related to the modulation scheme.

From Expression (55) it can be observed that the joint probability density between two fading amplitudes of interest relies, among several other factors, on the correlation coefficient ρ. The correlation coefficient ρ between two fading instants can be represented in terms of the spatial correlation, $\rho(\Delta x)$, of the signal over the fading channel [82]. The analysis for the derivation of the spatial correlation characteristics, presented in [82], follows the coordinate system shown in Figure 5.12.

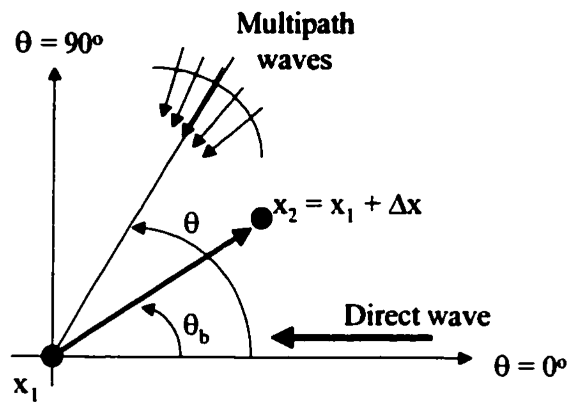

Figure 5.12: Coordinate system for spatial correlation analysis.

The analysis presented in this section follows the case in which the scattered waves arrive with a uniform angular distribution, as described in [82], shown in Figure 5.13.

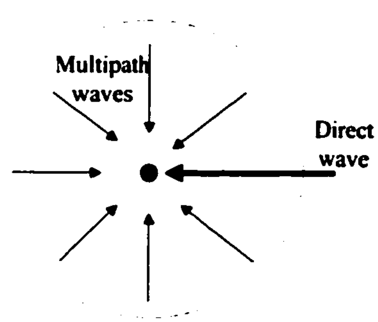

Figure 5.13: Scattered waves with a uniform angular profile.

In this case, the spatial correlation coefficient $\rho(\Delta x)$ is given by Expression [82, Eq. (22)] as

$$\rho(\Delta x) = \frac{2\{J_0(k\Delta x)\cos(k\Delta x\cos\theta_b)\} + s^2\{J_0(k\Delta x)^2\}}{2+s^2}, \tag{59}$$

where $J_0(\cdot)$ is the zero-order Bessel function of the first kind, k is the wave number defined by $k = 2\pi f_c / c$, were f_c represents the carrier frequency and s^2 is the average scattered wave power normalized by the direct-wave power, which is related to the *Ricean* parameter K by $s^2 = K^{-1}$.

For the purpose of the analysis presented in this section, it is useful to represent the spatial correlation coefficient $\rho(\Delta x)$ as a function of the channel symbol duration τ_b and the Doppler frequency f_d. It can easily be shown that $k\Delta x = 2\pi f_d \tau_b$, thus equation (59) becomes

$$\rho = \frac{2\{J_0(2\pi f_d \tau_b)\cos(2\pi f_d \tau_b \cos\theta_b)\} + s^2\{J_0(2\pi f_d \tau_b)^2\}}{2+s^2}. \tag{60}$$

It should be noted that large values of argument $2\pi f_d \tau_b$ correspond to a fast fading channel. On the other hand, small values of argument $2\pi f_d \tau_b$ correspond to a slow fading channel.

The system performance can be improved by implementing diversity techniques. In this section, the performance of ATM/AAL2 over correlated fading channels is evaluated in the presence of Equal-Gain Combining (EGC), where L uncorrelated copies of the received signal are directly combined (summed) to produce a single output. Under EGC diversity, if each of the L diversity branches is described by a Nakagami-m distributed random variable, with parameters m_0 and Ω_0, then the combined output approximately follows a new Nakagami-m distribution [44] with parameters

$$m \cong Lm_0, \tag{61}$$

$$\Omega = L\Omega_0 + L(L-1)\Omega_0 \frac{\Gamma^2(m_0 + 1/2)}{m_0\Gamma^2(m_0)}, \tag{62}$$

and the fading correlation parameter ρ, assuming the existence of i.i.d. (independent and identical distributed) diversity branch signals, of the diversity-combined output is equal to the correlation coefficient before equal gain combining [29], which is given by equation (60).

Section 5.3.1 presents the performance results at the AAL2 layer over a correlated fading channel using diversity. The channel model follows the analytical derivation presented in this section. In Appendix B, Section B.2 presents the derivation of the FSMC model parameters that were used to obtain the numerical results in Section 5.3.1.

5.3.1 Numerical Results

The numerical results presented in this section illustrate the performance of the AAL2 standard over a correlated fading channel in the presence of Equal Gain Combining (EGC) diversity reception. The CPS-PDU structure shown in Figure 5.14 is considered for the derivation of numerical results. The analysis assumes that AAL2 packets are not mapped beyond the boundaries of a CPS-PDU (i.e., $M' = 0$) and the CPS packets are assumed to be of equal size. The FSMC model is composed of a 6 state Markov chain and the channel BER is $\varepsilon = 10^{-3}$.

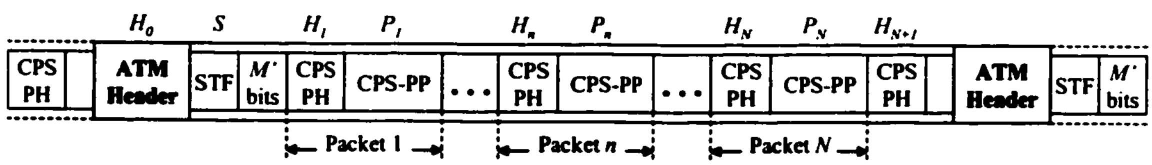

Figure 5.14: CPS PDU structure.

Performance results, presented in Figure 5.15, show the case in which diversity is not used and assume a CPS-PDU composed of seven AAL2 packets, each with CPS PDU payload of size equal to 24 bits (3 bytes). Figure 5.15(a) shows the results for the performance metric *mCLR*, for the CPS packets 1 through 7, as a function of the argument $2\pi f_d \tau_b$, which is related to the behaviour of the fading process.

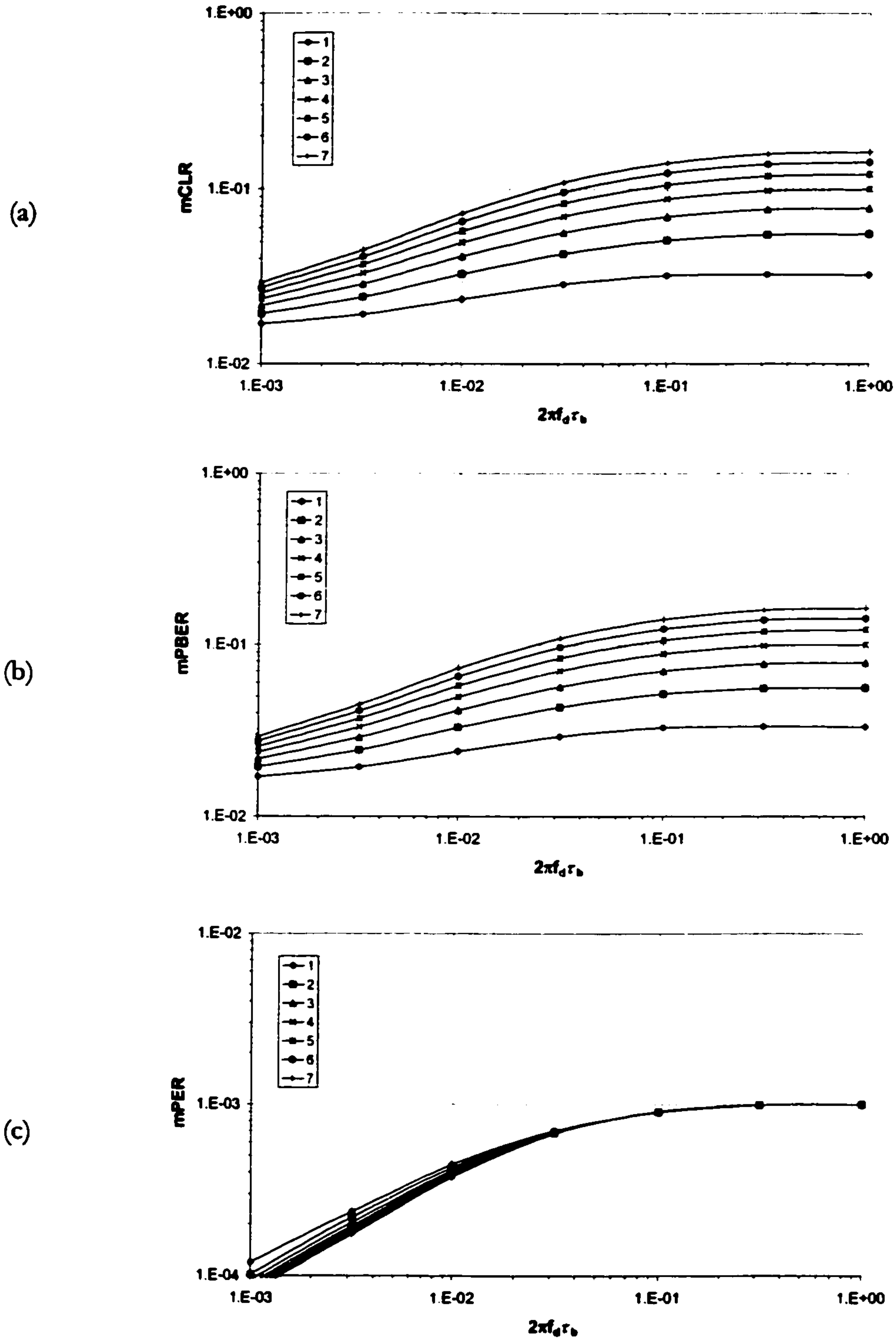

Figure 5.15 Numerical results for CPS packets 1 through 7 (without diversity).

From Figure 5.15(a) it is clear that the *mCLR* performance is best for CPS packet 1 and degrades with each subsequent CPS packet in the CPS-PDU payload. This behaviour is explained in view of the fact that the successful delivery of the CPS packet to the higher layers requires that the header of the CPS packet be correct, and in addition, that all headers from previous CPS packets in the CPS-PDU payload be correct. Figure 5.15(b) shows performance results for metric *mPBER*. It should be noted that performance results obtained for this metric are very similar to the results obtained for *mCLR*. From this observation it is clear that the main factor contributing to the BER seen by the higher layer is the *mCLR*, more specifically, the payload errors due to discarded CPS packets. Recall that, by definition of *mPBER*, bits lost at the ATM/AAL2 are considered bit errors at the higher protocol layers.

Results for performance metric *mPER* are shown in Figure 5.15(c). From this figure it is observed that performance *mPER* degrades, as argument $2\pi f_d \tau_b$ increases (fast fading), until it converges to a value of $mPER = 10^{-3}$. Whereas for low values of argument $2\pi f_d \tau_b$ (slow fading), performance metric *mPER* improves for each CPS packet. This result is explained by the fact that under slow fading if the channel falls in a deep fade then the receiver will experience a long burst of errors, as the model BER is fixed this implies that long burst error periods are followed by equally long error-free periods thus reducing the probability of lost/discarded AAL2 packets. On the other hand, under fast fading the channel tends to behave like a random channel as the receiver experiences short but frequent bursts of errors, therefore the probability of corrupted ATM and AAL2 headers increases. It is important to recall that a CPS packet can be mapped across CPS-PDU payload boundaries; in this case, the CPS packet is split into two parts, which are conveyed by two separate ATM cells. Performance metrics for this scenario are not addressed in this study, but the results are expected to be worse than those in the case where a CPS packet is conveyed in a single ATM cell, as the successful delivery of the CPS packet requires the correctness of two rather than one ATM cell headers.

Figure 5.16 show the performance results for the case with EGC diversity using two diversity branches (i.e. two antennas).

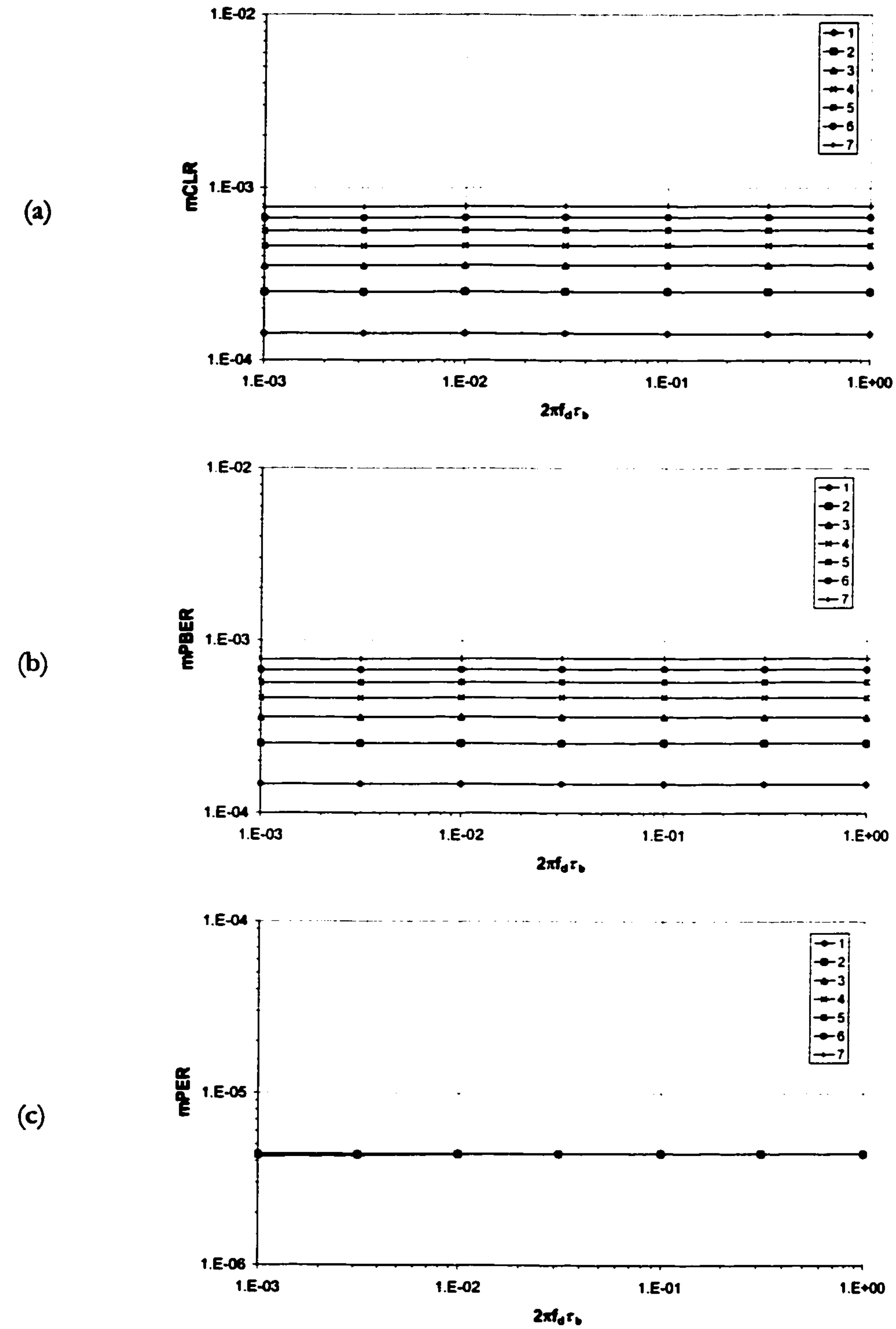

Figure 5.16: Numerical results for CPS packets 1 through 7 (using 2 branch diversity).

The numerical results show that the probability of errors, experienced by the ATM/AAL2 layers, has dropped to approximately 4.5×10^{-6}, which is more than two orders of magnitude compare to the case where diversity is not used. From Figure 5.16(a) it is observed that the probability of a lost AAL2 packet has dropped below 10^{-3}, whereas for the case with no diversity *mCLR* is greater than 10^{-2}.

Since AAL2 can accommodate CPS packets of variable payload size, it is of interest to study the performance of the AAL2 standard over the wireless channel for CPS packets with different payload sizes. For this purpose, numerical results for CPS packets with payload size equal to 24, 96 and 352 bits are presented in Figure 5.17. The results shown in these figures represent the average values over all CPS packets that are carried in the CPS-PDU payload for the case with no diversity.

From Figure 5.17(a) it is observed that the performance with respect to metric *mCLR* improves for large CPS packets. For large CPS packet payloads, the number of CPS packets that are carried in the CPS-PDU decreases and so does the number of CPS packet headers, thus the probability of corrupted headers affecting the CPS packet delineation decreases. In Figure 5.17(c), contrary to the behaviour exhibited by *mCLR*, the performance with respect to *mPER* improves for CPS packets with small payload size. By definition, *mPER* is associated with the rate of errors in the CPS packet payload given that the header/control fields are correct; therefore it mainly depends on the impact of the error process over the CPS packet payload. Consequently, the probability of errors in the CPS packet payload increases with the size of the payload field.

The performance results presented in Figure 5.18 analyze the same performance metrics presented in Figure 5.17 for the case in which EGC diversity with two diversity branches is implemented. In Figure 5.18(a) performance results for metric *mCLR* show that the probability of a lost CPS packet is below 10^{-3} regardless of the CPS packet payload size. Furthermore, it is observed that *mCLR* performance remains constant as argument $2\pi f_d \tau_b$ varies, thus the introduction of EGC diversity results in a mechanism resilient to fading variations. Figure 5.18(c) shows performance results for metric *mPER*, in this case it is observed that the probability of errors over the payload of a CPS packet remains the same regardless of the size of the CPS packet payload.

(a)

(b)

(c)

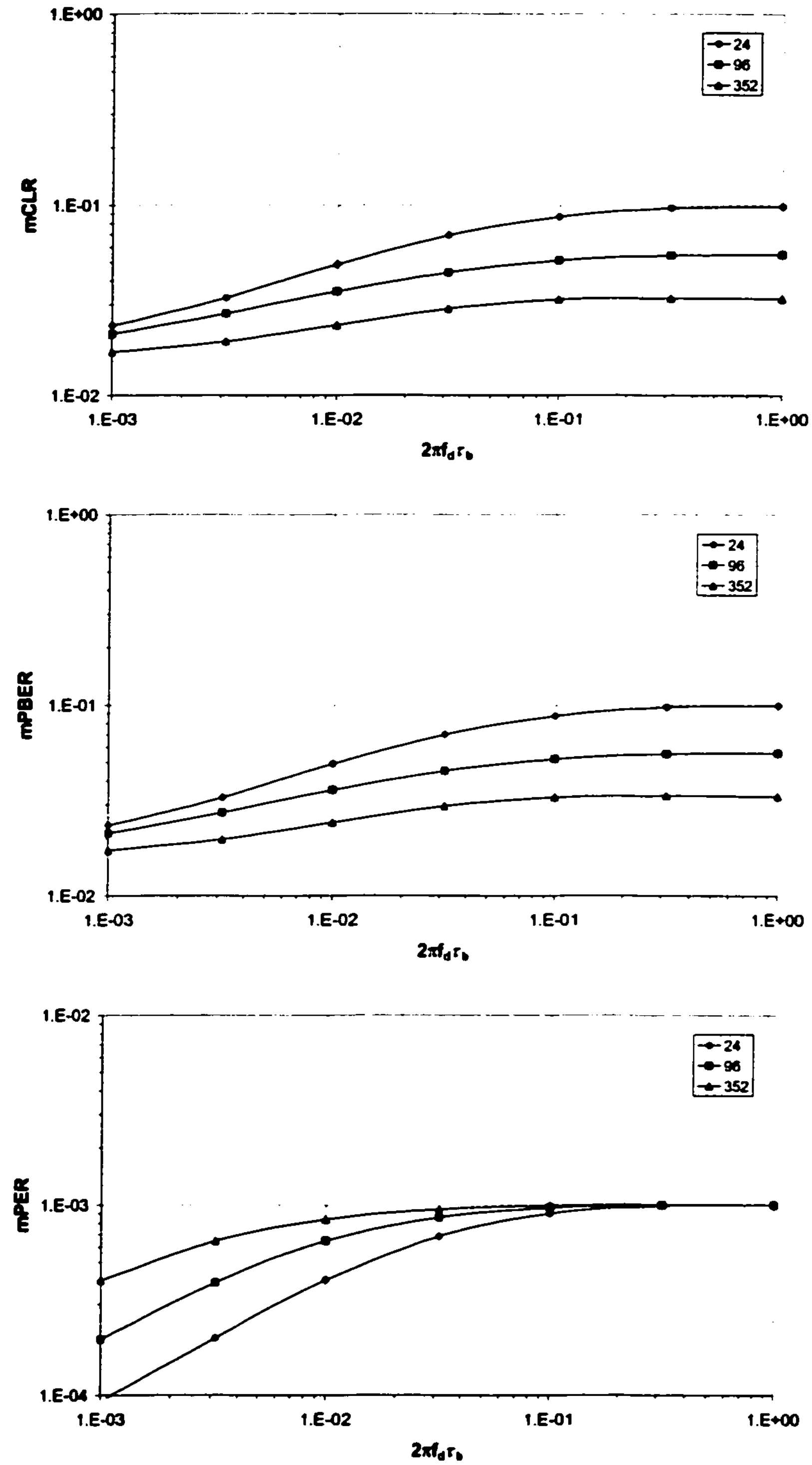

Figure 5.17: Performance results for different CPS-PP size (without diversity).

(a)

(b)

(c)

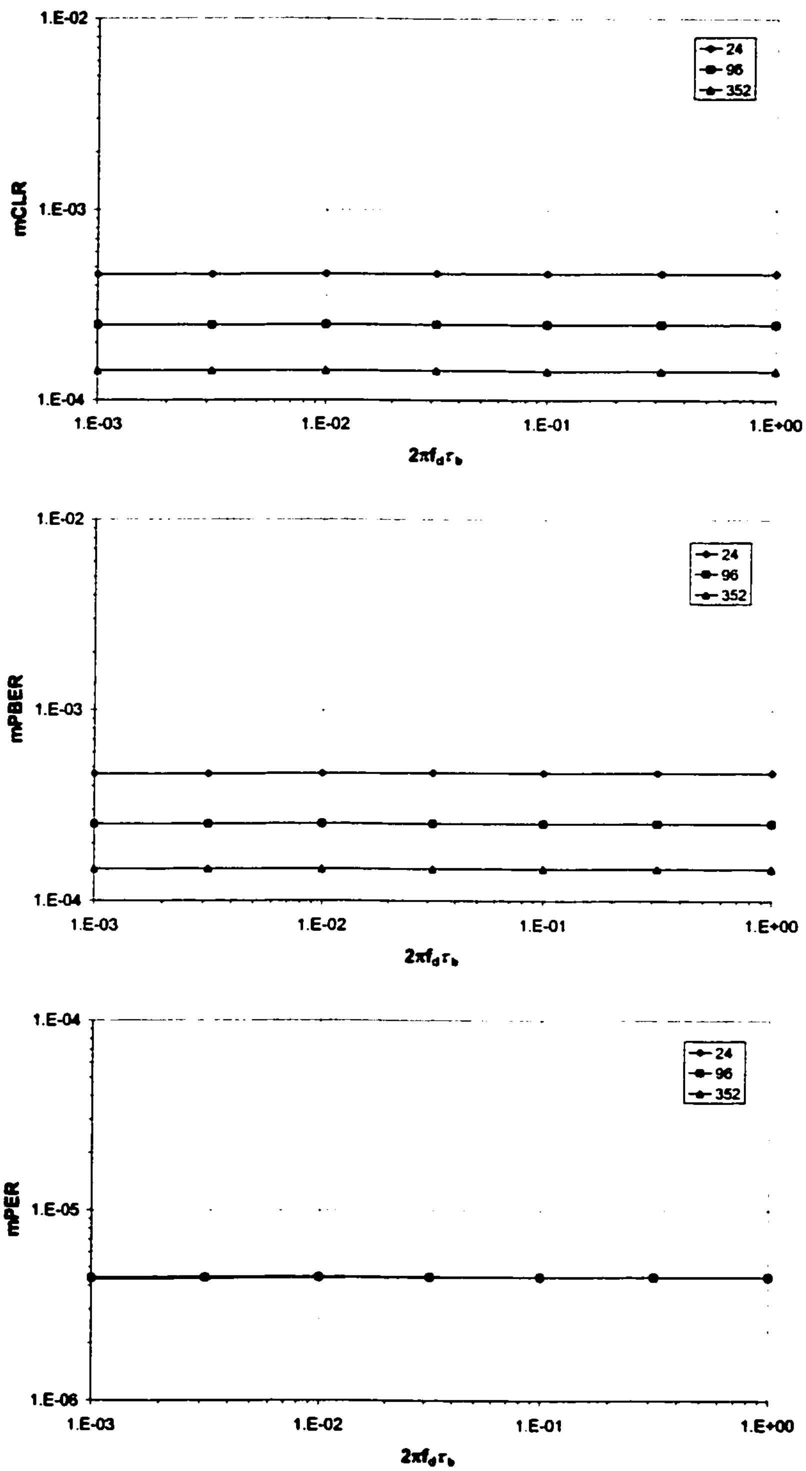

Figure 5.18: Performance results for different CPS-PP size (using 2 branch diversity).

5.3.2 Summary

In this section we evaluated the performance improvements at the AAL2 layer by introducing diversity reception to improve the system performance at the physical layer. The numerical results presented in this section assumed the use of Equal Gain Combining (EGC) which is considered to be a space diversity mechanism. Other space diversity techniques include Selection diversity and Maximal Ratio Combining (MRC) diversity. From the previous diversity techniques Selection diversity is the simplest diversity technique; however the performance improvements are not comparable to those that can be achieved under EGC or MRC. It is well known that MRC provides the best performance improvements [74], however Equal Gain Combining is less complex and easier to implement and it can provide performance improvements which are close to those of MRC.

The performance analysis of a system using Equal Gain Combining required the derivation of a FSMC to characterize the statistical time varying dynamics of the fading signal and at the same time incorporate the effects of the diversity reception. In the previous sections we relied on the Gilbert-Elliott model, however this model is not suitable for the analysis of a system with diversity.

The numerical results have shown that the implementation of a two branch Equal Gain Combining diversity receiver greatly improves the performance of the AAL2 standard over correlated fading channels. The introduction of EGC diversity has the effect of reducing the probability of bit errors experienced at the ATM and the AAL2 layers, consequently the probability of lost AAL2 packets or the probability of bit errors in the payload of the AAL2 packets is reduced.

Another observation is that the introduction of diversity results in a system which is resilient to fading variations. That is, the numerical results indicate that the probability of losses at the AAL2 layer remains unaffected to variations of the fading argument $2\pi f_d \tau_b$, which is related to the characteristics of the fading channel. For example, small values of the argument $2\pi f_d \tau_b$ correspond to a slow fading channel, were as large values of the argument $2\pi f_d \tau_b$ correspond to a fast fading channel.

Another interesting observation is that the numerical results derived for performance metrics *mCLR*, *mPBER* and *mPER* resemble the results derived under the Gilbert-Elliott channel model. That is, the results derived for large values of the argument $2\pi f_d \tau_b$ (fast fading) seem to resemble the results derived for small mean burst lengths in the Gilbert-Elliott channel. In the same way, the performance results derived for small values of the argument $2\pi f_d \tau_b$ (slow fading) seem to resemble the results derived for large mean burst lengths in the Gilbert-Elliott channel. This observation confirms a statement made earlier which implied that a simple channel model, such as the Gilbert-Elliott model, can provide enough insights without the complexity of a more elaborate FSMC model.

Chapter 6 An Error Resilient Frame Structure for the AAL2

6.1 Introduction

One of the main characteristics of the AAL2 standard is that it improves bandwidth utilization by multiplexing low data rate and delay sensitive traffic from multiple sources into a single ATM virtual circuit. Nevertheless, as currently specified, the AAL2 standard does not perform very efficiently under high bit error rate links. One of the reasons for the poor performance of the AAL2 standard is because it introduces a frame structure within the payload of each ATM cell. The frame structure, as defined in the AAL2 standard, introduces additional header fields as part of the structure of each AAL2 packet. These AAL2 header fields can be corrupted by bit errors resulting in the discard of the AAL2 packets at the AAL2 layer. In addition, the AAL2 standard introduces a mechanism for the delineation of AAL2 packets inside the payload of the ATM cells, and the delineation mechanism is vulnerable to bit error on the AAL2 packet header fields.

In Chapter 5, we evaluated the performance improvements at the AAL2 layer by introducing diverse approaches to improve the performance of the AAL2 standard in error-prone links. Such approaches included the use of Forward Error Correction codes, as well as, the introduction of diversity mechanisms. In this chapter we propose a new approach to improve the performance of the AAL2 standard over error-prone channels. The proposal deals with the introduction of a novel mechanism for the delineation of CPS packets within the payload of the ATM cells. In addition the proposed mechanism can reduce the required overhead, due to the delineation fields, while preserving the interoperability with the standard AAL2.

This chapter is divided into 7 sections. Section 6.2 presents a description of the delineation mechanism used in the AAL2 standard. Section 6.3 describes the proposal of a new delineation mechanism. Section 6.4 describes how the new delineation mechanism is used to modify the delineation mechanism in the AAL2 standard. Numerical results, following an analytical approach, are presented in Section 6.5. And Section 6.6 presents simulation results to validate the results presented in Section 6.5. Finally a summary of this chapter is presented in Section 6.7.

6.2 Delineation over Standard AAL2

The AAL2 standard achieves efficient bandwidth utilization by multiplexing data from multiple sources within the payload of the AAL2 Common Part Sublayer Protocol Data Unit (CPS-PDU). The CPS-PDU consists of a single byte start field, *STF*, and a 47-byte payload. The CPS-PDU payload may carry zero, one or more (*complete* or *partial*) CPS packets. Each CPS packet is composed by a three byte Common Part Sublayer Packet Header (CPS-PH) and a variable size Common Part Sublayer Packet Payload (CPS-PP) [12], as shown in Figure 6.1.

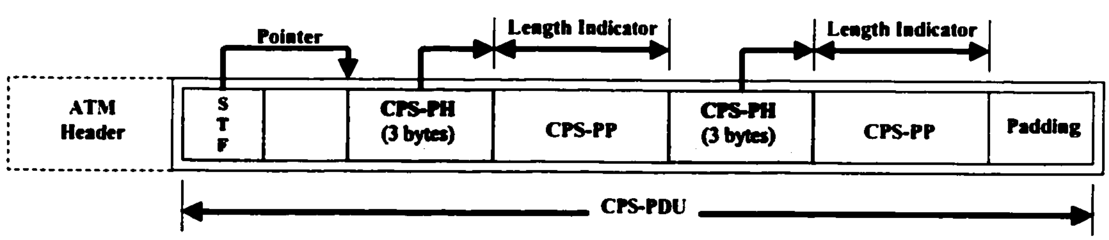

Figure 6.1: CPS packet delineation over standard AAL2.

Under the AAL2 standard, the CPS packet delineation is achieved by identifying the position of the first CPS packet in the CPS-PDU payload and then deriving the position of each subsequent CPS packet. To this matter, the *STF* field contains the required information to identify the position of the first CPS packet, while the Length Indicator (*LI*) field in each CPS-PH is used to derive the position of each subsequent CPS packet within the CPS-PDU payload, as depicted in Figure 6.1.

There are a variety of issues related to the delineation mechanism used in standard AAL2, especially when AAL2 packets are being transmitted over highly error-prone channels. One of these issues is related to the underlying dependency between CPS packets, as a result of the delineation mechanism. In other words, for a CPS packet not to be discarded it is required that its CPS-PH be correct (i.e., error-free) in addition to any previous header fields required to preserve delineation within the CPS-PDU payload, as depicted in Figure 6.1. For example, the first CPS packet in the CPS-PDU payload only relies on the ATM header, the *STF* and its own CPS-PH being correct for the CPS packet not to be lost or discarded at the ATM or AAL2 layer. On the other hand, the second CPS packet will have to rely on the same header fields as the first CPS packet, in addition to its own CPS-PH field. This means, that CPS packets can be discarded as a result of lost delineation within the CPS-PDU payload or lost due to a discarded ATM cell.

6.3 Improved Delineation Mechanism

The previous section described the structure of the AAL2 packet, including the mechanism used for the delineation of CPS packets within the CPS-PDU payload. In this Section a novel delineation mechanism is proposed for the delineation of CPS packets. This new delineation mechanism has been designed to improve the performance of the standard AAL2 packet structure in the presence of bit errors. This is achieved by introducing a new delineation field that maps the information regarding the location of CPS packets within the CPS-PDU payload, while reducing the overhead required for delineation of CPS packets. In addition, the proposed mechanism preserves most of the functionality provided by the standard AAL2.

According to the AAL2 standard, each CPS-PDU is composed of a sequence of 48 bytes. Within the CPS-PDU, the CPS packet delineation is implemented by means of the Start Field, *STF*, and the Length Indicator, *LI*, present in each CPS-PH. The proposed delineation mechanism is implemented by introducing a new Delineation Field (*DF*), which replaces the functionality provided by the *STF* and *LI* fields. Figure 6.2 depicts the process by which the new delineation field is created.

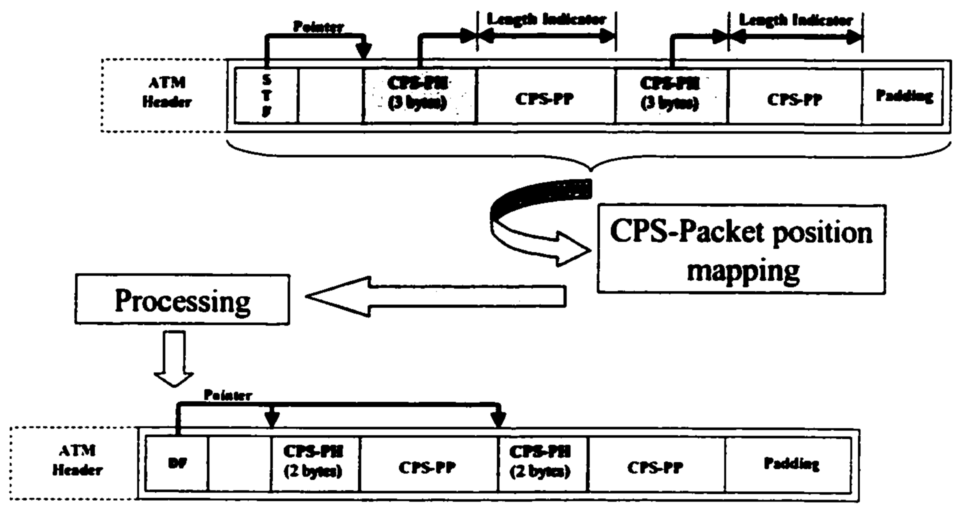

Figure 6.2: Delineation mechanism process.

In the process depicted in Figure 6.2, the first step consists in determining the position of CPS packets within the CPS-PDU. A delineation string is used to identify the position of AAL2 packets within the CPS-PDU. In the last "Processing" stage the delineation field, *DF*, is derived from the delineation string.

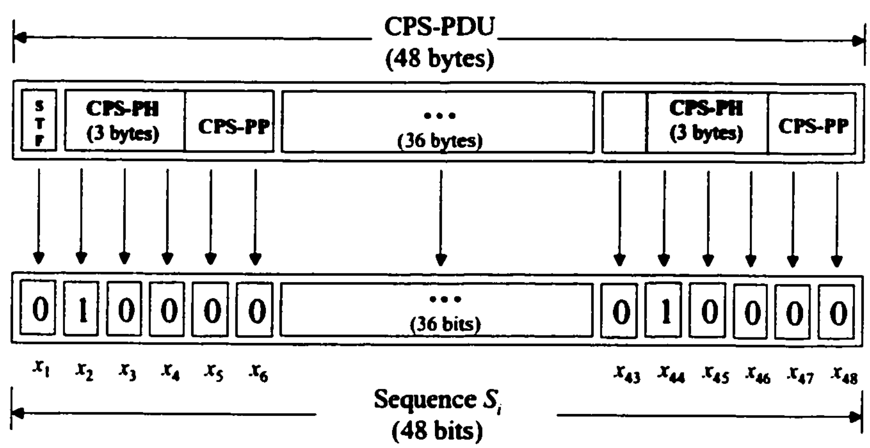

Figure 6.3: Delineation sequence mapping.

The first step outlined in Figure 6.2 is achieved by representing the CPS-PDU as a sequence $S_i = (x_1, x_2, \ldots, x_{48})$ of 48 bits (6 bytes), where $i = 1, 2, \ldots, N_x$ and N_x is equal to the number of possible combinations of S_i. Furthermore, there is a one-to-one correspondence from each of the 48 bytes from the CPS-PDU to each element x_k, $k = 1, 2, \ldots, 48$, as depicted in Figure 6.3. By definition, all elements x_k are equal to zero, except for those elements that are mapped from the CPS-PDU and correspond to the beginning of a CPS packet, for these cases, element x_k will be equal to one. Thus, sequence S_i is composed of the elements $x_k \in \{0,1\}\ \forall\ k = 1, 2, \ldots, 48$.

Due to the structure of a CPS-PDU, not all possible vectors $(x_1, x_2, \ldots, x_{48})$ correspond to a valid combination of sequence S_i. For instance, x_1 is always equal to 0 because the first byte in the CPS-PDU is allocated to the *STF* field. Furthermore, if $x_k = 1$ for any $2 \leq k \leq 48$, then x_{k+1}, x_{k+2} and x_{k+3} are equal to zero because each CPS packet is at least 4 bytes long (i.e., the minimum size of an AAL2 packet is 4 bytes); it consists of a 3 byte CPS-PH and a CPS packet payload that is at least one byte long. In general, let S_i be composed of a sequence of m bits. Then, vector S_i can be equal to any of $\psi(m,n)$ possible sequences, where $\psi(m,n)$ is a function of all the possible combinations of ones and zeros over m bits and n is equal to the number of complete CPS packets over m bits. Recall that the minimum size of a CPS packet is 4 bytes, which are mapped into sequence S_i as a 4-tuplet, T. The 4-tuplet, T, is composed of a bit "1" followed by three bits equal to "0".

Let n be the maximum possible number of complete CPS packets (i.e., CPS packets with a minimum size of 4 bytes that are not mapped beyond the boundaries of m bits) that fit within m bits, that is, $n = \lfloor m / 4 \rfloor$, where $\lfloor x \rfloor$ is the largest integer smaller or equal than x. Then $\psi(m,n)$ can be evaluated as the sum of ψ_1, ψ_2 and ψ_3, where:

- ψ_1 is defined as the number of possible combinations of $n+1$ CPS packets over m bits. That is, n CPS packets plus one CPS packet that is mapped across the boundary of the m bits. Figure 6.4 depicts some instances for this case. Then ψ_1 is given by,

$$\psi_1 = \sum_{k=1}^{m-4n} \binom{(m-k)-3n}{n}. \tag{63}$$

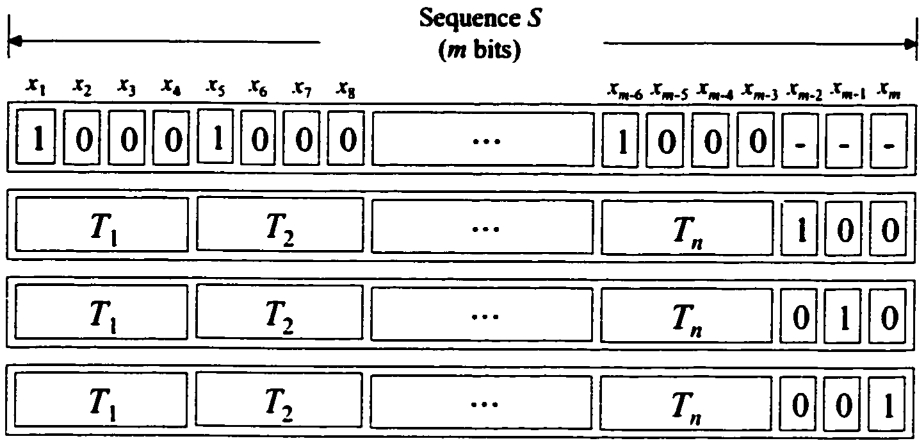

Figure 6.4 Example of n + 1 CPS packets in m bits.

- ψ_2 is defined as the number of possible combinations of 1, 2, …, n CPS packets over m bits. That is, ψ_2 is equal to the number of combinations of i = 1, 2, …, n 4-tuplets, T_i, over (m–3i). Figure 6.5(a) shows some examples of this case. Furthermore, given that a CPS packet can be mapped across CPS-PDU boundaries it is possible to have a situation as the one depicted in Figure 6.5(b). So we also account for all the possible combinations of (i–1) 4-tuplets over [j–3(i–1)], for j = m–3, m–2 and m–1. ψ_2 is given by,

$$\psi_2 = \sum_{i=1}^{n}\left[\binom{m-3i}{i} + \sum_{j=m-3}^{m-1}\binom{j-3(i-1)}{i-1}\right]. \tag{64}$$

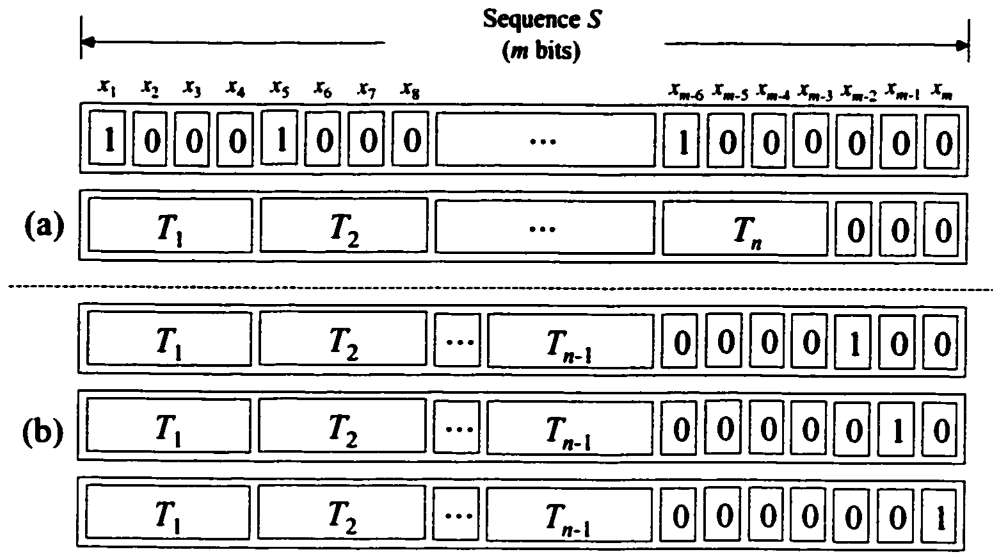

Figure 6.5 Example of *n* CPS packets in *m* bits.

- ψ_3 is defined to be equal to one. This term accounts for the single case where no CPS packets are carried over m bits and S_i is composed of a sequence of bits equal to "0".

Therefore, the number of possible combinations of S_i is given by,

$$\psi(m,n)=\sum_{i=1}^{n}\left[\binom{m-3i}{i}+\sum_{j=m-3}^{m-1}\binom{j-3(i-1)}{i-1}\right]+\sum_{k=1}^{m-4n}\binom{(m-k)-3n}{n}+1. \qquad (65)$$

For AAL2, it follows that element x_1 is always equal to zero, as it corresponds to the *STF*, so $m = 48 - 1 = 47$. Thus, the number of possible combinations, of sequence $S_i = (x_1, x_2, \dots, x_{48})$ is $N_x = \psi(47, 11)$.

From the previous mechanism it follows that for AAL2 the size of any sequence S_i is 48 bits (6 bytes), which results in a relatively high overhead for ATM. Due to the high redundancy of data in sequence S_i (i.e., for $k = 1, 2, \dots, 48$, the number of elements x_k equal to zero is always greater than that of x_k equal to one) it is possible to introduce compression, which becomes the last step in creating the Delineation Field, *DF*.

The compression of the delineation sequence, S_i, $i = 1, 2, \ldots, N_x$, is achieved by introducing the concept of a delineation matrix **D**. The m elements of the vector $S_i = (x_1, x_2, \ldots, x_m)$ are mapped into the elements, d_{ij}, i=1,2,...,r and j=1,2,...,c, of matrix **D** with r rows, c columns and $rc \geq m$. Starting at x_1, matrix **D** is filled one row at a time, thus $d_{ij} = x_k$ following:

$$i = \lceil k / c \rceil, \; j = k - c(i-1) \;\; \forall \; k = 1, 2, \ldots, m, \tag{66}$$

where $\lceil x \rceil$ is the smallest integer greater or equal than x. Figure 6.6 illustrates two examples of the mapping of delineation sequence S_i into a delineation matrix **D**.

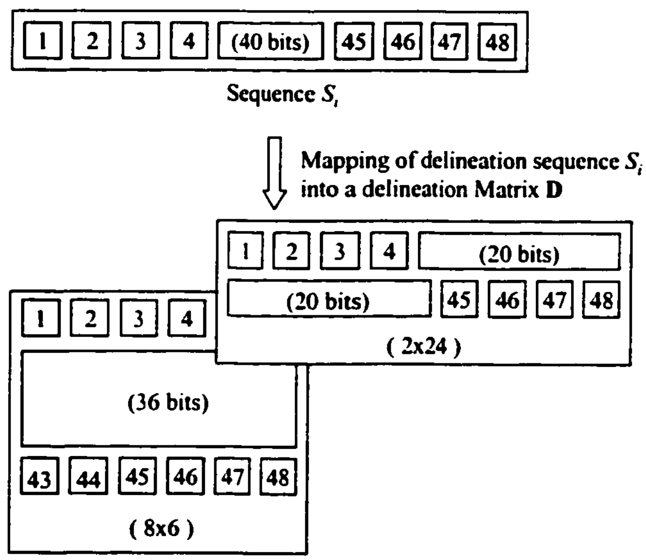

Figure 6.6: Mapping of a delineation sequence into a matrix D.

From the previous definition, it follows that there are many possible combinations such that condition $rc \geq m$ is valid. The selection of an appropriate dimension for matrix **D** must be such that $rc = m$ and $r, c \notin \{1, m\}$. The selection of values for r and c such that $rc > m$ must be avoided, as the number of possible combinations for matrix **D** will be greater than that of S_i, which is equal to N_x.

In the case of AAL2, $S_i = (x_1, x_2, \ldots, x_{48})$ for $i = 1, 2, \ldots, N_x$ and $N_x = \psi(47, 11)$. This means that possible values for r and c for matrix **D** include $r, c \in \{2, 3, 4, 6, 8, 12, 16, 24\}$ $\forall$ $rc = 48$. Mapping between elements x_k and d_{ij} is evaluated as previously described.

From matrix **D**, the sequence R_i is defined as the sequence of bits $R_i = (y_1, y_2, \ldots, y_c)$ for $i = 1, 2, \ldots N_y$ that corresponds to a valid row vector, N_y is equal to the number of possible combinations (i.e., in the sample space **R**) of R_i and c is the total number of columns in matrix **D**. In addition, the sequence L_j is defined as the sequence of bits that form row vector j, that is, $L_j = (d_{j1}, d_{j2}, \ldots, d_{jc})$ for $j = 1, 2, \ldots, r$. From the previous definition, it should be clear that $\{L_j\}_{j=1,2,\ldots,r} \in \mathbf{R}$.

Under AAL2, the number of valid combinations of R_i is given by,

$$N_y = \psi(c, \lfloor c / 4 \rfloor). \qquad (67)$$

Table 12 shows the values of N_y, assuming AAL2, for different combinations of $r, c \in \{2, 3, 4, 6, 8, 12, 16, 24\}$ for $rc = 48$.

Table 12: Size of sample space R.

Order of matrix **D**	Ny
24 × 2	3
16 × 3	4
12 × 4	5
8 × 6	10
6 × 8	19
4 × 12	69
3 × 16	250
2 × 24	3292

For any given matrix **D**, compression is used over all row sequences R_i, $i = 1, 2, \ldots N_y$ by using Huffman codes [83]. Huffman coding is a statistical scheme that relies on the statistical nature of occurrences of input elements, in this case R_i, for the proper assignment of Huffman codes to each input element. Consequently, there is one Huffman code for each sequence R_r. Thus, for each row vector L_j, j=1,2,...,r in matrix **D**, there is also a Huffman code associated with it, as $L_j \in \mathbf{R}$, $\forall j = 1, 2,..., r$. The sequence of bits from the Huffman codes associated with L_j are used to form the Delineation Sequence, *DS*, that is part of the Delineation Field, *DF*.

6.4 Improved Delineation Mechanism for the AAL2 standard

The introduction of the delineation field, *DF*, in the AAL2 packet will result in the removal of the *STF* and *LI*s fields from the CPS-PDU. The *DF* field provides for functionality equivalent to the *STF* and *LI* fields, which are required for the delineation of CPS packets within the CPS-PDU.

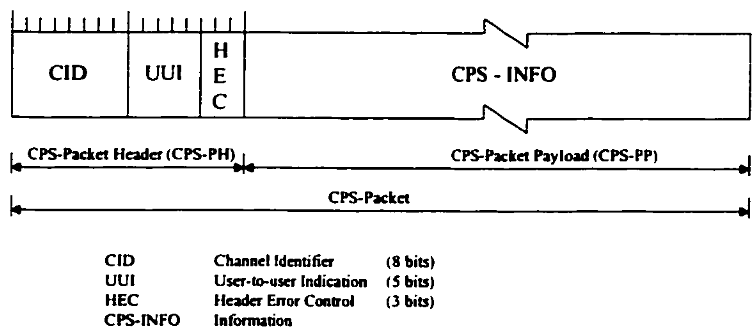

Figure 6.7: Proposed CPS packet format.

The removal of the *LI* field (6 bits) from the CPS-PH results in a CPS-PH of size 18 bits, which is not a multiple of eight. Thus, in addition to the removal of the *LI* field, it is further required that two additional bits be removed from the CPS-PH. It is proposed that the *HEC* field contains the remainder of the division (modulo 2), by the generator polynomial X^3+X+1, of the product of X^3 and the contents of the first 13 bits of the CPS-PH. In this way, the *HEC* field will only require 3 bits and therefore the resulting CPS-PH will be further reduced to a more suitable size of 16 bits (2 bytes). Figure 6.7 shows the format of the CPS packet under the proposed delineation scheme.

A novel mechanism has been proposed for the introduction of a new Delineation Field, *DF*. Furthermore, this mechanism introduces the concept of a delineation matrix **D** and Table 12 shows all possible options for selecting the order of matrix **D**. However the question of selecting a proper delineation matrix **D** for the particular case of AAL2 has not been addressed.

The selection of an adequate matrix **D** relies on the constraint that the overhead introduced by the new delineation mechanism should not be greater than the overhead required in the standard AAL2.

Table 13: Huffman codes size for R_i.

Matrix D	N_y	Max. Huffman Codes Size (bits)
24 × 2	3	2
16 × 3	4	3
12 × 4	5	3
8 × 6	10	5
6 × 8	19	6
4 × 12	69	8
3 × 16	250	9
2 × 24	3292	13

The process of creating the Delineation Field, *DF*, includes the compression of a vector sequence S using Huffman coding. Under the constraint that the resulting *DF* field should be as short as possible, Huffman coding is done by assuming a very high probability of occurrence for the vector sequence S with elements all equal to zero; the resulting Huffman code for the sequence all zeros will be 1-bit. A uniform probability of occurrence is assumed for the rest of possible combinations of sequence S. Table 13 shows the size of the largest resulting Huffman code for different dimensions of matrix **D**.

Let N_r be equal to the number of bits that are removed from the CPS-PDU for the introduction of the new delineation field *DF*; that is, 8 bits from the *STF* field and 8 bits for each CPS packet in the CPS-PDU payload. Let N_{DF} be equal to the size, in bits, of the resulting delineation field *DF*. Then the overhead ratio, Γ, is defined as

$$\Gamma = \frac{N_{DF}}{N_r}. \tag{68}$$

It is clear that if $\Gamma > 1$ then the overhead introduced by the new delineation field is greater than overhead removed, N_r.

Assuming that $N_P = 1, 2, \ldots, 12$ CPS packets, of equal size, are carried within the CPS-PDU payload, then a possible set of values for sequence S is shown in Table 14.

Table 14: Delineation sequence strings.

N_P	Vector Sequence S_i
1	010000000000000000000000000000000000000000000000
2	010000000000000000000000010000000000000000000000
3	010000000000000001000000000000000100000000000000
4	010000000000010000000000010000000000010000000000
5	010000000010000000010000000010000000010000000000
6	010000000100000001000000010000000100000001000000
7	010000001000000100000010000001000000100000010000
8	010000010000010000010000010000010000010000010000
9	010000100001000010000100001000010000100001000000
10	010000100001000010000100001000010000100001000010
11	010001000100010001000100010001000100010001000000
12	010001000100010001000100010001000100010001000100

Table 14 shows a set of vector sequences S_i for the evaluation of the overhead ratio, Γ, as a function of the number of CPS packets, N_P, in the CPS-PDU payload. It should be noted that the set of sequences S_i shown in Table 14, is ideal for the evaluation of the overhead ratio Γ, as they include all possible worst-case scenarios for a given matrix **D**. In other words, by evaluating these sequences, it is possible to analyze all those cases in which a minimum amount of overhead N_r, is removed from the CPS-PDU while the size of the delineation field N_{DF} is maximized.

From the list of possible vector sequences S_i, shown in Table 14, and assuming the largest Huffman codes for different matrix **D**, shown in Table 13, it follows that it is possible to evaluate the overhead ratio Γ as a function of the number of CPS packets N_p and the order of matrix **D**, as shown in Table 15.

Table 15: Overhead ratio, Γ, for a given matrix D.

Matrix D	Number of CPS packets, N_p												
	0	**1**	**2**	**3**	**4**	**5**	**6**	**7**	**8**	**9**	**10**	**11**	**12**
24 × 2	4	2	1.33	1	0.8	0.67	0.71	0.63	0.56	0.5	0.45	0.42	0.38
16 × 3	3	1.5	1	1	0.8	0.67	0.57	0.63	0.56	0.5	0.45	0.5	0.46
12 × 4	2	1.5	1	0.75	0.6	0.67	0.57	0.5	0.44	0.5	0.45	0.42	0.38
8 × 6	2	1	1	0.75	0.8	0.67	0.71	0.63	0.67	0.5	0.55	0.42	0.46
6 × 8	1	1	1	0.75	0.8	0.83	0.71	0.63	0.56	0.5	0.45	0.42	0.38
4 × 12	1	1	1	1	1	0.83	0.71	0.63	0.56	0.5	0.45	0.42	0.38
3 × 16	1	1	1	1	0.8	0.67	0.57	0.5	0.44	0.4	0.36	0.33	0.31
2 × 24	1	1	1.33	1	0.8	0.67	0.57	0.5	0.44	0.4	0.36	0.33	0.31

From Table 15, it is clear that the selection of matrix **D** of order 24×2, 16×3, 12×4, 8×6 or 2×24 are not good selections, as they have at least one case for which the overhead introduced by the delineation field is greater than the removed overhead N_r. From the remaining options, namely 6×8, 4×12 and 3×16, it is observed that the matrix **D** of order 3×16 provides the best performance in terms of overhead reduction, as shown in Figure 6.8.

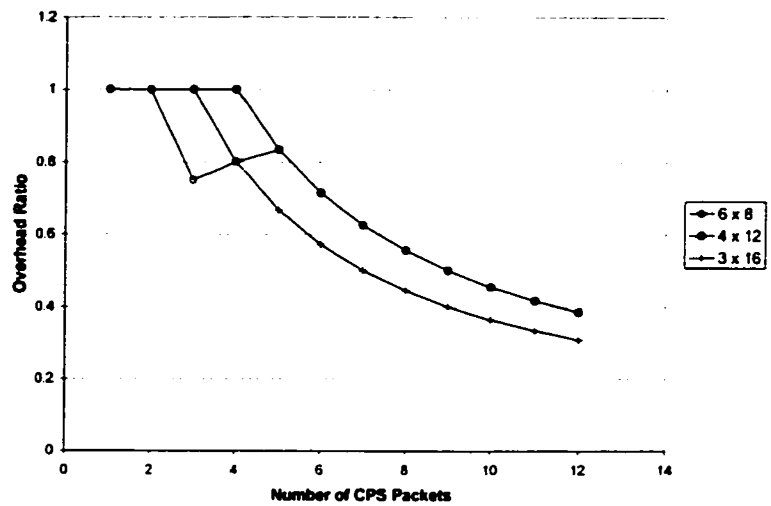

Figure 6.8: Overhead Ratio, Γ.

For a matrix **D** of order 3×16, the overhead in bytes as a function of the number of CPS packets is shown in Figure 6.9.

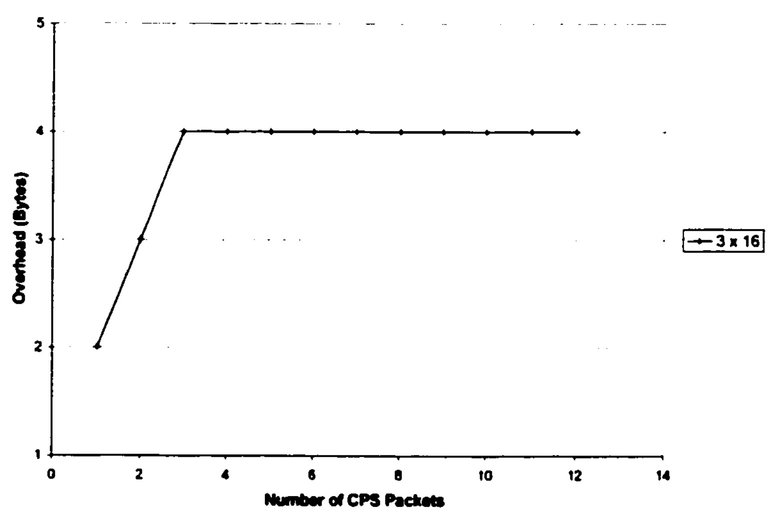

Figure 6.9: Delineation Field, *DF*, for Matrix D (3×16).

From Figure 6.9, it is observed that the size of the delineation sequence, *DS*, will range from 2 to 4 bytes depending on the number of CPS packets. This requires a 2-bit delineation sequence length indicator (*DSLI*) to be included along with the *DS*. The proposed values for the length indicator and their description are presented in Table 16.

Table 16: Delineation sequence length indicator.

DSLI	DS field length, l_{DS}
0 0	l_{DS} = 1 byte
0 1	l_{DS} = 2 bytes
1 0	l_{DS} = 3 bytes
1 1	l_{DS} = 4 bytes

Figure 6.10, shows the structure of the Delineation Field, *DF*, in the CPS-PDU under the proposed delineation scheme. It should be noted that results presented in Table 15, Figure 6.8 and Figure 6.9 have accounted for the introduction of the *DSLI* field, as part of the *DF* field. Furthermore, a *DSLI* of size 3-bits is required for those cases in which matrix **D** has a dimension of 24×2, 16×3, 12×4 or 8×6, as it is not possible to represent all possible lengths for the resulting *DS* field with only 2-bits.

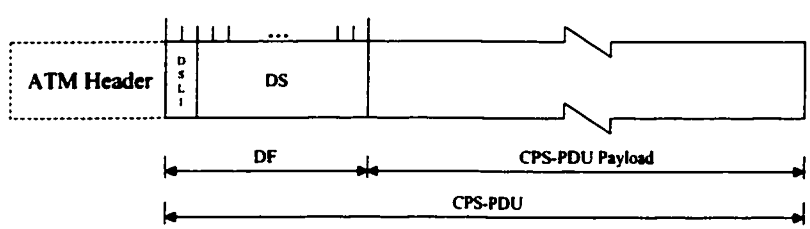

DF Delineation Field (1 to 4 bytes)
DSLI Delineation Sequence Length Indicator (2 bits)
DS Delineation Sequence (3 to 27 bits)

Figure 6.10: CPS-PDU format using the DF field.

Another functionality that is provided in standard AAL2 is padding within the CPS-PDU payload. Under the proposed delineation mechanism, padding will be handled by setting to zero all padding bits within the CPS-PDU payload, as it is done in the AAL2 standard.

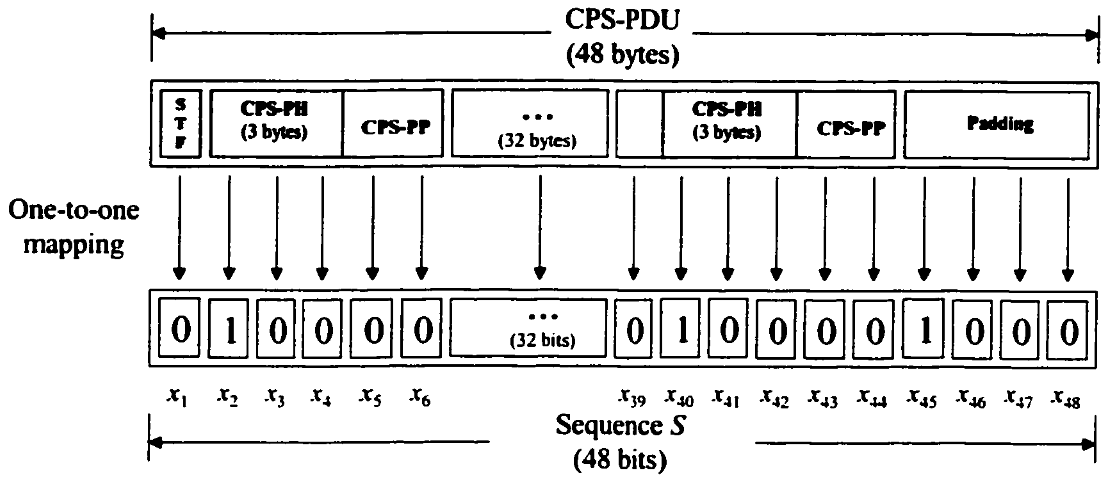

Figure 6.11: Padding indication within the delineation sequence.

In the vector sequence S, the element x_k that corresponds to the beginning of the padding string should be set to "1", thus indicating the beginning of a "dummy" CPS packet, as shown in Figure 6.11. After the *DF* field is decoded at the receiver side, the presence of all bits equal to zero in the last "dummy" CPS packet will indicate the presence of padding bits.

The interoperability of the proposed scheme with standard AAL2 will require the introduction of Interworking Function nodes which will allow the mapping between the standard AAL2 protocol and the proposed modified AAL2 protocol. The implementation of such Interworking Function nodes, as well as, the level of complexity introduced by such devices remains a topic for future work.

6.5 Numerical Results over the Gilbert-Elliott Channel

The numerical results for performance metrics *mCLR* and *mPER*, derived in equations (35) and (38), are presented in this section.

For consistency with the results presented in previous chapters, the following channel parameters were used for the Gilbert-Elliott model: steady state channel BER is $\varepsilon = 10^{-3}$ and state bit error probabilities are $P_c(0) = 0$ and $P_c(1) = 0.5$.

Since one of the main characteristics of the AAL2 standard is the ability to multiplex information from multiple sources, it is of interest to study the performance of AAL2 over the burst error channel for CPS packets with different payload size. For this purpose, CPS packets with payload size of 24 bits, 96 bits and 352 bits are analyzed and presented in this section. Figure 6.12 shows performance results, as a function of the mean burst length τ, for each of the CPS packets in the CPS-PDU for the case CPS-PP of size 24 bits, N = 7, under the proposed delineation mechanism. Figure 6.13 shows performance results, as a function of the mean burst length τ, for each of the CPS packets in the CPS-PDU for the case CPS-PP of size 96 bits, N = 3, under the proposed delineation mechanism. Figure 6.14 show average performance results, as a function of the mean burst length τ, for each of the CPS packets in the CPS-PDU for the case CPS-PP of size 24, 96 and 352 bits, under the proposed delineation mechanism.

In addition, simulations results are presented in Section 6.6. The simulation results were obtained using the network simulator (ns-2) tool [55]. As part of the simulation, two ATM nodes exchanged AAL2 packets (using the proposed delineation mechanism) over a link, which is error-prone and characterized by the Gilbert-Elliot model.

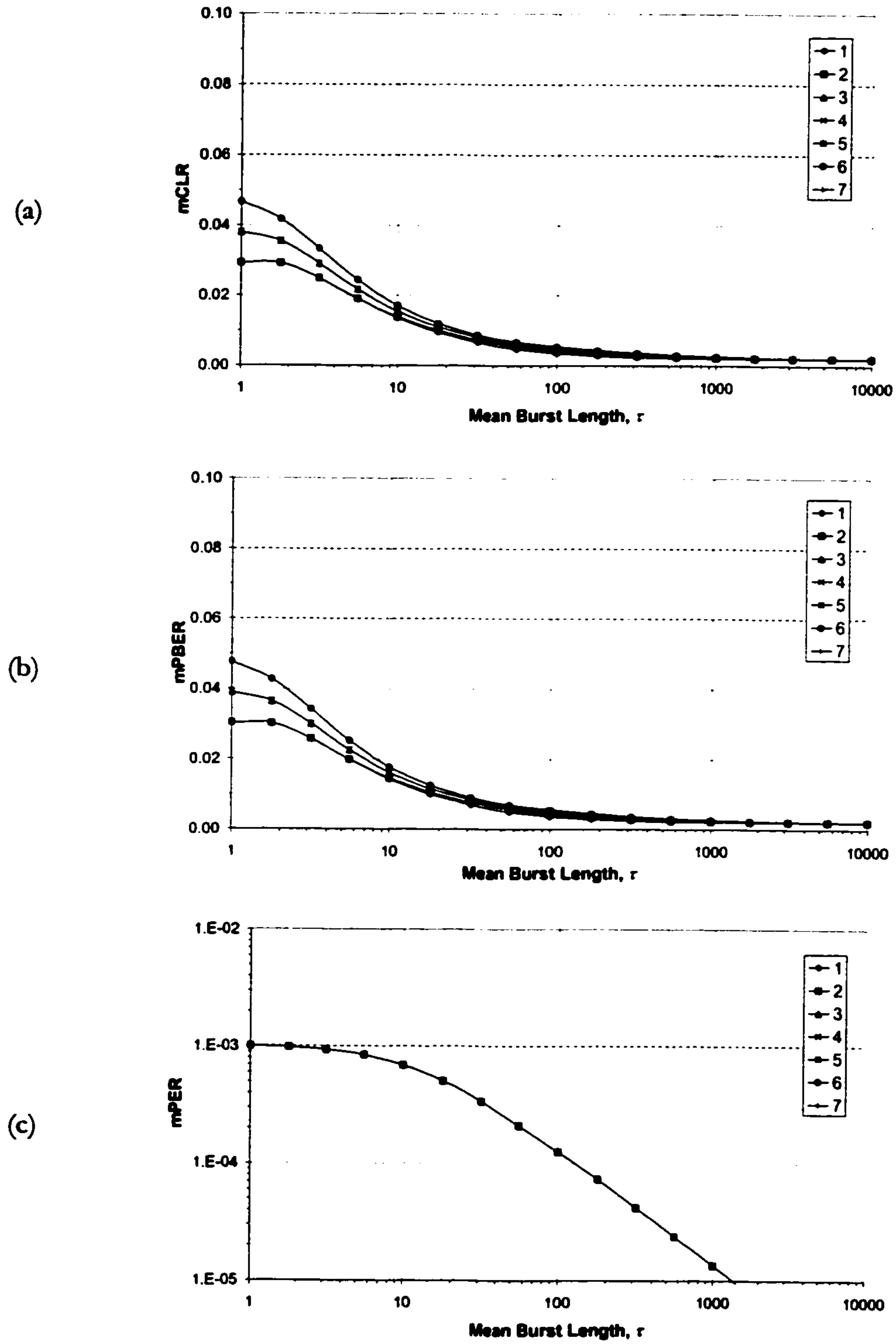

Figure 6.12: Performance results for CPS-PP size 24 bits.

(a)

(b)

(c)

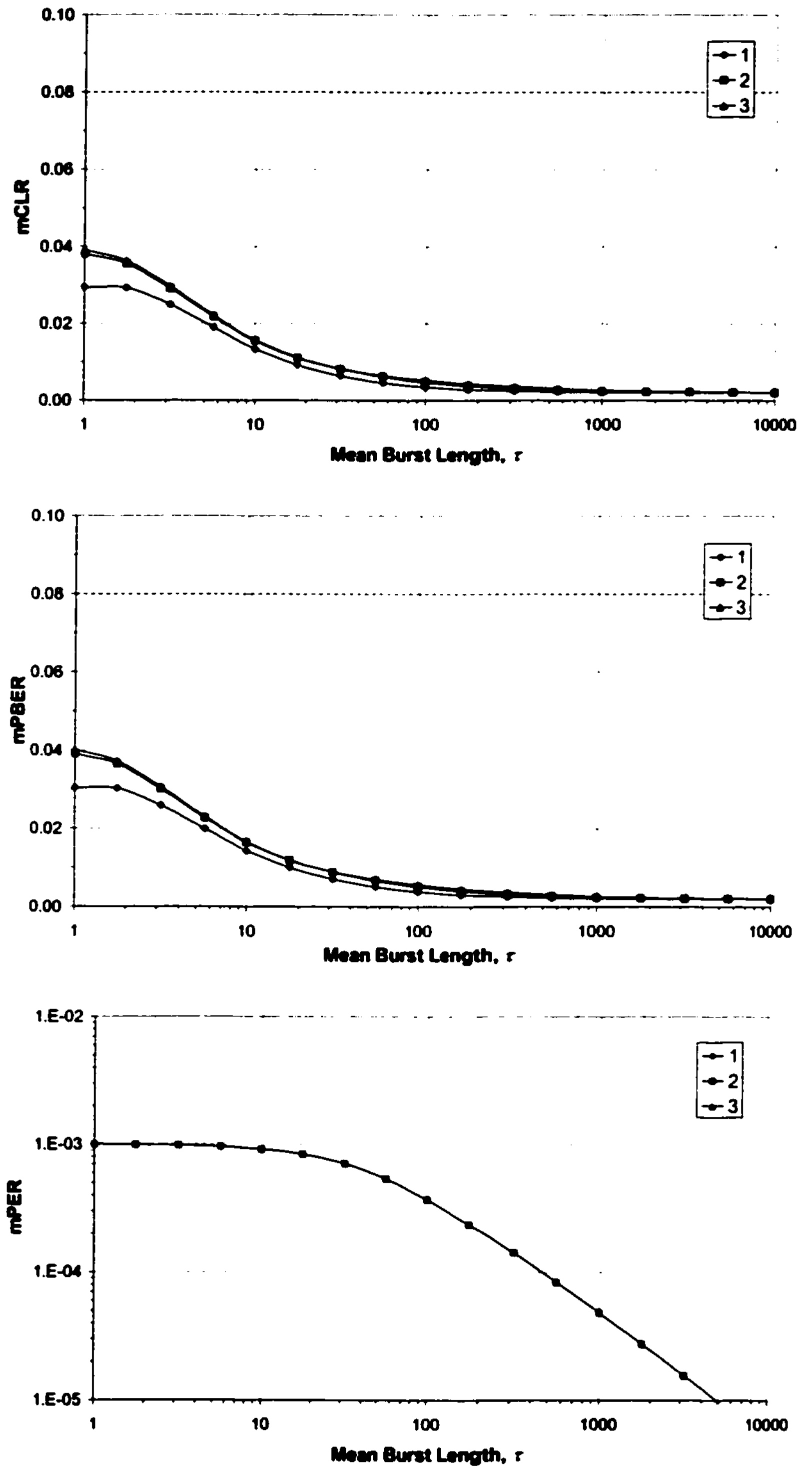

Figure 6.13: Performance results for CPS-PP size 96 bits.

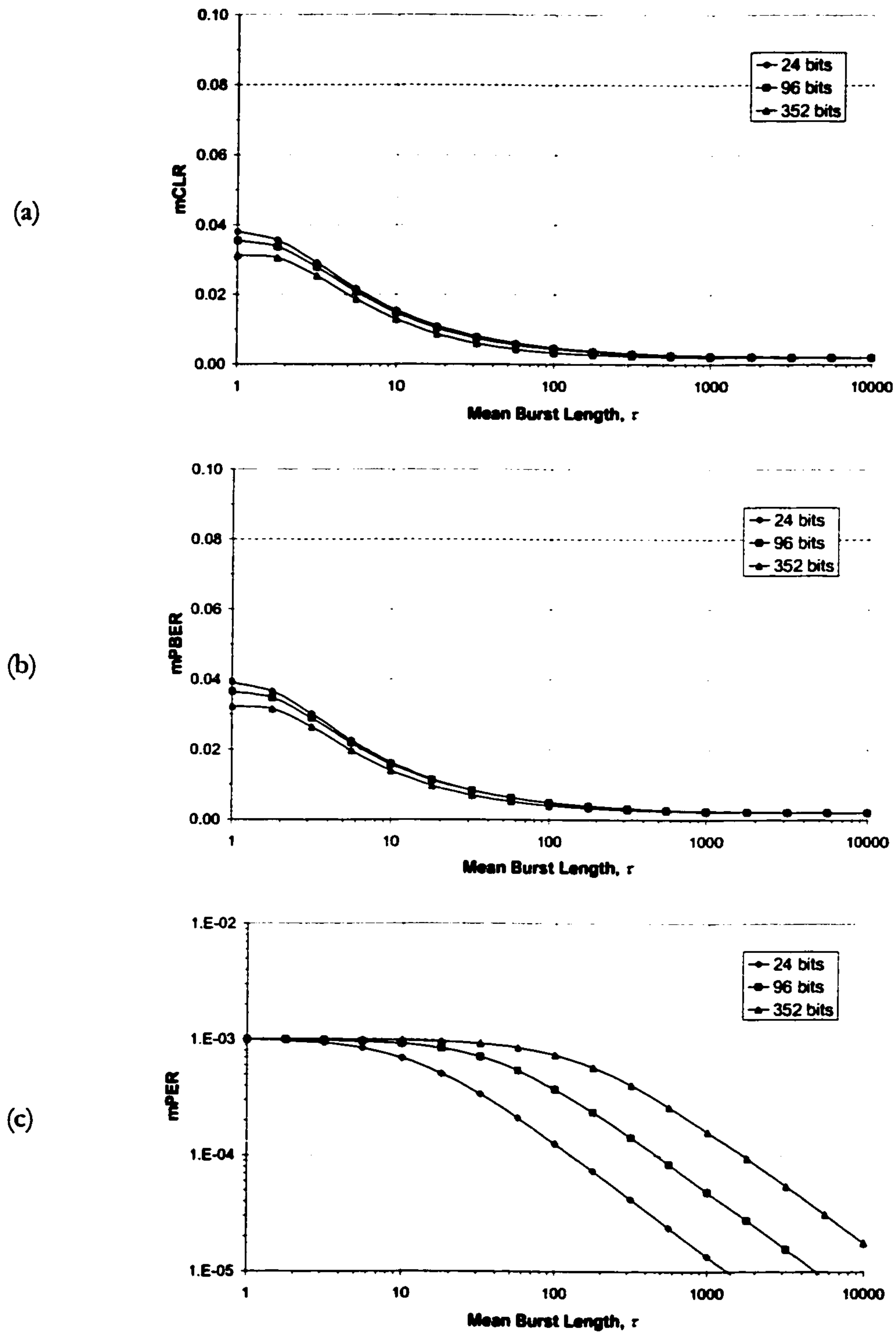

Figure 6.14: Average performance results.

By comparing the performance results obtained using the proposed delineation mechanism against the results obtained under the standard AAL2 delineation, it can be observed that under the proposed delineation mechanism the probability that a CPS packet will be lost, due to corrupted delineation fields, is essentially the same (for a given mean burst length τ) for any CPS packet regardless of its relative position within the CPS-PDU or the size of the CPS packet payload. For example for AAL2 packets with payload of 24 bits, in Figure 4.4(a) under standard AAL2 delineation, the probability that the first CPS packet will get lost, for a mean burst length $\tau = 1$, is equal to 0.03 (or 3%), while the probability that the last CPS packet is lost is 0.16 (or 16%). On the other hand, in Figure 6.12(a) under the proposed delineation mechanism, the probability that the first CPS packet will get lost, for a mean burst length $\tau = 1$, is equal to 0.03 (or 3%), while the probability that the last CPS packet is lost is less than 0.05 (or 5%).

6.6 Simulation Results

The numerical results presented in Section 6.5 relied on the analytical derivation of expressions to evaluate the performance metrics of interest at the AAL2 following an approach similar to the one described in Chapter 4. However the analysis relies on the assumption that AAL2 packets are not mapped beyond the boundaries of a CPS-PDU. Recall that this assumption is important in the derivation of closed form expressions. In this section, we present numerical results obtained under simulation to be able to validate the analytical results presented in Section 6.5. It should be noted that the simulation implementation allows for AAL2 packets to be mapped beyond the boundaries of a CPS-PDU.

The simulation assumes two ATM nodes exchanging information over a FSMC modeled link. Figure 6.15 shows the block diagram of the network architecture implemented in the ns-2 simulation. The functionality for the improved delineation mechanism for AAL2 is implemented as part of the ATM/AAL2 Agents at the transmitter and receiver nodes, as illustrated in Figure 6.15.

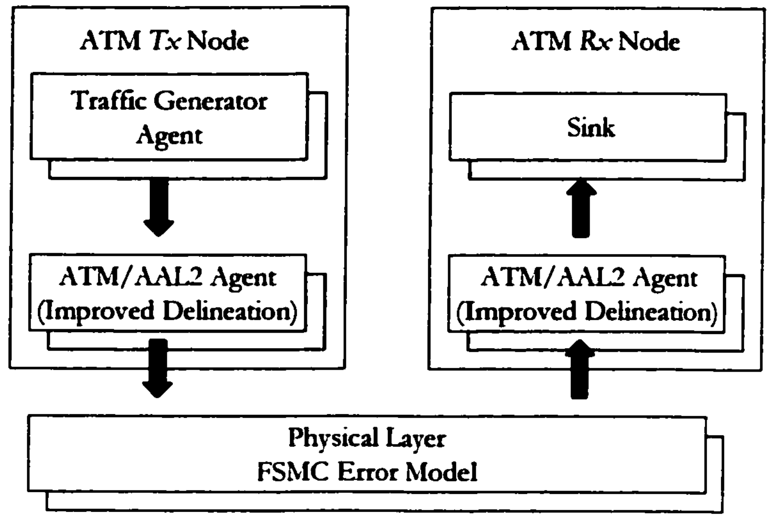

Figure 6.15: Block diagram of network architecture for improved AAL2 delineation.

At the sender the Traffic Generator Agent generates a constant stream of bits to the ATM/AAL2 Agent. The ATM/AAL2 Agent receives the information from the Traffic Generator Agent and encapsulates the information by creating fixed size AAL2 packets and the AAL2 packets are structured as part of the CPS-PDU following the implementation for the improved delineation mechanism described in Section 6.4. The information is then sent by the ATM/AAL2 Agent to the physical layer and then transmitted over the link. The size of the AAL2 packets is defined by a parameter specified as part of the simulation script. To keep track of the bit errors introduced by the link, a string of 424 bits (all equal to "1") is associated to each transmitted ATM cell. Bit errors introduced by the link will result in a bit switched from "1" to "0".

In the simulation the error-prone channel is characterized by a FSMC model. In this case the channel is characterized by a two-state Markov chain (i.e., Gilbert-Elliott model). The Gilbert-Elliot model parameters are specified as part of the simulation script. These parameters include the channel BER ε, the mean burst length τ (i.e., the average time spent in the "bad" state) and the probability of errors on each of the two states. For the purpose of the numerical results presented in this section, the channel BER was set to $\varepsilon = 10^{-3}$ and the state error probabilities were $P_e(0) = 0$ and $P_e(1) = 0.5$.

At the other end of the transmission link, the ATM cells are received and examined by the receiver's ATM/AAL2 Agent. If an ATM cell is flagged with bit errors, then the Agent will proceed to check the ATM and the AAL2 headers. The simulator assumes that the HEC code in the ATM header can correct up to one bit in error. The delineation field DF and the CPS-PH fields (i.e., the AAL2 packet headers) do not provide for any error correction capability, as defined in the ITU-T AAL2 standard. Thus the AAL2 packets will be lost if there are two or more bit error in the ATM cell header or if an AAL2 header field is corrupted by bit errors. In addition the ATM/AAL2 Agent keeps track of bit errors on those AAL2 packets that are not lost or discarded at the ATM or AAL2 layer. Once the ATM cell has been inspected for bit errors it is sent to a sink module responsible of destroying the ATM cell.

The numerical results obtained with the ns-2 simulator are presented in Figure 6.16. These results are plotted against the mean burst length τ, which is defined to be the average time spent on the "bad" state of the two-state Markov link model. In addition Figure 6.16 presents the analytical results derived in Section 6.5 for comparison purposes. The simulation results are plotted using solid lines and the plot labels have the notation (S), whereas the analytical results are plotted using dashed lines and the labels have the notation (A).

From the performance results presented for the performance metrics illustrated in Figure 6.16, it can be observed that for an AAL2 packet with payload size of 352 bits (44 bytes) the simulation results follow very closely the results derived with the analytical expression. This observation is due to the fact that the AAL2 packets with payload size equal to 352 bits are carried by only one ATM cell and therefore there is no impact due to AAL2 packets being mapped beyond the boundaries of a CPS-PDU. On the other hand the performance results for metrics *mCLR* and *mPBER* derived in the simulation are different to the numerical results derived with the analytical approach using expressions (35) and (39), which are used to evaluate the performance metrics *mCLR* and *mPBER* respectively. In Figure 6.16(a) it can be observed that for small values of the mean burst length τ, the simulation results indicate that the probability of losses for AAL2 packets with payload size of 24 bits is lower than that of AAL2 packets with payload of 96 bits, which is contrary to the numerical results derived with the analytical expressions.

(a)

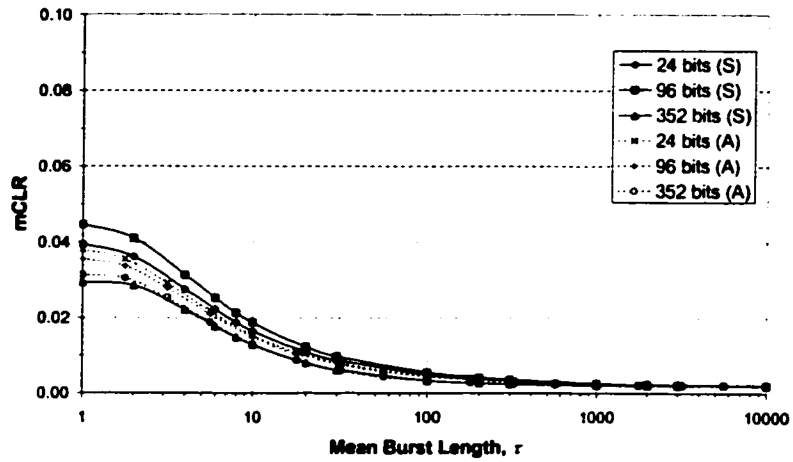

(b)

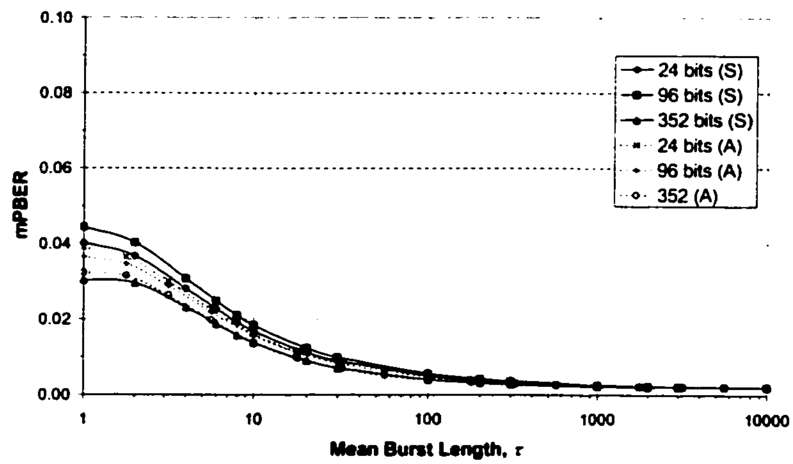

(c)

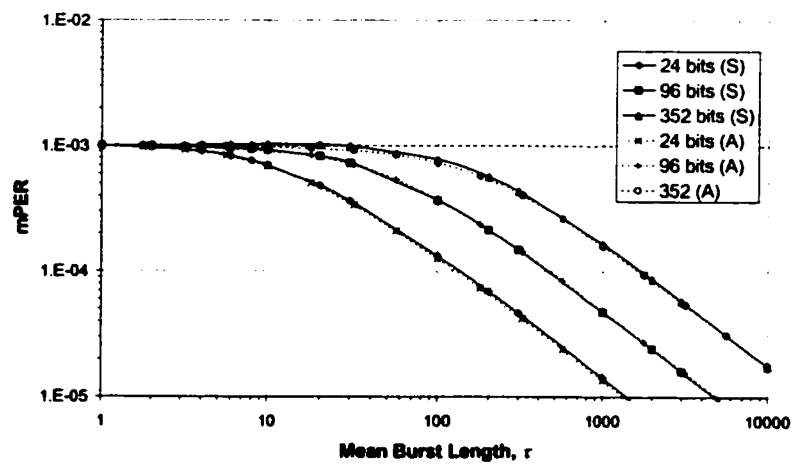

Figure 6.16: Simulation Results.

This observation can be explained as follows. The simulation implementation assumes that the AAL2 packets can be mapped between two CPS-PDUs, that is, two ATM cells can carry one AAL2 packet. It is clear that the probability of a lost AAL2 packet is greater for those AAL2 packets that are carried by two ATM cells than that of the AAL2 packets that are carried by only one ATM cell. This statement is derived from the observation that the probability of losing an AAL2 packet that is carried by two ATM cells is a function of the probability that one or both ATM cells are discarded due to bit errors on their ATM header fields.

To explain the simulation results for metric *mCLR*, illustrated in Figure 6.16(a), we concentrate on the particular case where the mean burst length is equal to $\tau = 1$. The simulation assumes that AAL2 packets can be mapped beyond the boundaries of the CPS-PDU. Then the CPS-PDU frame structure for the AAL2 packets with payload size equal to 24 bits (3 bytes) is like the one shown in Figure 6.17. In this case the AAL2 packets size is 5 bytes (recall that under the proposed delineation mechanism the AAL2 packets header is only 2 bytes long). Based on Figure 6.17 we can see that every 5 ATM cells results in one ATM cell which does not have the last AAL2 packet being mapped beyond the boundaries of the CPS-PDU.

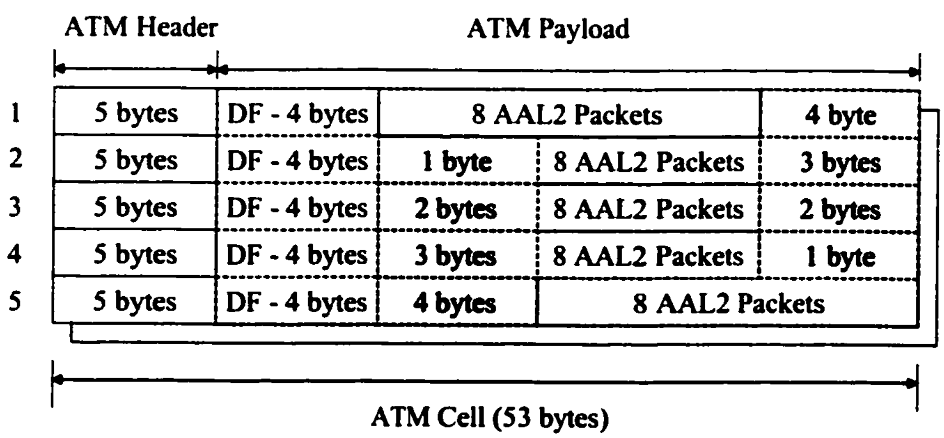

Figure 6.17: ATM cell structure for AAL2 packets of size 5 bytes

The same reasoning is derived for the AAL2 packets with payload size equal to 96 bits (12 bytes). The resulting AAL2 packets size is 14 bytes. Then based on Figure 6.18 we can observe that every 7 ATM cells results in one ATM cell which does not have the last AAL2 packet being mapped beyond the boundaries of the CPS-PDU.

	ATM Header	ATM Payload			
1	5 bytes	DF - 4 bytes	3 AAL2 Packets		2 byte
2	5 bytes	DF - 4 bytes	12 bytes	2 AAL2 Packets	4 bytes
3	5 bytes	DF - 4 bytes	10 bytes	2 AAL2 Packets	6 bytes
4	5 bytes	DF - 4 bytes	8 bytes	2 AAL2 Packets	8 byte
5	5 bytes	DF - 4 bytes	6 bytes	2 AAL2 Packets	10 byte
6	5 bytes	DF - 4 bytes	4 bytes	2 AAL2 Packets	12 bytes
7	5 bytes	DF - 4 bytes	2 bytes	3 AAL2 Packets	

ATM Cell (53 bytes)

Figure 6.18: ATM cell structure for AAL2 packets of size 12 bytes.

Then the performance metric $mCLR$ can be derived as a function of the number n_L of AAL2 packets that are exposed to a low probability of losses (i.e., the AAL2 packets that are not mapped beyond the CPS-PDU) defined as $mCLR_L$ and the number n_H of AAL2 packets that are exposed to a high probability of losses (i.e., the AAL2 packets that are mapped beyond the CPS-PDU) defined as $mCLR_H$. Then $mCLR$ can be calculated as

$$mCLR = \frac{n_L \cdot mCLR_L + n_H \cdot mCLR_H}{n_L + n_H}. \qquad (69)$$

The probability $mCLR_L$ can be evaluated by using a modified representation of Expression (30), which is later used to evaluate the loss probability of the m-th AAL2 packet by means of Expression (31), as explained in Section 4.2. Then the evaluated loss probability of the AAL2 packets that are not mapped beyond the CPS-PDU (for a mean burst length $\tau = 1$) is equal to $mCLR_L = 4.76\times10^{-2}$. Similarly, the evaluated loss probability of the AAL2 packets that are mapped beyond the boundaries of the CPS-PDU (for a mean burst length $\tau = 1$) is equal to $mCLR_{H} = 7.83\times10^{-2}$. From these probabilities it is now possible to evaluate the loss probability for the AAL2 packets with payload size equal to 24 bits given that $n_L = 40$ and $n_H = 4$ (as illustrated in Figure 6.17), that is,

$$mCLR_{24} = \frac{40\cdot 4.76\times10^{-2} + 4\cdot 7.83\times10^{-2}}{40+4} = 5.03\times10^{-2}, \tag{70}$$

and the loss probability for the AAL2 packets with payload size equal to 96 bits, given that n_L = 16 and $n_H = 6$ (as illustrated in Figure 6.18), is equal to

$$mCLR_{96} = \frac{16\cdot 4.76\times10^{-2} + 6\cdot 7.83\times10^{-2}}{16+6} = 5.6\times10^{-2}. \tag{71}$$

The numerical result presented in (70) and (71) corroborate the simulation results presented in Figure 6.16(a).

The numerical results for performance metric *mPBER*, illustrated in Figure 6.16(b), are similar to those of *mCLR*. This observation has been explained in Section 4.3 and is due to the fact that the performance metric *mPBER* is related to the performance *mCLR*, as defined in Expression (39). Therefore the results presented for performance metric *mPBER* imply that the probability of a lost AAL2 packet (or *mCLR*) has a very important impact on the error rate observed at the layers above the AAL2 layer.

With respect to the numerical results for performance metric *mPER*, illustrated in Figure 6.16(c), we can observe that the simulation results agree with the analytical results derived in the previous section. In Section 6.7 we present a summary of the most important results presented through out this chapter.

6.7 Summary

From the early stages of this research, it was clearly identified that the AAL2 standard was vulnerable to bit errors due to the frame format introduced within the payload of the ATM cells. In addition the AAL2 standard introduces a delineation mechanism, which is highly dependant on the ATM and the AAL2 header fields being correct and error-free, as demonstrated by performance results presented in Chapter 4, where the performance of the AAL2 standard was evaluated over error-prone channels. Consequently a new scheme has been devised and numerical results have been presented to demonstrate the performance improvements over the standard AAL2 delineation mechanism.

The numerical results presented in this section demonstrate that the proposed delineation mechanism improves the performance of the AAL2 standard in the presence of bit errors. This gain in performance is achieved by "equalizing" the performance of all the AAL2 packet, regardless of their relative position within the payload of the CPS-PDU. Numerical results presented in Chapter 4 have shown that under metric *mCLR* (probability of a lost AAL2 packet) the first AAL2 packet immediately after the STF field has a better performance than the last CPS packet within the CPS-PDU payload. Under the proposed delineation mechanism this is no longer the case.

In addition, the implementation of the proposed delineation mechanism reduces the overhead required by delineation header fields when the number of AAL2 packets within the CPS-PDU payload is greater than 3.

Chapter 7 Conclusions and Future Work

7.1 Conclusions

In this thesis we present a research study related to the deployment of the ATM Adaptation Layer 2 in wireless ATM networks. The ATM Adaptation Layer 2 was standardized by the ITU-T in recommendation I.363.2 and it was designed to support low data rate and delay sensitive traffic in ATM network. This study is motivated by the interest in evaluating the performance of the AAL2 standard in error-prone links. For example, it is well known that the ATM standard was originally designed to be used over highly reliable links, such as fiber optic links, so it is clear that the bit error process will have an impact on the performance of ATM. On the other hand, the AAL2 standard introduces a new frame structure inside the payload of the ATM cells. This frame structure introduces additional header fields which are also vulnerable to bit errors.

In Chapter 2 we present a description of the AAL2 standard. From this study we can identify two issues of concern for the deployment of the AAL2 standard in WATM networks. First, the AAL2 standard defines several header fields in the CPS-PDU structure. These header fields do not provide any bit error correction capability (as opposed to the HEC field of the ATM header) and bit error may result in corrupted header fields and therefore AAL2 packets will be lost or discarded at the AAL2 layer. Second, the header fields in the CPS-PDU are also used for the delineation of the AAL2 packets. Then a corrupted AAL2 header field may result in more than one AAL2 packet being lost, that is, it is possible that a group of AAL2 packets may be discarded as a result of lost delineation in the CPS-PDU. Having identified these issues, we proceeded to identify a suitable work frame for the characterization of the bit error process at the physical layer.

In Chapter 3 we have identified that the Finite State Markov Chain models provide a suitable analytical work frame for the characterization of the bit error process at the physical layer. Based on the FSMC models it was possible to proceed with the performance analysis of the AAL2 standard in Chapter 4. The Finite State Markov Chain model was used in the derivation of analytical expressions for performance metrics of interest at the AAL2 layer. Such metrics included the probability of packet losses at the AAL2 layer, as well as the probability of bit errors in the payload of the AAL2 packets. The numerical results presented in Chapter 4 have indicated that the performance degradation observed by the users of the AAL2 layer (higher layer applications) is mostly due to the losses of the AAL2 packets. Another observation was that the probability of a lost AAL2 packet increases for each packet in the CPS-PDU. That is, the probability of losing the first AAL2 packet in the CPS-PDU is always lower than the probability of losing any subsequent AAL2 packet. This result is clearly related to the delineation mechanism introduced by the AAL2 standard.

As a result of the impact of bit error in the header fields of the ATM/AAL2 frame structure, in Chapter 5 we propose the introduction of well known techniques to improve system performance, such as, Forward Error Correction codes and diversity techniques. The first approach was the protection of the individual header fields by using BCH codes. The numerical results indicated that the performance gains were not significant, especially when at least one of the ATM or the AAL2 header fields remained unprotected by the BCH codes (see sections 5.2.1 and 5.2.2). On the other hand, the probability of losing an AAL2 packet improves once the ATM and the AAL2 header fields are protected with BCH codes (see section 5.2.3); however this was only true when the physical channel is characterized by a bit error process with a mean burst length in the order of 1 or 2 bits. The second approach was the use of Reed-Solomon codes. This approach required the protection of the payload of a group of ATM cells. The numerical results indicated good performance improvement, as compared to the results obtained with the BCH codes. This observation is especially true for code rates equal or lower than 0.8. However it should be noted that for a RS coder with code rate 0.8 the overhead is approximately 20%.

Later in Chapter 5 we continue the analysis of the AAL2 standard in the presence of equal gain combining (EGC) diversity. This study was motivated by the observation that performance improvements with block codes were only good up to the point were the error correcting capability of the code was not exceeded. That is, another approach had to be devised for error-prone links which are characterized by large mean burst lengths. The numerical results clearly indicate good performance improvements at the AAL2 layer in the presence of EGC. The performance improvements are in the range of two orders of magnitude when introducing a two-branch diversity architecture. Therefore the use of EGC diversity is considered to be the best way to improve system performance at the AAL2 layer in wireless ATM networks. However this approach does not improve the probability of AAL2 packets losses related to the delineation of AAL2 packets. That is, the probability of an AAL2 packets getting lost increases with each AAL2 packet inside the CPS-PDU.

In Chapter 6 we proposed a robust frame format for the AAL2 standard. The proposed frame structure improves the performance at the AAL2 layer by introducing a new mechanism for the delineation of AAL2 packets. This mechanism reduces the probability of losing delineation in the CPS-PDU due to corrupted AAL2 packet headers. In addition, the proposed mechanism can reduce the overhead in the CPS-PDU payload by reducing the size of the AAL2 packet headers, which will make it possible to increase the bandwidth utilization of the wireless links.

7.2 Future Work

The analysis presented in this work is based on the performance optimization of the AAL2 standard over an error-prone link. As a result, diverse mechanisms have been proposed to improve the system performance at the AAL2 layer. Such mechanisms have included the introduction of well know techniques, such as, forward error correction codes and the use of diversity mechanism. In addition a bit-error resilient frame structure has been proposed for the AAL2 standard. This mechanism improves the performance of the AAL2 standard by introducing a robust delineation mechanism which is less vulnerable to bit error.

Future work may consider the benefits of combining the mechanisms presented in this work. For example the proposed resilient mechanism for AAL2 (derived in Chapter 6) can be analysed in conjunction with forward error correction codes or in conjunction with a diversity mechanism. However, special care should be taken as such approaches may not reduce the probability of losses at the AAL2 layer. For example, it can be foreseen that the resilient mechanism proposed in Chapter 6 will not benefit from the introduction of a protection scheme like the one presented in Section 5.2.4, where the Reed-Solomon codes are used to protect the payload of ATM.

Finally, it should be pointed out that the techniques presented in this work can be introduced in the analysis of other protocols in the presence of error-prone links.

Bibliography

[1] N. C. Lobley, "GSM to UMTS – architecture evolution to support multimedia", BT Technology Journal, Vol. 19, No. 1, Jan. 2001, pp. 38-47

[2] B. Subbiah, "Transport architecture evolution in UMTS/IMT-2000 cellular networks", International Journal of Communication Systems, Vol. 13, No. 5, Aug. 2000, pp. 371-385

[3] W. Burakowski, A. Beben, P. Pyda, "Estimation of Multiplexing Gain in ATM tactical Links", IEEE Military Communications Conference, Vol. 1, Oct. 2001, pp. 423-427

[4] C. E. Fossa, N. J. Davis, "3G Wireless Standards Offer Solution to Mobile Services in the Warfighter Information Network", IEEE Military Communications Conference, Vol. 1, Oct. 2001, pp. 403-407

[5] L. Freléchoux, M. Osborne, "Dynamic IP over Mobile ATM", IEEE Military Communications Conference, Vol. 1, Oct. 2001, pp. 741-745

[6] P. S. Giovanni, M. Airst, "Asynchronous Transfer Mode over HF Radio (ATM/HF) A Network Architecture Proposal", IEEE Military Communications Conference, Oct. 1999, pp. 998-1002

[7] R. A. Colton, J. Airst, D. Aschkenasy, D. L. Goldsmith, "ATM for Naval Applications", IEEE Military Communications Conference, Oct. 1999, pp. 384-388

[8] P. Webb, D. Lindsay, P. Thorlby, P. Loretto, S. Eagan, "Design and Implementation of a Generic Testbed for Adapting ATM for the Tactical Radio Environment", IEEE Military Communications Conference, Oct. 1999, pp. 131-134

[9] C. J. van Waveren, H. A. M. Luiijf, W. Burakowski, Z. Kopertowski, "ATM Tactical Network – a challenge for the military networks", Military Conference on Telecommunications and Informatics, Oct. 1997, pp. 349-357

[10] W. C. Quan, E. R. Sive, "POST-2000 Tactical Communications Systems for NATO", IEEE Communications Magazine, Vol. 33, No. 10, Oct. 1995, pp. 113-118

[11] P. F. Sass, L. Gorr, "Communications for the Digitized Battlefield of the 21st Century", IEEE Communications Magazine, Vol. 33, No. 10, Oct. 1995, pp. 86-95

[12] ITU-T I.363.2, "B-ISDN ATM Adaptation Layer Specifications", Sept. 1997

[13] J. H. Chung, Y. H. Kwon, K. H. Cho, D. K. Sung, O. H. Jang, "Performance Evaluation of an AAL2 Link Transmission Scheme for Voice and Data Packets in BS-BSC Links", Proceedings of the 52nd Vehicular technology Conference, Sep. 2000, pp. 1610-1614

[14] O. Isnard, J.-M. Calmel, A.-L. Beylot, G. Pujolle, "Handling Traffic Classes at AAL2/ATM Layer over the Logical Interfaces of the UMTS Terrestrial Radio Access Network", IEEE International Symposium on Personal, Indoor and Mobile Radio Communications, Sep. 2000, pp. 1464-1468

[15] H. Kawakami, F. Ishino, H. Yumiba, "QoS Management of AAL2 in IMTS-2000 Networks", IEICE Transactions on Fundamentals of Electronics, Communications and Computer Sciences, Vol. E84-A, No. 7, July 2001, pp. 1636-1643

[16] H. Saito, "Effectiveness of UBR VC Approach in AAL2 Networks and Its Application to IMT-2000", IEICE Transaction on Communications, Vol. E83-B, No. 11, Nov. 2000, pp. 2486-2493

[17] I. Szabó, S. Székely, I. Moldován, "Performance Optimisation of AAL2 Signalling for Supporting Soft Handoffs in UMTS Terrestrial Radio Access Networks", IEEE Symposium on Computers and Communications, July 2000, pp. 46-51

[18] ITU-T I.366.2, "AAL Type 2 Service Specific Convergence Sublayer for Trunking", Feb. 1999

[19] ITU-T G.711, "Pulse Code Modulation (PCM) of Voice Frequencies", Nov. 1988

[20] ITU-T G.726, "40, 32, 24, 16 kbit/s Adaptive Differential Pulse Code Modulation (ADPCM)", Dec. 1990

[21] ITU-T G.729, "Coding of Speech at 8 kbit/s using Conjugate-Structure Algebraic-Code-Excited Linear-Prediction (CS-ACELP)", Mar. 1996

[22] ITU-T G.729 Annex D, "6.4 kbit/s CS-ACELP speech coding algorithm", Sep. 1998

[23] ITU-T G.729 Annex E, "11.8 kbit/s CS-ACELP speech coding algorithm", Sep. 1998

[24] W. C. Jakes, "Microwave Mobile Communications", Wiley, 1974, New York

[25] A. M. Chen, R. R. Rao, "On Tractable Wireless Channel Models", Proc. 9th IEEE International Symposium on Personal, Indoor and Mobile Radio Communications, Vol. 2, Sept. 1998, pp. 825-830

[26] M. J. Chu, D. L. Goeckel, W. E. Stark, "On the Design of Markov Models for Fading Channels", Proc. 50th Vehicular Technology Conference, Sept. 1999, pp. 2372-2376

[27] E. O. Elliott, "Estimates of error rates for codes on burst-error channels", Bell Systems Technical Journal, Vol. 42, Sept. 1963, pp. 1977-1997

[28] E. N. Gilbert, "Capacity of a burst-noise channel", Bell Systems Technical Journal, Vol. 39, Sept. 1960, pp. 1253-1266

[29] Y. L. Guan, L. F. Turner, "Generalised FSMC model for radio channels with correlated fading", IEE Proceedings Communications, Vol. 146, No. 2, Apr. 1999, pp. 133-137

[30] J. Lu, K. B. Letaief, M. L. Liou, "Robust Video Transmission over Correlated Fading Channels", IEEE Transactions on Circuits and Systems for Video Technology, Vol. 9, No. 5, Aug. 1999, pp 737-751

[31] S. D. Morgera, F. Simard, "Parameter Estimation for a Burst-Noise Channel", Proc. International Conference on Acoustics, Speech and Signal Processing, Vol. 3, May 1991, pp. 1701-1704

[32] C. Pimentel, I. F. Blake, "Enumeration of Markov Chains and Burst Error Statistics for Finite State Channel Models", IEEE Transactions on Vehicular Technology, Vol. 48, No. 2, March 1999, pp. 415-428

[33] F. Swarts, H. C. Ferreira, "Markov Characterization with Soft Decision Outputs", IEEE Transactions on Communications, Vol. 41, No. 5, May 1993, pp. 678-682

[34] W. Turin, R. van Nobelen, "Hidden Markov Modeling of Fading Channels", Proc. 48th IEEE Vehicular Technology Conference, May 1998, pp. 1234-1238

[35] W. Turin, R. van Nobelen, "Hidden Markov Modeling of Flat Fading Channels", IEEE Journal on Selected Areas in Communications, Vol. 16, No. 9, Dec. 1998, pp. 1809-1817

[36] W. Turin, M. Monhan Sondhi, "Modeling Error Sources in Digital Channels", IEEE Journal on Selected Areas in Communications, Vol. 11, No. 3, Apr. 1993, pp. 340-347

[37] H. S. Wang, P. C. Chang, "On Verifying the First-Order Markovian Assumption for a Rayleigh Fading Channel Model", IEEE Transactions on Vehicular Technology, Vol. 45, No. 2, May 1996, pp. 353-357

[38] H. S. Wang, N. Moayeri, "Finite-State Markov Channel – A Useful Model for Radio Communication Channels", IEEE Transactions on Vehicular Technology, Vol. 44, No. 1, Feb. 1995, pp. 163-171

[39] L. Wilhelmsson, L. B. Milstein, "On the Effect of Imperfect Interleaving for the Gilbert-Elliott Channel", IEEE Transactions on Communications, Vol. 47, No. 5, May. 1999, pp. 681-688

[40] M. Zorzi, R. R. Rao, "On the Impact of Burst Errors on Wireless ATM", IEEE Personal Communications, Vol. 6, No. 4, Aug. 1999, pp. 65-75

[41] M. Zorzi, R. R. Rao, "On the Statistics of Block Errors in Bursty Channels", IEEE Transactions on Communications, Vol. 45, No. 6, June 1997, pp. 660-667

[42] T. S. Rappaport, "Wireless Communications Principles & Practice", Ed. Prentice-Hall, 1996.

[43] M. K. Simon, M. Alouini, "Digital Communication over Fading Channels: A Unified Approach to Performance Analysis", Wiley-Interscience, 2000.

[44] M. Nakagami, "The m-Distribution – A General Formula of Intensity Distribution of Rapid Fading", Statistical Methods in Radio Wave Propagation, Jun. 1958, pp. 3-36.

[45] S. A. Abbas, A. U. Sheikh, "A Geometric Theory of Nakagami Fading Multipath Mobile Radio Channel with Physical Interpretations", IEEE 46th Vehicular Technology Conference, Apr. 1996, pp. 637-641.

[46] D. P. Petr, R. R. Vatte, P. Sampath, Y. Lu, "Efficiency of AAL2 for Voice Transport: Simulation Comparison with AAL1 and AAL5", IEEE International Conference on Communications, June 1999, pp. 896-901.

[47] S. Jeong, D. K. Hsing, T. Wu, J. A. Copeland, "Trunking Performance Analysis of AAL2 for VBR Voice Transport", IEEE International Conference on Communications, June 1999, pp. 886-890.

[48] H. Saito, "Performance Evaluation of AAL2 Switching Networks", IEICE Transaction on Communications, Vol. E82-B, No. 9, Sep. 1999, pp. 1411-1423.

[49] J. H. Chung, Y. H. Kwon, K. H. Cho, D. K. Sung, O. H. Jang, "Performance Evaluation of an AAL2 Link Transmission Scheme for Voice and Data Packets in BS-BSC Links", Transactions of the IEEE Vehicular Technology Conference, Sep. 2000, pp. 1610-1614.

[50] K. Sriram, T. G. Lyons, Y. T. Wang, "Anomalies Due to Delay and Loss in AAL2 Packet Voice Systems: Performance Models and Methods of Mitigation", IEEE Journal on Selected Areas in Communications, Vol. 17, No. 1, Jan. 1999, pp. 4-17.

[51] K. Sriram, Y. T. Wang, "Voice over ATM Using AAL2 and Bit Dropping: Performance and Call Admission Control", IEEE Journal on Selected Areas in Communications, Vol. 17, No. 1, Jan. 1999, pp. 18-28.

[52] C. Liu, S. Munir, R. Jain, "Packing Density of Voice Trunking using AAL2", IEEE Global Telecommunication Conference, Dec. 1999, pp. 611-615.

[53] B. Subbiah, S. Dixit, "ATM Adaptation Layer 2 (AAL2) for Low Bit Rate Speech and Data: Issues and Challenges", Proceedings of the IEEE ATM Workshop, 1998, pp. 225-233.

[54] B. Subbiah, S. Dixit, "Low-Bit-Rate Voice and Telephony over ATM in Cellular/Mobile Networks", IEEE Personal Communications, Vol. 6, No. 6, Dec. 1999, pp. 37-43.

[55] The Network Simulator – ns-2. http://www.isi.edu/nsnam/ns/

[56] S. Aikawa, Y. Motoyama, M. Umehira "Forward Error Correction Schemes for Wireless ATM Systems", IEEE International Conference on Communications, June 1996, pp. 454-458

[57] I. F. Akyildiz, I. Joe, H. Driver, Y. L. Ho, "A new Adaptive FEC Scheme for Wireless ATM Networks", IEEE Military Communications Conference, Oct. 1998, pp. 277-281

[58] M. M. Al-Khatib, M. Bayoumi, "New Automatic Error Control System with ATM Cell Header Reduction for Wireless ATM Networks", Proceedings of the 1999 IEEE ATM Workshop, May. 1999, pp 233-238

[59] M. Barton, "Unequal Error Protection for Wireless ATM Applications", IEEE Global Telecommunications Conference, Nov. 1996, pp. 1911-1915

[60] J. B. Cain, D. N. McGregor, "A Recommended Error Control Architecture for ATM Networks with Wireless Links", IEEE Journal on Selected Areas in Communications, Vol. 15, No. 1, Jan. 1997, pp. 16-28

[61] P. R. Denz, A. A. Nilsson, "Performance of Error Control Coding Techniques for Wireless ATM", Proceedings of the IEEE International Conference on Communications, Vol. 2, Jun. 1998, pp. 1099-1103

[62] J. F. Durkin, "A Reliable Wireless ATM System", Proceedings of the 1998 IEEE Aerospace Applications Conference, Vol. 4, Mar. 1998, pp. 443-448

[63] D. S. Eom, M. Sugano, M. Murata, H. Miyahara, "A Combination Scheme of ARQ and FEC for Multimedia Wireless ATM Networks", IEICE Transactions on Communications, Vol. E81-B, No. 5, May 1998, pp. 1016-1024

[64] A. H. Levesque, B. E. Basch, R. R. Voruganti, A. M. Michelson, "Reliable ATM Transmission in Tactical Networks", Proceedings of the Second Annual FEDLAB Symposium, Feb. 1998, pp. 246-250

[65] D. Moore, M. Rice, "Variable Rate Error Control for Wireless ATM Networks", Proceedings of the IEEE International Conference on Communications, Vol. 2, Jun. 1995, pp. 988-991

[66] S. V. Pizzi, et. al. , "Error Control for Tactical ATM", IEEE Military Communications Conference, Vol. 2, 1998, pp. 397-408

[67] C. Schuler, "Optimization and Adaptation of Error Control Algorithms for Wireless ATM", International Journal of Wireless Information Networks, Vol. 5, No. 2, Apr. 1998, pp. 173-185

[68] C. Schuler, "Error Correction Strategies for Wireless ATM", Proceedings of the 4th IEEE Workshop on High-Performance Communication Systems, 1997, pp. 204-213

[69] Z. Sun, S. Kimura, Y. Ebihara, "Adaptive Two-level Unequal Error Protection Convolutional Code Scheme for Wireless ATM Networks", Proceedings of the 19th IEEE Annual Joint Conference of the IEEE Computer and Communications Societies (INFOCOM 2000), Vol. 3, pp. 1693-1697

[70] J. R. Yee, E. J. Weldon, "Evaluation of the Performance of Error-Correcting Codes on a Gilbert Channel", IEEE Transactions on Communications, Vol. 43, No. 8, Aug. 1995, pp. 2316-2323

[71] W. A. Geisel, "Tutorial on Reed-Solomon Error Correction Coding", NASA Technical Memorandum 102162, Aug. 1990.

[72] S. Lin, D. J. Costello, "Error Control Coding: Fundamentals and Applications", Prentice-Hall Inc., 1983.

[73] M. Abdel-Hafez, M. Safak, "Simplified analysis of equal gain combining in Nakagami fading channels", Electronics Letters, Vol. 33, No. 23, Nov. 1997, pp. 1926-1927

[74] M.-S. Alouini, M. K. Simon, "Error Rate Analysis of *M*-PSK with Equal Gain Combining over Nakagami Fading Channels", Proceedings of the 49th Vehicular technology Conference, May 1999, pp. 2378-2382

[75] M.-S. Alouini, M. K. Simon, "Performance of Coherent Receivers with Hybrid SC/MRC over Nakagami-*m* Fading Channels", IEEE Transactions on Vehicular Technology, Vol. 48, No. 4, July 1999, pp. 1155-1164

[76] Y.-C. Ko, M.-S. Alouini, M. K. Simon, "Averaged SNR of Dual Selection Combining over Correlated Nakagami-*m* Fading Channels", IEEE Communications Letters, Vol. 4, No. 1, Jan. 2000, pp. 12-14

[77] P. Lombardo, G. Fedele, M. M. Rao, "MRC Performance for Binary Signals in Nakagami Fading with General Branch Correlation", IEEE Transactions on Communications, Vol. 47, No. 1, Jan. 1999, pp. 44-52

[78] J. Reig, N. Cardona, L. Rubio, "Performance of Radio Cellular Systems using Maximal Ratio Combining in a Correlated Nakagami Fading with Multiple Interferers", Proceedings of the 49th Vehicular Technology Conference, May 1999, pp. 2358-2362

[79] C. R. C. M. da Silva, M. D. Yacoub, "Bit error analysis of equal gain combining reception for Nakagami fading channels: An exact formulation", Electronics Letters, Vol. 36, No. 13, June 2000, pp. 1147-1149

[80] M. Z. Win, G. Chrisikos, J. H. Winters, "Error Probability for M-ary Modulation in Correlated Nakagami Channels using Maximal Ratio Combining", IEEE military Communications Conference, Oct. 1999, pp. 70-75

[81] M. D. Yacoub, C. R. C. M. da Silva, J. E. Vargas B., "Second-order statistics for equal gain and maximal ratio diversity-combining reception", Electronics Letters, Vol. 36, No. 4, Feb. 2000, pp. 382-384

[82] Y. Karasawa, H. Iwai, "Formulation of Spatial Correlation Statistics in Nakagami-Rice Fading Environments", IEEE Transactions on Antennas and Propagation, Vol. 48, No. 1, Jan. 2000, pp. 12-18

[83] G. Held, T. R. Marshall, "Data compression: techniques and applications: hardware and software considerations", 3rd. ed., John Wiley, 1991.

Appendix A AAL2 Encoding Profiles (I.366.2)

Recommendation I.366.2/ Annex P defines a set of ITU-T predefined profiles to be used with audio information streams. Encoding profiles for audio algorithms G.711, G.726 and G.729 are presented in Table 17 - Table 24.

Table 17: Profile using PCM-64.

UUI codepoint range	Packet length (octets)	Description of algorithm	M	Packet time (ms)
0 - 15	40	PCM, G.711-64, generic	1	5

Table 18: Profile using PCM and silence.

UUI codepoint range	Packet length (octets)	Description of algorithm	M	Packet time (ms)
0 - 15	40	PCM, G.711-64, generic	1	5
0 - 15	1	Generic SID	1	5

Table 19: Profile using ADPCM and silence.

UUI codepoint range	Packet length (octets)	Description of algorithm	M	Packet time (ms)
0 - 15	40	PCM, G.711-64, generic	1	5
0 - 15	25	ADPCM, G.726-40	1	5
0 - 15	20	ADPCM, G.726-32	1	5
0 - 15	15	ADPCM, G.726-24	1	5
0 - 15	10	ADPCM, G.726-16	1	5
0 - 15	1	Generic SID	1	5

Table 20: Profile using G.729 with higher efficiency and G.726 for voiceband data.

UUI codepoint range	Packet length (octets)	Description of algorithm	M	Packet time (ms)
0 - 15	40	PCM, G.711-64, generic	1	5
0 - 15	25	ADPCM, G.726-40	1	5
0 - 15	20	CS-ACELP, G.729-8	2	20
0 - 15	16	CS-ACELP, G.729-6.4	2	20
0 - 15	10	CS-ACELP, G.729-8	1	10
0 - 15	8	CS-ACELP, G.729-6.4	1	10
0 - 15	2	G.729 SID	1	10

Table 21: Profile using G.729 with lower delay.

UUI codepoint range	Packet length (octets)	Description of algorithm	M	Packet time (ms)
0 - 15	40	PCM, G.711-64, generic	1	5
0 - 15	10	CS-ACELP, G.729-8	1	10
0 - 15	2	G.729 SID	1	10

Table 22: Profile using G.729 with lower delay and G.726-32 for voiceband data at lower rates.

UUI codepoint range	Packet length (octets)	Description of algorithm	M	Packet time (ms)
0 - 15	40	PCM, G.711-64, generic	1	5
0 - 15	20	ADPCM, G.726-32	1	5
0 - 15	10	CS-ACELP, G.729-8	1	10
0 - 15	2	G.729 SID	1	10

Table 23: Profile using G.729 with lower delay and G.726-40 for voiceband data at higher rates.

UUI codepoint range	Packet length (octets)	Description of algorithm	M	Packet time (ms)
0 - 15	40	PCM, G.711-64, generic	1	5
0 - 15	25	ADPCM, G.726-40	1	5
0 - 15	10	CS-ACELP, G.729-8	1	10
0 - 15	8	CS-ACELP, G.729-6.4	1	10
0 - 15	2	G.729 SID	1	10

Table 24: Profile using G.729 with full variable bit rates.

UUI codepoint range	Packet length (octets)	Description of algorithm	M	Packet time (ms)
0 - 15	40	PCM, G.711-64, generic	1	5
0 - 15	30	CS-ACELP, G.729-12	2	20
0 - 15	20	CS-ACELP, G.729-8	2	20
0 - 15	16	CS-ACELP, G.729-6.4	2	20
0 - 15	15	CS-ACELP, G.729-12	1	10
0 - 15	10	CS-ACELP, G.729-8	1	10
0 - 15	8	CS-ACELP, G.729-6.4	1	10
0 - 15	2	G.729 SID	1	10

Appendix B Derivation of FSMC model parameters

B.1 The Gilbert-Elliot Model

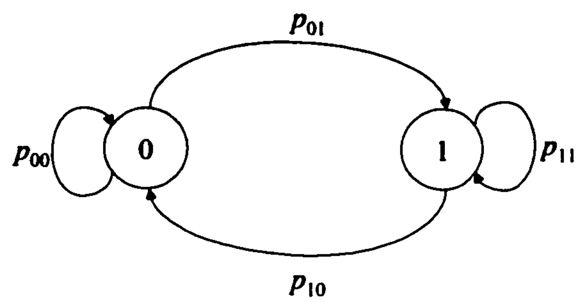

Figure B.1: Gilbert-Elliott channel model.

The Gilbert-Elliot model is characterized by a two state Markov chain, as illustrated in Figure B.1. The derivation of the Gilbert-Elliott model parameters, in the context of this Thesis, is based on the following factors: the channel bit error rate ε, the state error probabilities $P_e(0)$ and $P_e(1)$, and the mean burst length τ. Recall that the mean burst length is considered to be the average time spent in state 1, which is defined to be the inverse of the probability of a transition from state 1 to state 0, which is defined as p_{10}. Therefore, the transition probability p_{10} can be evaluated in terms of the mean burst length τ,

$$p_{10} = \frac{1}{\tau}, \tag{B.1}$$

and the probability of a transition from state 1 to state 1, defined as p_{11}, is just the complement of Expression (B.1). That is, p_{11} is equal to

$$p_{11} = 1 - p_{10}. \tag{B.2}$$

The next step is to derive the transition probability from state 0 to state 1, which is defined as p_{01}. This expression can be evaluated from Expression (10), which is used to evaluate the channel bit error rate in terms of the steady state probabilities π_0 and π_1, and the state error probabilities $P_e(0)$ and $P_e(1)$. Then p_{01} can be evaluated as

$$p_{01} = \frac{(P_e(0)-\varepsilon)p_{10}}{\varepsilon - P_e(1)}, \tag{B.3}$$

and the transition probability from state 0 to state 0, defined as p_{00}, is just the complement of Expression (B.3). That is, p_{11} is equal to

$$p_{00} = 1 - p_{01}. \tag{B.4}$$

Then the transition probability matrix **P** is completely defined by evaluating Expressions (B.1) - (B.4). The next step is to evaluate the steady state probabilities π_0 and π_1. These probabilities can be easily evaluated in terms of the transition probabilities p_{01} and p_{10}, as defined in Expression (9).

B.2 The FSMC Model for Diversity

The FSMC model implemented for the diversity analysis relies on the statistical characterization of the time varying fading process, as described in Section 3.3. The first step on the derivation of the FSMC model parameters consists in evaluating the steady state probability vector $\boldsymbol{\pi}$. The analysis used in diversity assumes a FSMC composed of N = 6 states. Then, the steady state probabilities π_k, k = 1, 2, 3, 4, 5 and 6 can be evaluated using the recursive algorithm presented in [30],

$$\pi_k = \begin{cases} \dfrac{1}{2^N - 1} & k = 1 \\ 2 \cdot \pi_{k-1} & k = 2, ..., N \end{cases}. \tag{B.5}$$

Recall that the derivation of the FSMC model, as described in Section 3.3, departs from the concept of appropriately partitioning the dynamic range of the fading amplitude into a finite number of non-overlapping intervals. In other words, each state s_k can be derived in terms of the non-overlapping intervals and the channel is said to be in state s_k if the fading amplitude of the fading signal falls within the interval defined by $[\alpha_{k-1}, \alpha_k)$. The derivation of these non-overlapping intervals is facilitated by using an alternate representation for the derivation of the steady state probabilities π_k. Namely, the steady state probabilities π_k can be derived in terms of the probability density function $p_A(\alpha)$ that characterizes the fading process,

$$\pi_k = \int_{\alpha_{k-1}}^{\alpha_k} p_A(\alpha) d\alpha, \tag{B.6}$$

and for a Nakagami-m distributed fading process Expression (B.6) becomes

$$\pi_k = \frac{\Gamma(m, 0, m \times \alpha_k^{\,2}/\Omega) - \Gamma(m, 0, m \times \alpha_{k-1}^{\,2}/\Omega)}{\Gamma(m)}, \tag{B.7}$$

where m is defined as the Nakagami-m fading parameter, Ω is defined as the mean square value of the fading amplitude α and $\Gamma(a, z_0, z_1)$ is defined as the generalized incomplete gamma function.

The numerical results, presented in **5.3.1**, assume the use of Equal Gain Combining diversity and the fading process is characterized by a Rayleigh distribution. Then the Nakagami-m fading parameter on each diversity branch is defined to be equal to $m_0 = 1$ (because of the Rayleigh fading assumption). Also, without loss of generality, we assume a normalized mean square value $\Omega_0 = 1$ for the fading amplitude on each diversity branch. So the Nakagami-m fading parameter m and the mean square value Ω, assuming EGC diversity, are given by

$$m \cong L m_0, \tag{B.8}$$

$$\Omega = L\Omega_0 + L(L-1)\Omega_0 \frac{\Gamma^2(m_0 + 1/2)}{m_0 \Gamma^2(m_0)}, \tag{B.9}$$

where L is equal to the number of diversity branches and $\Gamma(.)$ is defined as the Gamma function.

At this point the values of the fading amplitude levels α_k are evaluated numerically using Expression (B.7) beginning with $\alpha_0 = 0$, as the Nakagami-m fading parameter m, the mean square value Ω and the steady state probabilities π_k are known from Expressions (B.5), (B.8) and (B.9) respectively.

Now we are in a position to evaluate the transition probability matrix $\mathbf{P}$. The transition probabilities p_{ij}, $i, j \in \{1, 2, 3, 4, 5, 6\}$ can be evaluated in terms of the non-overlapping intervals $[\alpha_{k-1}, \alpha_k)$ and the probabilities of a transition from one interval to another, as defined by,

$$p_{ij} = \frac{Pr[\alpha_{i-1} \le \alpha_1 < \alpha_i, \alpha_{j-1} \le \alpha_2 < \alpha_j]}{Pr[\alpha_{i-1} \le \alpha_1 < \alpha_i]} = \frac{\int_{\alpha_{j-1}}^{\alpha_j} \int_{\alpha_{i-1}}^{\alpha_i} p_{A_1,A_2}(\alpha_1, \alpha_2) d\alpha_1 d\alpha_2}{\int_{\alpha_{i-1}}^{\alpha_i} p_{A_1}(\alpha_1) d\alpha_1}. \tag{B.10}$$

It should be noted that the denominator of Expression (B.10) is equal to the steady state probabilities π_i and these probabilities have already been evaluated in Expression (B.5). The numerator of Expression ((B.10)) is evaluated numerically using the joint probability density function of a Nakagami-m distribution given by

$$p_{A_1,A_2}(\alpha_1, \alpha_2) = \frac{4(\alpha_1\alpha_2)^m \exp\left[-\frac{m}{\Omega}\frac{\alpha_1^2 + \alpha_2^2}{1-\rho}\right]}{\Gamma(m)(1-\rho)(\sqrt{\rho})^{m-1}} \left(\frac{m}{\Omega}\right)^{m+1} I_{m-1}\left(\frac{2m\alpha_1\alpha_2\sqrt{\rho}}{\Omega(1-\rho)}\right), \tag{B.11}$$

It should be noted that all parameters in Expression (B.11) are known except for the correlation coefficient ρ. The correlation coefficient is evaluated from Expression (60). For the particular case of a Rayleigh distributed fading process, the correlation coefficient ρ is given by

$$\rho = \frac{2\{J_0(2\pi f_d \tau_b)\} + s^2\{J_0(2\pi f_d \tau_b)^2\}}{2+s^2}, \tag{B.12}$$

where $J_0(\cdot)$ is the zero-order Bessel function of the first kind, τ_b is the channel symbol duration, f_d is the Doppler frequency and s^2 is the average scattered wave power normalized by the direct-wave power, which is related to the *Ricean* parameter K by $s^2 = K^{-1}$. It should be noted that the numerical results presented in Section 5.3 are obtained as a function of the argument $2\pi f_d \tau_b$, which characterizes the fading channel. Therefore, the only unknown quantity in Expression (B.12) is the value of s^2. The analysis assumes a Rayleigh distributed fading channel, therefore we rely on the definition of s^2 and assume a direct-wave signal power which is 10dB lower than the average scattered wave power, that is K_{dB} = -10 dB. Then s^2 can be evaluated as

$$s^2 = \left(10^{K\mathrm{db}/10}\right)^{-1}. \tag{B.13}$$

At this point we can evaluate all the transition probabilities p_{ij} using Expression (B.10). The last step in defining the channel FSMC model is to derive the state error probabilities $P_e(k)$, k =1, 2, 3, 4, 5, 6. The derivation of the state error probabilities is related to the modulation/demodulation scheme that is in use. The analysis presented in Section 5.3 assumes a non-coherent QPSK demodulation scheme. Therefore the state error probabilities are evaluated as

$$P_e(k) = \frac{1}{\pi_k}\int_{\alpha_{k-1}}^{\alpha_k} f_A(\alpha)\cdot e(\alpha)d\alpha, \tag{B.14}$$

where expression $e(\alpha)$ for non-coherent QPSK is given by

$$e(\alpha) = \frac{1}{2}erfc\left(\sqrt{\frac{\alpha^2}{N_{pw}}}\right), \tag{B.15}$$

where *erfc*(.) represents the complementary error function and N_{pw} represent the noise power after Equal Gain Combining. The noise power is calculated as follows, under Equal Gain Combining the average noise power N_{pw}(dB) is just the sum of the mean noise power N'(dB) on each diversity branch. That is,

$$N_{pw}(\mathrm{dB}) = \sum_{i=1}^{L} N'(\mathrm{dB}) \text{ or } N_{pw} = L \cdot N'. \tag{B.16}$$

It should be noted that with all the information derived to this point it is possible to evaluate the channel error rate in terms of the signal-to-noise ration (SNR). The relationship between the SNR and the mean noise power is given by

$$\mathrm{SNR}(\mathrm{dB}) = \frac{S}{N'}(\mathrm{dB}) \text{ or } \frac{S}{N'} = 10^{\mathrm{SNR}(\mathrm{dB})/10}, \tag{B.17}$$

Where S is the signal power and is equal to the mean square value Ω. Therefore, the mean noise power can be calculated as

$$N' = \Omega \cdot 10^{\left(\mathrm{SNR}(\mathrm{dB})/10\right)}. \tag{B.18}$$

Figure B.2, illustrates the channel BER as a function of the SNR. From the previous analysis it is derived that the required SNR to achieve a channel BER of 10-3 is SNR(dB) = 23dB. This is the last value that is required to derive all the parameters of the FSMC model that is used in Section 5.3.

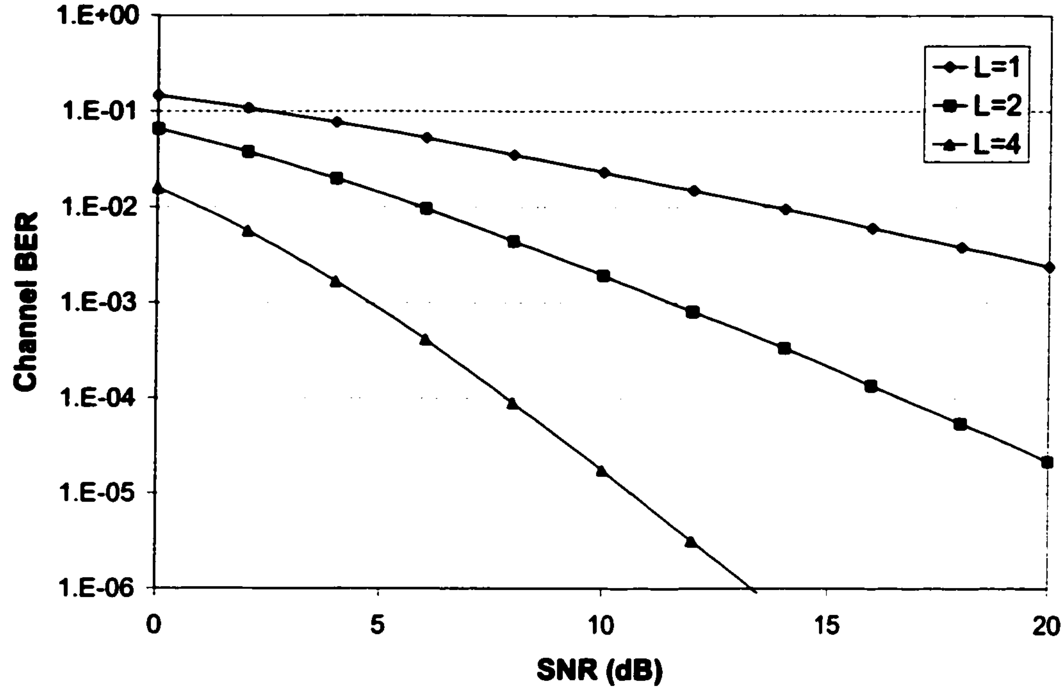

Figure B.2: Channel BER using EGC diversity.